1-1-2017

Water Splitting Using Cobalt-Based Amidopyridine Complexes

Habib Baydoun
Wayne State University,

WATER SPLITTING USING COBALT-BASED AMIDOPYRIDINE COMPLEXES

by

HABIB BAYDOUN

DISSERTATION

Submitted to Graduate School

of Wayne State University,

Detroit, Michigan

in partial fulfillment of the requirements

for the degree of

DOCTOR OF PHILOSOPHY

2017

MAJOR: CHEMISTRY (Inorganic)

Approved By:

_____

Advisor Date

_____

_____

_____

_____

DEDICATION

To my parents, thank you for your love and endless support

ACKNOWLEDGEMENTS

I would like to start by thanking my advisor Prof. Claudio Verani for his support, encouragement and insights. Without you I quiet literally could not have done my research. I would also like to extend my gratitude to my committee members Prof. Stanislav Groysman, Prof. H. Bernhard Schlegel, and Dr. Karen Mulfort. Thank you for taking time to serve on my committee and for always being there when I needed you.

I would also like to extend my gratitude to my collaborators, Prof. Schlegel, Prof. Stephanie Brock, and their students Dr. Shivnath Mazumder, Bishnu Thapa, and Da Li from Wayne State university, as well as Dr. Oleg Poluektov and Dr. Jens Niklas from Argonne National Laboratory. Without their insights and helpful input my research would not have been possible.

I also would like to thank my undergraduate research advisor, Prof. Antoine Ghauch, for introducing me to chemical research. Your enthusiasm inspired me to peruse my graduate studies.

I would also like to thank my group members over the years; Dr. Dajena Tomco, Dr. Dakshika Wanniarachchi Dr. Lanka Wickramasinghe, Dr. DEBASHIS BASU, Dr. Ryan Thomas, Dr. Sunalee Gonawala, and Dr. Kenneth Kpogo, as well as the future doctors Danushka Ekanayake, Pavithra Kankanamalage, Nour El Harakeh, Isuri Weeraratne, Samudra Amunugama, Fredricka Morgan, Renata Crispin, and Krista Kulesa. Thank you for making the past five years some of the most enjoyable. A special shout out is in order to my undergraduate student Jordyn Burdick (future PA), without your help most of the work in chapter 5 would not have been possible.

I also need to thank all my friends at WSU for always being there for me when I needed you. I would particularly like to thank Da, Marissa, Lucas, and Ahmad. You guys are the best. I would especially like to thank Krista for being the man!

I would like to thank the National Science Foundation, and the Department of Energy for providing the funding that made my doctoral work possible. I would also like to thank Wayne State University for personal funding in the form of the Thomas C. Rumble, and Mary G. Wood fellowships.

Lastly and most importantly, I would like to extend my deep appreciation to my parents Zahera Darwiche, and Hassan Beydoun, as well as my sisters Rola, Abir, Youser, and Nour. Your love and support made it possible for me to carry on with my studies.

TABLE OF CONTENTS

LIST OF TABLES

LIST OF FIGURES

CHAPTER 1. INTRODUCTION

Portions of this chapter are reproduced with permission from: *Basu, D.; Mazumder, S.; Shi, X.; Baydoun, H.; Niklas, J.; Poluektov , O.; Schlegel, H. B.; Verani, C.; Angew. Chem. Intl. Ed.* **2015**, *54, 2105. Basu, D.; Mazumder, S.; Niklas, J.; Baydoun, H.; Wanniarachchi, D.; Shi, X.; Staples, R.; Poluektov , O.; Schlegel, H. B.; Verani, C.; Chem. Sci.* **2016**, *7, 3264. Gonawala, S.; Baydoun, H.; Wickramasinghe, L.; Verani, C.; Chem. Commun.* **2016**, *52, 8440*.

1.1. Splitting Water as a Source of Alternative Energy

With the impending depletion of fossil fuels, there is a pressing need to develop new sources of alternative energy.[1] With this goal in mind, hydrogen gas has been proposed as a clean alternative to carbon-based energy. However, current methods of producing hydrogen rely on either the steam reforming and the water shift reactions.[2] In the steam reforming reaction, methane is reacted with water to release hydrogen and carbon monoxide gases (**equation 1.1.**). The water gas shift reaction (**equation 1.2.**) produces hydrogen by reacting carbon monoxide with water to release hydrogen and carbon dioxide. Both reactions have their drawbacks, since the first requires the use of hydrocarbons and the second produces carbon dioxide.

$$CH_4 + H_2O \rightarrow CO + 3H_2 \qquad \textbf{(equation 1.1.)}$$

$$CO + H_2O \rightarrow CO_2 + H_2 \qquad \textbf{(equation 1.2.)}$$

Splitting water into hydrogen and oxygen gases has emerged as a source of alternative energy. The water splitting reaction (**equation 1.3.**) can be divided into two half reactions. The first reaction (**equation 1.4.**) water oxidation, in which two molecules of water are split to generate one molecule of oxygen and four protons as well as four electrons. The second reaction (**equation 1.5.**) is proton reduction; in this reaction, the protons and electrons that were generated in the first reaction combine to generate hydrogen gas.

$2H_2O \rightarrow O_2 + 4H^+ + 4e^-$ (**equation 1.4.**) $E^0 = 1.23\ V_{NHE}$

$4H^+ + 4e^- \rightarrow 2H_2$ (**equation 1.5.**) $E^0 = 0.00\ V_{NHE}$

$2H_2O \rightarrow O_2 + 2H_2$ (**equation 1.3.**)

Both the water oxidation and proton reduction reactions are nontrivial as they require the transfer of multiple protons and electrons. Therefore, a great deal of work has focused on developing metal catalysts that can lower the activation barriers of these reactions. Although initial work focused almost exclusively on the use of precious metals, such as platinum for proton reduction, and ruthenium and iridium for water oxidation, there has been a paradigm shift in the scientific literature towards the use of Earth-abundant metals as water splitting catalysts.[3-7]

1.2. Proton Reduction Catalysis

1.2.1. Mechanism of Proton Reduction

Cobalt, with its ability to stabilize highly reduced oxidation states such as Co^I, has been extensively utilized as a metal ion capable of performing proton reduction. Most of the reported mechanistic pathways associated with proton reduction using cobalt are shown in **Figure 1.1.**[8-13] When [Co^I] reacts with a proton, a [Co^{III}-H^-] is formed. Following this step, the mechanism is thought to proceed *via* heterolytic or homolytic pathways. In the heterolytic pathway, the [Co^{III}-H^-] reacts with yet another proton in solution to regenerate the [Co^{III}] catalyst as well as hydrogen gas. Conversely in the homolytic pathway, after the generation of the [Co^{III}-H^-] species, two [Co^{III}-H^-] species react with each other to release hydrogen gas and regenerate the [Co^{II}] species. Other pathways have been proposed involving the reduction of [Co^{III}-H^-] to [Co^{II}-H^-], followed by the generation of hydrogen in a similar mechanism to that of [Co^{III}-H^-]. Finally, proton coupled electron transfer (PCET) processes from [Co^{II}] to [Co^{III}-H^-] and [Co^I] to [Co^{II}-H^-] are possible.

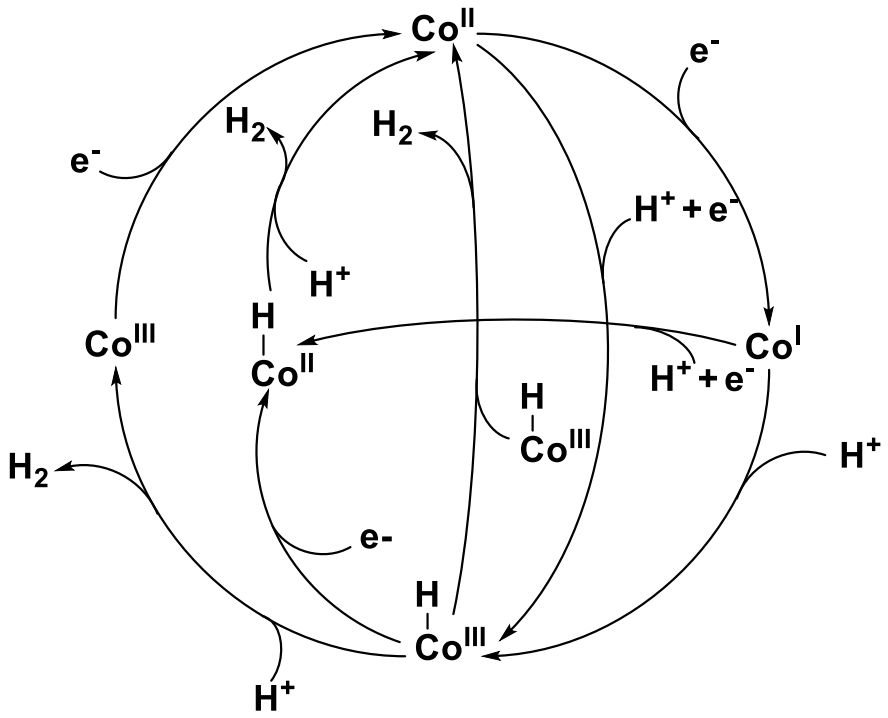

Figure 1.1. The mechanisms of electrocatalytic proton reduction.

With the proton reduction mechanism in mind, one can point to the important interplay between the reactivity and stability of the intermediates. For instance, [Co^{I}] needs to be sufficiently nucleophilic to react with protons. Therefore, the addition of strongly electron withdrawing groups is expected to hinder reactivity. However, [Co^{I}] needs to be reached at a moderate potential because more negative [Co^{I}] potentials are directly correlated to higher overpotentials. As such, the addition of strong electron donating groups possibly has deleterious effects on catalysis. Moreover, [Co^{III}-H^{-}] needs to be reactive enough to allow the catalytic cycle to continue because if it is too stable then the cycle will not proceed. These conclusions underscore the importance of ligand design in the development of efficient molecular water reduction catalysts.

Molecular proton reduction catalysis can be performed by using (i) photosensitizers, (ii) applied electrochemical potentials, and to a much lesser extent (iii) using chemical reductants. One of the most common photosensitizers is tris(bipyridine)ruthenium(II) ($[Ru^{II}(bpy)_3]^{2+}$). The

mechanism by which $[Ru^{II}(bpy)_3]^{2+}$ operates is shown in **Figure 1.2.**[14] Upon irradiation with an appropriate wavelength, $[Ru^{II}(bpy)_3]^{2+}$ gets excited and forms $[Ru^{II*}(bpy)_3]^{2+}$. $[Ru^{II*}(bpy)_3]^{2+}$ then transfers an electron to the catalyst before generating the oxidized form $[Ru^{III}(bpy)_3]^{3+}$. $[Ru^{II}(bpy)_3]^{2+}$ is regenerated from $[Ru^{III}(bpy)_3]^{3+}$ in the presence of a sacrificial electron donor such as ascorbic acid or triethylamine. Alternatively, the electrons needed to generate hydrogen gas could be obtained directly from the surface of an electrode by applying an electrochemical potential that is negative enough to drive catalysis. Catalysis is generally performed using a standard three-electrode setup with a Pt auxiliary electrode, Ag/AgCl reference electrode and Hg-pool working electrode. Finally, the last method of performing proton reduction is by using chemical reductants. However, expense and extreme air sensitivity of these reducing agents prohibits the widespread application of this method.[15] It is therefore limited to gaining mechanistic insights into the catalytic cycle by first chemically reducing the catalyst and then reacting it with a selected proton source to form hydrogen. Spectroscopic techniques are then used to follow the kinetics of the reaction.[16]

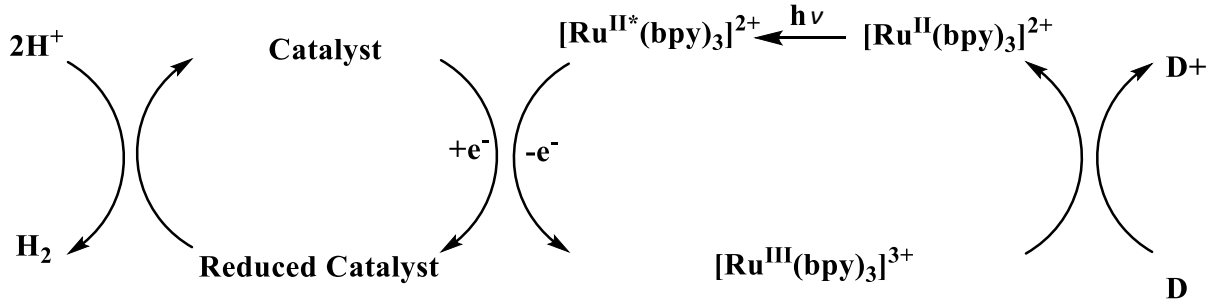

Figure 1.2. A schematic representation of the proton reduction mechanism using $[Ru^{II}(bpy)_3]^{2+}$ as a photosensitizer.

1.2.2. Monometallic Cobalt Catalysts

The first proton reduction catalyst was a cobalt diglyoxime complex reported by Connolly & Espenson in 1986.[17] Since then this field has expanded tremendously to include many different classes of ligands such as polypyridines,[18] dithiolines,[19] porphyrins,[20] phenolates[9] and phosphines,[21] as well as different 3d metals such as iron,[22] cobalt,[14, 23-24] nickel,[25-28] copper[29-31] as well as 4d and 5d metals such as platinum[32] and molybdenum[18-19, 33]. Herein is a brief survey of the literature with special emphasis on the mechanistic aspects of ligand involvement in the catalytic cycle for monometallic cobalt catalysts, and what is known about the cooperativity of different metals for homobimetallic cobalt catalysts.

Although the nominal "[Co^{I}]" is generally thought of as the active form of the catalyst, the ligand is often found to be involved in the catalytic cycle. In general, ligand involvement can occur in two different ways: (i) the ligand can be protonated during the catalytic cycle and act as a proton relay which facilitates the formation of hydrogen, or (ii) ligand-based reduction to form [$Co^{II}L^{\bullet}$] can compete with metal-based reduction. In the latter case the ligand acts as an electron reservoir where reducing equivalents are stored. This can possibly have deleterious effects on catalysis.

Cobalt oxime complexes are some of the most studied proton reduction catalysts.[13, 34-46] Given the wide-scale adoption of oximes as catalytic platforms, their mechanism has been studied in great detail. Although the general reduction mechanism discussed earlier still applies for oximes, Artero *et. al.* have reported another possible catalytic pathway that was probed using DFT calculations. **Figure 1.3** shows the proposed alternative pathway in which following the formation of the five-coordinate [Co^{I}], the ligand is protonated at one of the oxygens of the oxime.[47] Following this step, another proton step takes place to form an octahedral [Co^{III}-H^{-}] along with the protonated ligand. A one-electron reduction then generates the five-coordinate [Co^{II}-H-LH] transition state, where the two protons are combined to form a bound hydrogen molecule. An attack by acetonitrile releases hydrogen gas and regenerates the [Co^{II}] species.

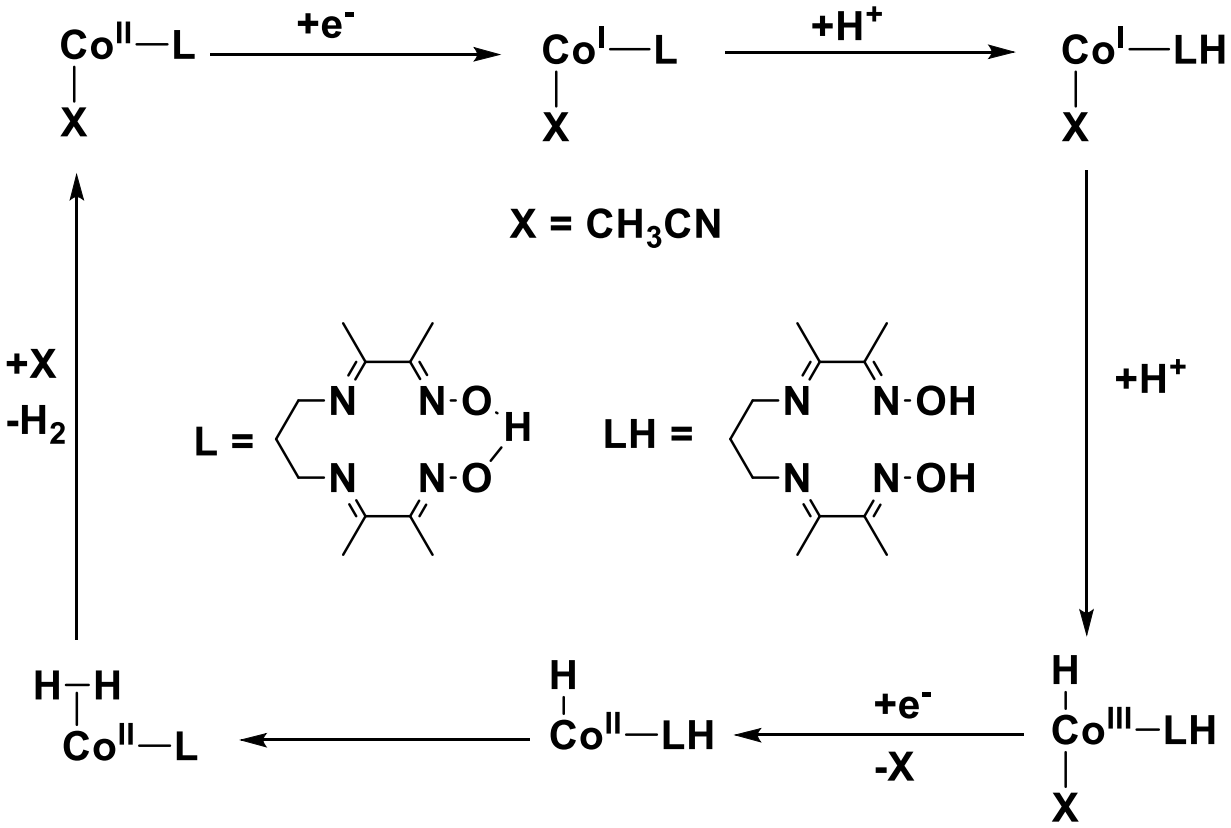

Figure 1.3. The alternative protonation pathway proposed by Artero *et al.*[47]

The Verani group has made significant contributions in the study of ligand involvement in the catalytic cycle. We have recently studied the catalytic activity of a series of heteroaxial cobalt oxime catalysts where one of the axial positions was occupied by a chloride, while the other was occupied by a substituted pyridine on the 4 position (**Figure 1.4.**).[12] The three substituents that were studied were *t*-butyl (**Figure 1.4a.**), pyrrolidine (**Figure 1.4b.**), and benzoyl (**Figure 1.4c.**) functionalities.

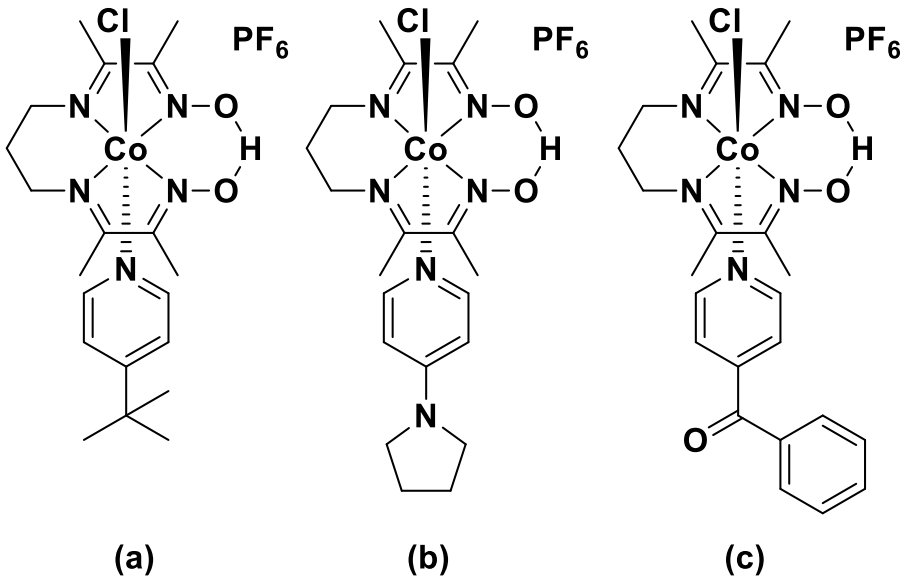

Figure 1.4. The series of heteroaxial cobalt oxime complexes studied by Verani *et al.*

All three catalysts had a similar overpotential (0.35-0.36 V) in acetonitrile with 10 equiv. of trifluoroacetic acid (TFA) as a proton source. However, there was a marked difference in catalytic activity between the three catalysts. While the benzoyl and pyrrolidine substituted catalysts gave a TON of 14 following 3 hours of electrolysis, the *t*-butyl substituted catalyst gave a TON of 19 following three hours of catalysis. It is worth noting that a maximum TON of 50 can be achieved given the amount of acid present.

Due to the relatively high activity of the *t*-butyl substituted catalyst we studied its mechanism in more detail. The catalytic wave in the presence of TFA occurs at a potential that is

very close to the Co^{II}/Co^{I} potential. This supports a mechanism that involves [Co^{I}] reacting with H^{+} to yield [Co^{III}-H^{-}]. Optimizing the [Co^{I}] structure using DFT revealed that (i) the structure of [Co^{I}] is five-coordinate with a pyridine in the axial position, and (ii) the energy difference between the metal-centered and ligand-centered reduction processes is only 3.7 kcal/mol (**Figure 1.5.**).

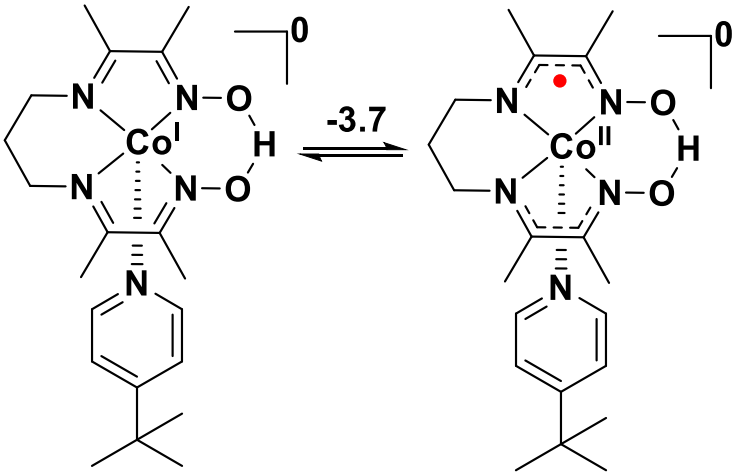

Figure 1.5. The DFT calculated energy difference between the ligand- and metal-centered reduction process.

The value of 3.7 kcal/mol is within the error of the DFT method. In order to support this model experimentally, we attempted to chemically isolate [Co^{I}] utilizing decamethylcobaltocene as a stoichiometric reducing agent.[15] The presence of pyridine in the reduced structure was confirmed using NMR spectroscopy. Moreover, we were able to obtain X-ray quality crystals from the NMR solvent. Solving the crystal structure revealed the unexpected formation of an oxime dimer through the methyl groups (**Figure 1.6.**). While the obtained structure does not provide a direct observation of the ligand-based radical, it does provide indirect evidence to its presence as part of the catalytic cycle.

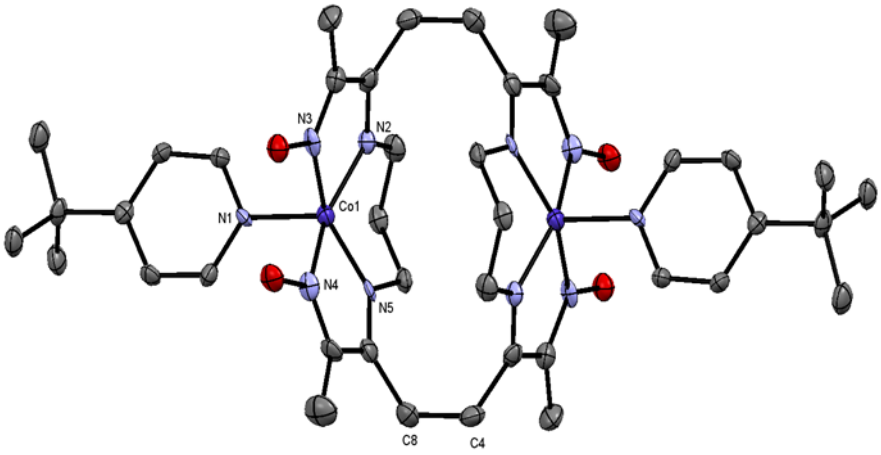

Figure 1.6. ORTEP representation of the crystal structure for the neutral dimer (CCDC 1448834) at 50% ellipsoid probability. Hydrogen atoms omitted for clarity. Co(1)–N(1) = 1.997(4); Co(1)–N(2) = 1.902(4); Co(1)–N(3) = 1.866(4); Co(1)–N(4): 1.850(4); Co(1)–N(5) = 1.890(4); C(4)–C(8) = 1.592(6).

Because one of the main conclusions of the oxime catalyst was that the active [Co^{I}] species is five coordinate where the pyridine is conserved, we reported on a modified ligand design in which the fifth coordination site is incorporated into the main ligand framework (**Figure 1.7.**).[11] Interestingly, upon complexation water was incorporated over one of the imine bonds leading to partial ligand hydrolysis.

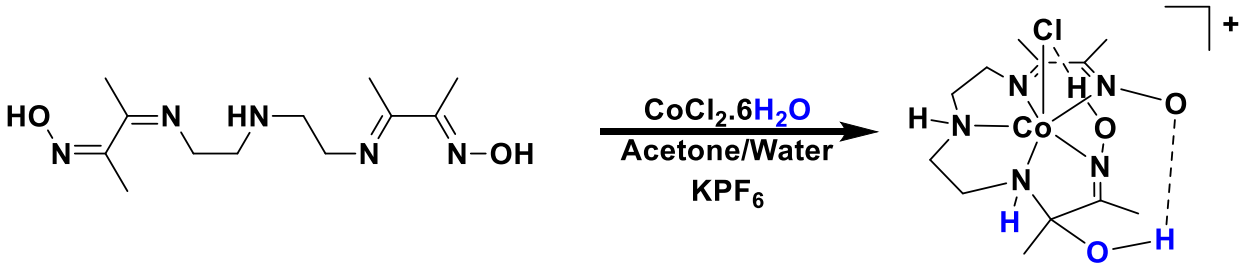

Figure 1.7. The pentadentate oxime-based catalyst reported by Verani *et al.*

In acetonitrile, an overpotential of 0.24 V was observed using acetic acid as a proton source. Following 3 hours of catalysis, a TON of 15 was observed (maximum possible value is 50 given the amount of acid present in solution). However, unlike the previous oxime catalysts the new catalyst is water-soluble which allowed for the study of its water reduction capabilities. Using phosphate buffer (1 mol/L, pH 7) as the reaction medium, an onset overpotential of 0.65 V and an observed TON of 5700 following 18 hours of catalysis were obtained. Interestingly

though, while the molecular nature of the catalyst was retained in acetonitrile, the formation of Co-based nanoparticles was observed under aqueous conditions. The formation of these nanoparticles likely proceeded through further ligand hydrolysis during the catalytic cycle. These results indicate that the interactions of the ligand with the solvent system during catalysis can have deleterious effects on the catalyst and need to be taken into account in the ligand design.

Long, and Chang *et al.* have investigated extensively the use of polypyridine ligands for proton reduction.[5, 48-50] Having studied the activity of redox inactive ligands for proton reduction (**Figure 1.8.)**,[48] they hypothesized that using redox active ligands would improve the catalytic activity by providing an alternative pathway for the catalytic mechanism.[50] With this in mind they modified their ligand design to include two redox active bipyridine chelating groups (**Figure 1.9.**).[51] Moreover, the bipyridine moieties are expected to resist hydrogenation due to their aromatic nature. Both the Zn and Co complexes revealed two reduction processes at similar potentials that are assigned as $bpy^{0/\bullet-}$. For Co these processes occur following a metal-centered $Co^{II/I}$ reduction process. The titration of acetic acid into the solution revealed the presence of a catalytic wave with a reduction potential that is in between the metal- and ligand-centered processes. This suggests that the ligand is involved in the catalytic cycle. Moreover, under similar catalytic conditions the redox active complex (**Figure 1.8.**) achieves TONs that are 6 times higher than its redox inactive counterparts (**Figure 1.9.**).

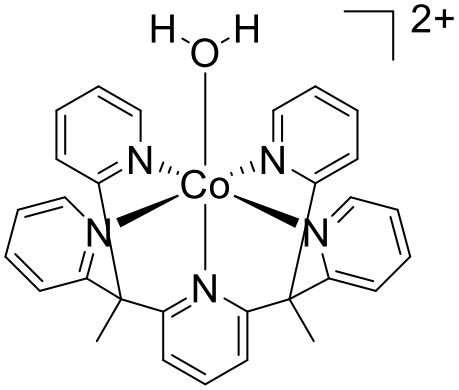

Figure 1.8. The redox inactive catalyst utilized by Chang and Long *et al.*[48]

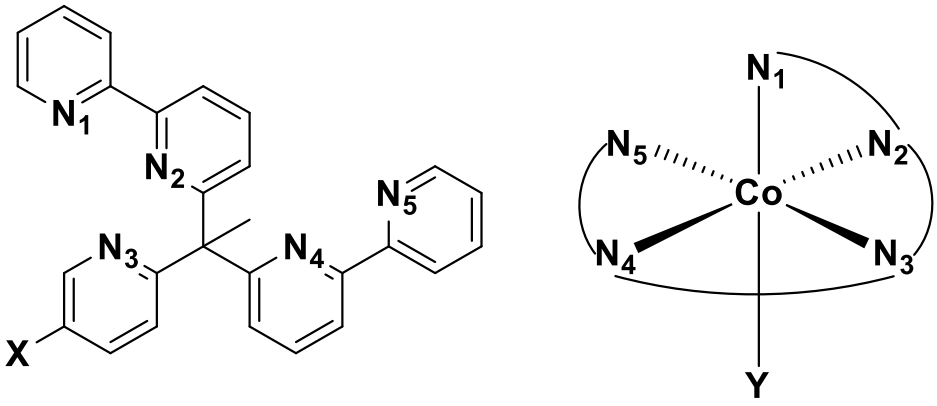

X = H or CF_3

Y = $SO_3CF_3^-$

Figure 1.9. The redox active ligand design utilized by Chang and Long *et al.* as well as a schematic representation of the coordination mode of the catalyst.

The Verani group has extensive expertise in phenolate chemistry.[9, 52-59] Building on previous investigations, the catalytic activity of a cobalt-based complex in an N_2O_3 environment was studied (**Figure 1.10.**).[9] Upon complexation, the amine moiety is oxidized to form a redox active imine group in the complex.

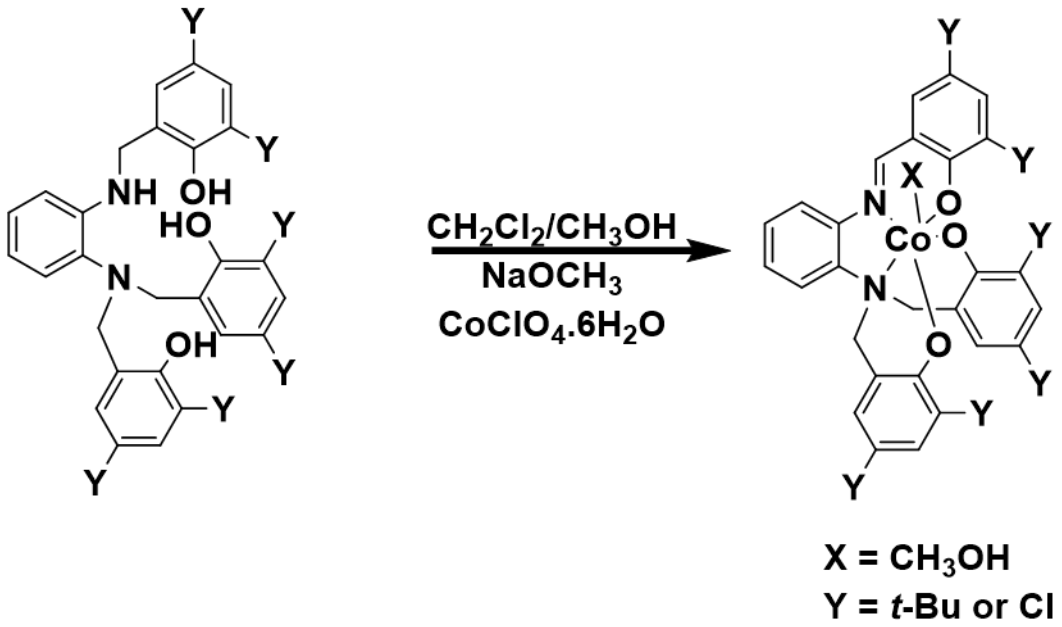

Figure 1.10. The synthesis of the phenolate-based catalyst reported by Verani *et al.*

The CV of the phenolate metal complexes revealed three oxidation processes that are assigned as phenolate to phenoxyl radical conversions, and two reduction processes that are assigned as a Co^{III}/Co^{II} conversion and an imine to imino radical conversion. Interestingly, although the nature of these metal complexes precludes the observation of a Co^{II}/Co^{I} process, upon acid titration using acetic acid as a proton source, a catalytic wave was obtained close to the second reduction process (ascribed to imine reduction). The two complexes that were studies had relatively high overpotentials: 0.6 V for the chloro-substituted complex and 0.9 V for the *t*-Bu substituted complex. These results point to one of the rare examples of unquestionable ligand involvement in the catalytic cycle where the imine moiety is acting as an electron reservoir.

The hard nature of phenolates likely destabilizes [Co^{I}] and makes the formation of hydrogen more energetically demanding, thereby accounting for the high overpotentials. To address this issue, we modified the ligand design to incorporate softer pyridine donors in place of the harder phenolate donors (**Figure 1.11.**).[10] However, during the complexation process the ligand underwent drastic rearrangement to produce imine and methanol incorporated intermediates. These intermediate species finally converged to the thermodynamically stable amide product. In order to avoid ligand rearrangement during synthesis, the amine group was substituted with a methyl group (**Figure 1.11. inset**). This change in ligand design lead to the 'clean' formation of the Co complex.

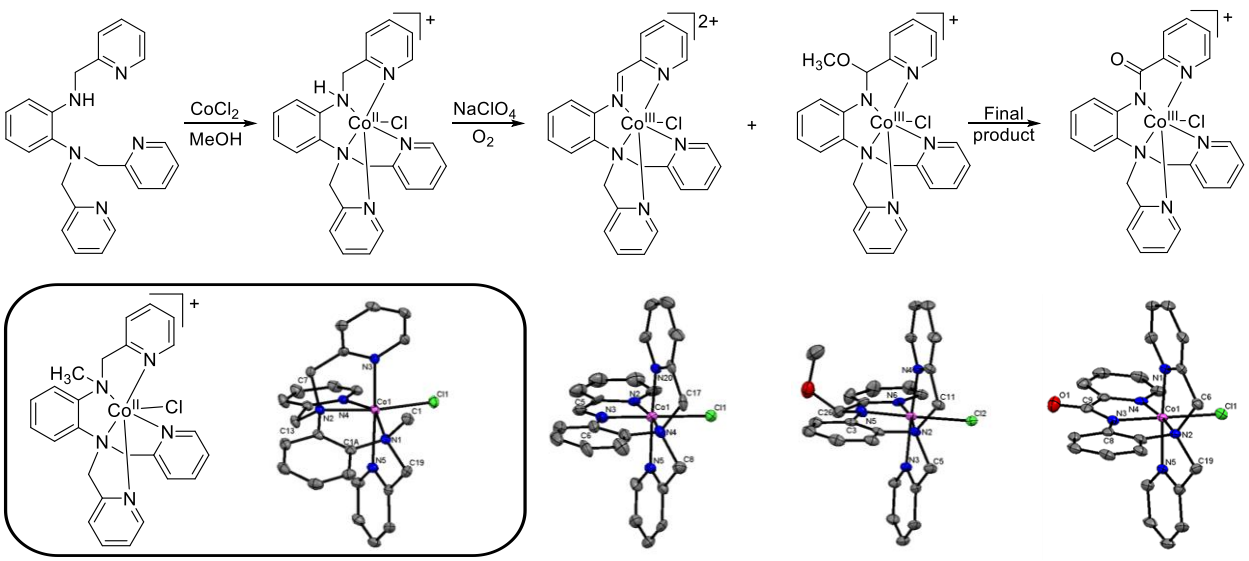

Figure 1.11. The polypyridine catalysts studied by Verani *et al.*

Since both the amido and *N*-methyl complexes proved water soluble, their catalytic activity was studied in phosphate buffer (pH 7, 1 mol/L). The transient nature of the imine and methanol-incorporated complexes precluded catalytic analysis. On the one hand, while the amido complex was synthesized *via* ligand rearrangement, it had an onset overpotential of 0.55 V and underwent 7000 turnovers following 18 hours of catalysis. On the other hand, the N-methyl complex was synthesized as designed. However, it had a higher onset overpotential of 0.70 V

and a lower TON of 6000 following 18 hours of catalysis. These observations will provide the inspiration for the amidopyridine ligand design discussed in Chapter 3.[60]

1.2.3. Bimetallic Catalysts

The hydrogenase enzyme utilizes an active site that consists of a bimetallic core. However, the use of bimetallic metal complexes as proton reduction catalysts has remained a field that is relatively unstudied. Peters *et al.*[61] studied the catalytic activity of a pyridazine-templated homobimetallic cobalt macrocycle (**Figure 1.12.a**). Due to the electronic coupling between the two metal centers, they focused on the structural variations upon reduction by isolating the [Co^{III}-Co^{III}], [Co^{III}-Co^{II}], [Co^{II}-Co^{II}], and the [Co^{II}-Co^{I}] crystal structures. Using spectroscopic studies, they concluded that the [Co^{I}-Co^{I}] forms H_2 whereby two [Co^{III}-H^{-}] species react independently to form H_2.

Dinolfo and coworkers[62] studied the catalytic activity of a macrocyclic N_6O_2 [Co^{II}-Co^{II}] complex **Figure 1.12.b**. However, [Co^{II}-Co^{I}] was not catalytically active; instead catalysis was initiated at potentials that are negative enough to produce [Co^{I}-Co^{I}]. Based on this observation, a mechanism with two possible pathways was postulated. In the first, the formation of two hydride species [H-Co^{III}-Co^{III}-H] was proposed. In this pathway, both metal centers are involved in catalysis. In the second pathway, the formation of a [Co^{II}-Co^{II}-H] intermediate was proposed. In this case one of the cobalt centers is actively involved in catalysis, while the other metal center is acting as an electron reservoir. Based on the experimental results presented in this work it was not possible to distinguish which pathway is preferred.

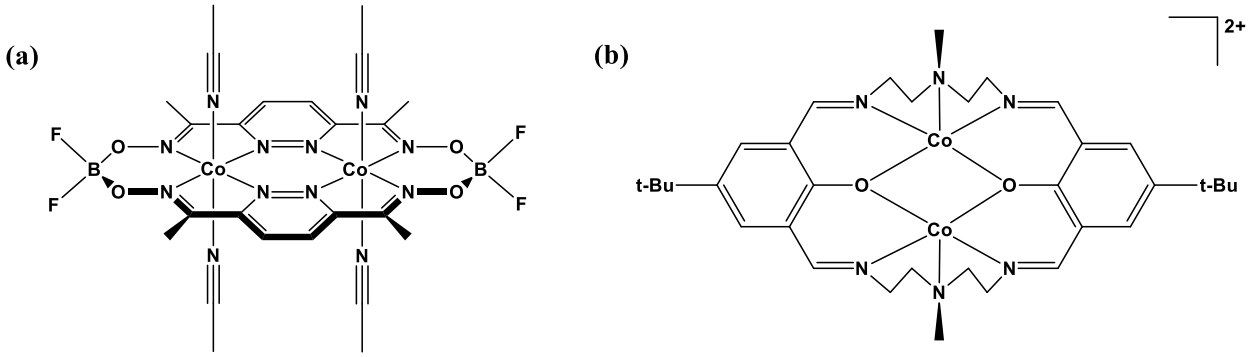

Figure 1.12. The bimetallic catalysts reported by (a) Peters *et al.* and (b) Dinolfo *et al.*

Gray and *et al.*[63-64] used two different linkers to bring two oxime-based active sites closer to each other. The first linker consisted of a C_8 alkyl chain (**Figure 1.13.a**)[63] producing a net effect comparable to using twice the concentration of the monometallic catalyst. This observation is consistent with catalysis through a heterolytic pathway. Interestingly, when the much shorter BO_4^- bridge was utilized (**figure 1.13.b)** electronic coupling between the two metal centers was observed.[64] However, the bridged catalyst operated at a higher overpotential than its monometallic counterpart.

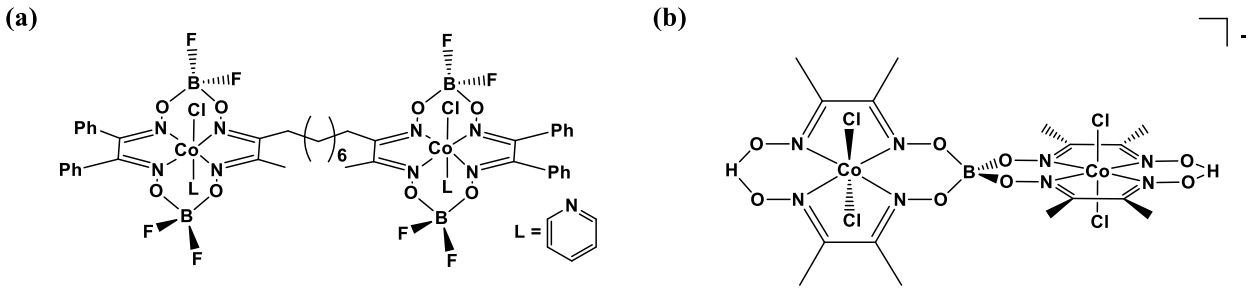

Figure 1.13. The bimetallic catalysts reported Gray *et al.*

Fukuzumi and coworkers in turn utilized a pyrazolate bridging moiety to chelate two separate cobalt centers and form a [Co^{III}-Co^{III}] metal complex (**Figure 1.14.a**).[16] By using cobaltocene and decamethylcobaltocene as stoichiometric reducing agents they could isolate the reduced [Co^{II}-Co^{I}] and [Co^{I}-Co^{I}] species. Following the reaction kinetics of these reduced intermediates with TFA using stopped flow spectroscopic techniques, they concluded that even

when the two metal centers are in closer proximity, a heterolytic pathway is still favored over a homolytic pathway.

More recently, Llobet *et al.*[65] used a decadentate ligand capable of supporting two cobalt centers in close proximity (**Figure 1.14.b**). The reported species were capable of performing photocatalytic proton reduction in acetonitrile. However, the mechanistic results discussed by the authors suggest that the two metal centers perform catalysis independently of each other.

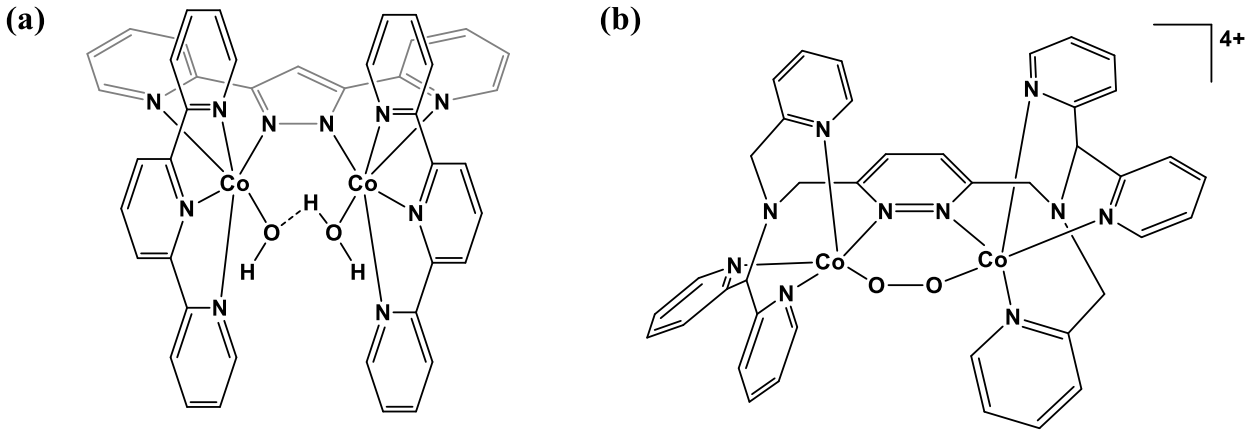

Figure 1.14. The bimetallic catalysts reported by (a) Fukuzumi *et al.* and (b) Llobet *et al.*

The Verani group, in collaboration with the Fiedler and Schlegel groups,[66] has recently reported a [Co^{II}-Co^{II}] catalyst that uses an NN'O_2 fused bridging ligand (**Figure 1.15.**). The results indicate that catalysis only proceeds following a two-electron reduction to form [Co^{I}-Co^{I}]. Experimental evidence in conjunction with DFT calculations suggest that upon the reaction of the [Co^{I}-Co^{I}] species with H^+, one of the reduced cobalt centers reacts to form the catalytically active [Co^{III}-H^-] species while the other center acts as an electron reservoir, shuttling an electron. Therefore, the active species that is formed consists of a [Co^{II}-Co^{II}-H^-] instead of [Co^{I}-Co^{III}-H^-] or a [$^-$H-Co^{III}-Co^{III}-H]. Using this mechanism, the [Co^{III}-H^-] that is associated with most proton reduction mechanisms is avoided. **Chapter 4** will discuss the catalytic activity of a novel homobimetallic cobalt catalyst based on the amidopyridine ligand framework discussed in

Chapter 3. This catalyst is the first example where the activity of the bimetallic catalyst is demonstrably better than using a monometallic catalyst.

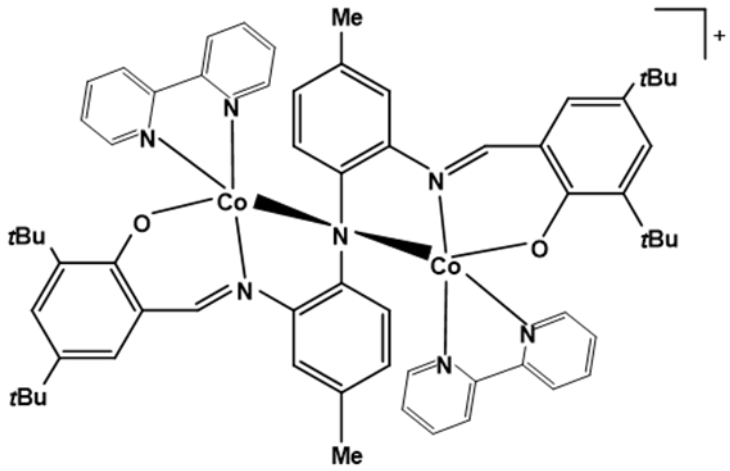

Figure 1.15. The bimetallic catalyst reported by Fiedler, and Verani *et al.*

1.3. Water Oxidation Catalysts

Due to the energetic demands of transferring four protons and four electrons as well as forming oxygen-oxygen bonds, the water oxidation reaction requires the presence of metal catalysts. These requirements impart a high energetic requirement for water oxidation equivalent to ~ 56.6 kcal/mol (237 kJ/mol, or 1.23 V_{NHE}). Although the mechanisms of water oxidation have yet to be fully elucidated for most metal complexes, in general they all require the formation of high valent oxo ([M^{iv}=O], or [M^{v}=O]). Following the formation of these species, two possible mechanisms can take place. In the first mechanism, H_2O acts as a nucleophile and attacks the electrophilic [M=O] species. This leads to the formation of a metal-hydroperoxo species [M-OOH] which can be subsequently oxidized to release oxygen gas. In the second mechanism, two [M=O] species with significant radical character on the oxygens undergo coupling and lead to the formation of a binuclear metal complex with an [M-O-O-M] bridge (**Figure 1.16.**)

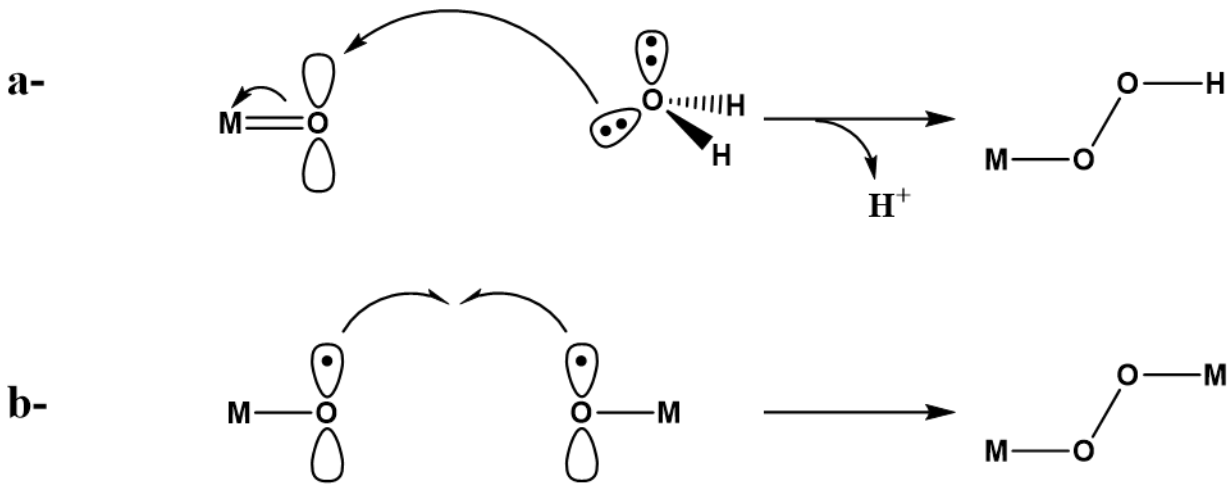

Figure 1.16. The (a) water nucleophilic attack and (b) radical coupling mechanisms.

Molecular water oxidation catalysis can be performed by using (i) chemical oxidants, (ii) photosensitizers, and/or (iii) an applied electrochemical potential. One of the most common chemical oxidants for water oxidation is ceric ammonium nitrate, or CAN ($Ce(NH_4)_2(NO_3)_6$). CAN is a one-electron oxidizing agent that has an oxidizing potential of 1.82 V_{NHE} that operates according to (**equation 1.6**) and can be used to quickly and efficiently screen a variety of water oxidation catalysts. However, the use of CAN requires highly acidic media (pH < 1) which limits the number of catalysts that can be stably screened using this method.

$$4Ce^{IV} + 2H_2O \rightarrow 4Ce^{III} + O_2 + 4H^+ \qquad \textbf{(equation 1.6)}$$

Photochemical water oxidation takes by using a photosensitizer such as tris(bipyridine)ruthenium(II) ($[Ru^{II}(bpy)_3]^{2+}$) as a photosensitizer (**Figure 1.17.**). Upon irradiation with a light source of an appropriate wavelength $[Ru^{II}(bpy)_3]^{2+}$ gets excited to $[Ru^{II*}(bpy)_3]^{2+}$ which then reacts with a sacrificial oxidant such as $Na_2S_2O_8$ to yield $[Ru^{III}(bpy)_3]^{3+}$ which acts as a one-electron oxidant at a potential of 1.21 V_{NHE}.

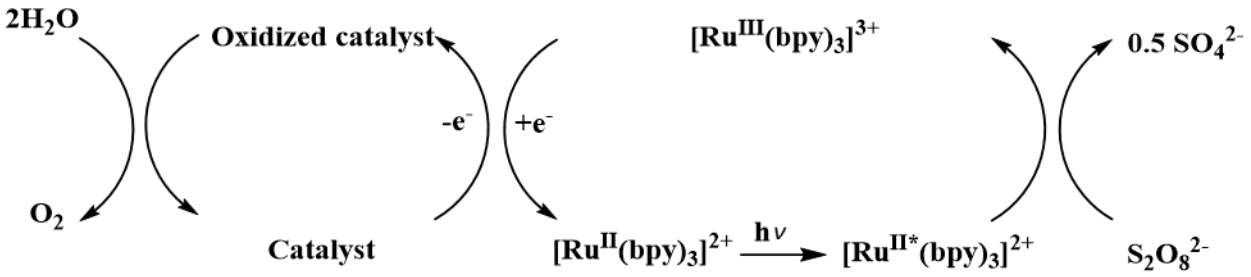

Figure 1.17. A schematic representation of the water oxidation mechanism using $[Ru^{II}(bpy)_3]^{2+}$ as a photosensitizer.

The final method by which water oxidation catalysts are commonly screened is by applying an electrochemical potential. During electrochemical water oxidation, an electrode (usually glassy carbon or fluorine-doped tin oxide (FTO) glass) is placed in a standard three-electrode cyclic voltammetry setup. The potential is scanned, and water oxidation is detected by the appearance of a catalytic wave at a potential where the blank is inactive. This has the advantage of quick screening of a large number of catalysts under a variety of conditions, such as pH and supporting electrolyte. However, one drawback of this method is that catalysis only takes place at the surface of the electrode, and therefore most of the catalyst in solution is not utilized. Moreover, the presence of an electrode can foster the formation of nanoparticles or metal oxide films on the surface. Therefore, the exact nature of the source of catalysis needs to be investigated.

The seminal work by the Meyer group[67] in 1982 on the "blue dimer" which is a bimetallic μ-oxo bridged ruthenium complex (**Figure 1.18.a**) showed for the first time that molecular species can indeed catalyze water splitting. Then Thummel *et al.*[68] showed that mononuclear ruthenium complexes can also catalyze water oxidation (**Figure 1.18.b**). More recently, water oxidation using 3d transition metal complexes has gained traction as a more cost-effective alternative. **Figure 1.19.** shows a selection of molecular catalysts based on Mn, Fe, and Co.[20, 69-74] Since the present work (**Chapter 5**) deals with the attachment of molecular catalysts

on the surface of solid supports, rather than solution-based catalysis, the following section (**1.4**) will expand on the modes of surface functionalization.

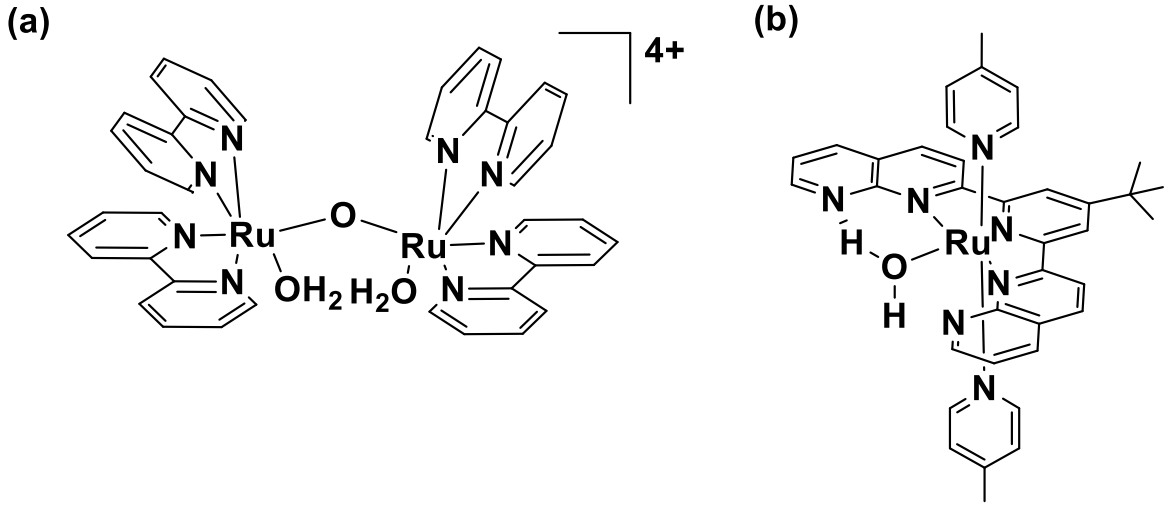

Figure 1.18. The catalysts reported by (a) Meyer *et al.* and (b) Thummel *et al.*

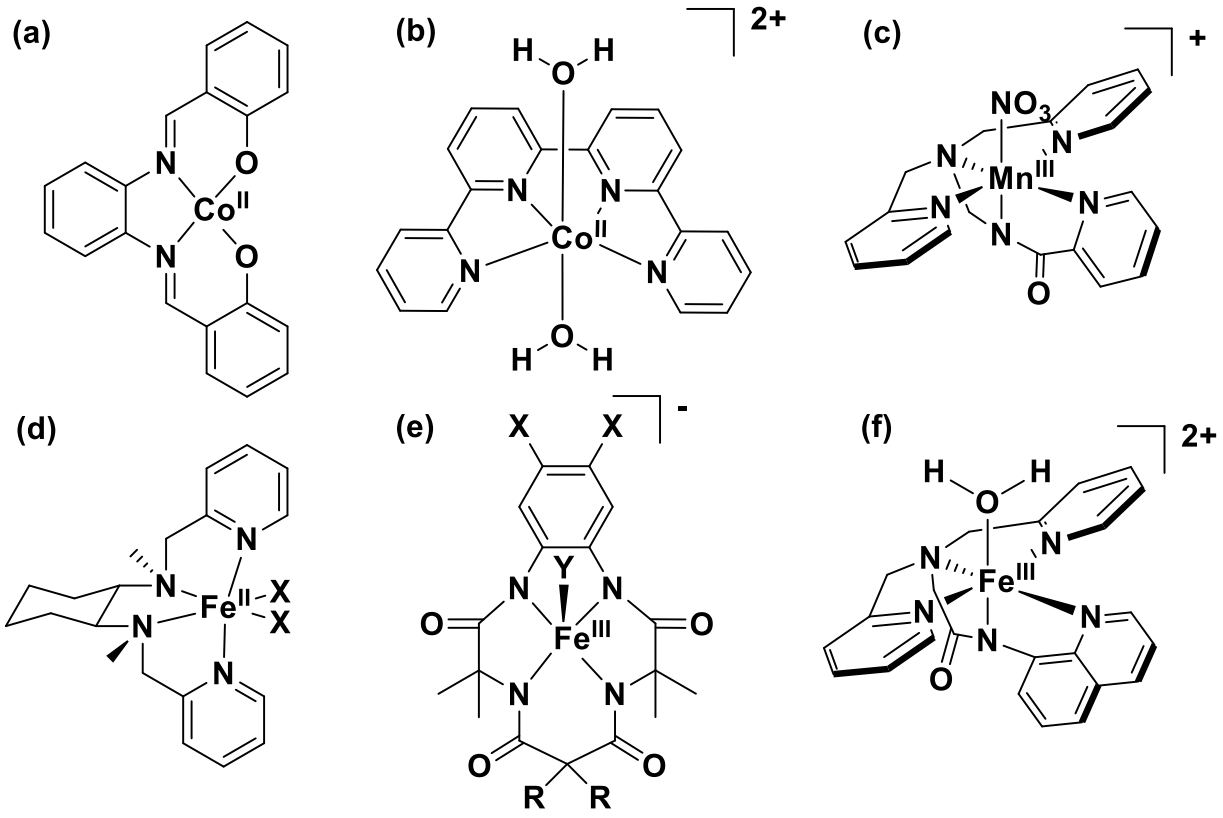

Figure 1.19. A selection of Earth abundant catalysts reported by (a) Sarotel *et al.*[70], (b) Lau *et al.*[69], (c) Brudvig *et al.*[71], (d) Costas *et al.*[72], (e) Collins *et al.*[73], and Meyer *et al.*[74]

1.4. Surface Functionalization Using Molecular Catalysts for Water Splitting

Translating homogenous solution-phase catalysts into effective heterogenous systems requires the development of methods to deposit homogenous catalysts onto conductive solid supports.[75-78] Following surface functionalization, integrated electrochemical water splitting devices can be developed, in which water oxidation occurs at the anode and proton reduction occurs at the cathode.[1] Traditionally, such electrodes are made from solid state materials such as metal oxides, phosphates, or hydroxides.[79-80] However, understanding the surface chemistry of such materials is very challenging. Surfaces functionalized with coordination complexes pose much less of a challenge in this regard. To this end surfaces can be functionalized using either chemisorption where a direct chemical bond between the molecule and the surface is formed, or physisorption where the molecule is attached to the surface using intermolecular forces.

Chemisorption can be achieved by functionalizing the molecule with an anchoring group that forms a chemical bond to the surface. The surface in this case generally consists of a conductive metal oxide, and the linkage is achieved using an oxygen-rich functionality such as phosphonate or acetate groups.

The Schmuttenmaer, Brudvig, and Crabtree groups have recently reported on an iridium catalyst that can be anchored onto the surface of ITO at room temperature in water without the need to functionalize the molecular catalyst with any linking groups (**Figure 1.20.**).[78] The linkage took place *via* a substitution of the coordinated water molecules with the terminal surface-bound oxide species. This allowed for the formation of a direct bond from the conductive oxide surface to the iridium metal center. The catalytic film was found to be highly active towards water oxidation requiring overpotentials as low as 160 mV to reach a current density of

0.5 mA/cm^2. XPS analysis before and after catalysis confirmed the molecular nature of the catalyst.

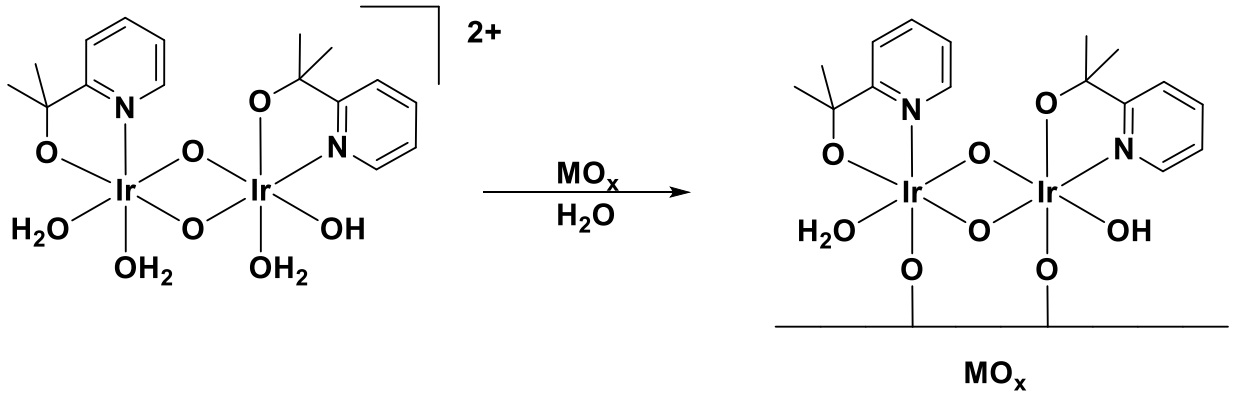

Figure 1.20. The chemisorption of the bimetallic iridium catalyst on the surface of ITO as reported by Schmuttenmaer, Brudvig, and Crabtree *et al.*

Since physisorption does not require the formation of a direct chemical bond between the catalyst and the conductive surface, the molecule is attached to the surface using intramolecular forces. One of the most common intermolecular forces used for catalyst deposition is π-π stacking. π-π stacking is an intermolecular force in which aromatic rings on different molecules have an attractive interaction between each other.[81] As such for this force to be useful substrates containing extensive aromatic systems such as graphite,[82-83] graphene,[84] or carbon nanotubes (CNTs)[46, 76, 85] need to be used. Moreover, the molecule in question needs to have an extensive π system[46, 85-86] to act as the anchor.

Pyrenes represent one of the most widely used anchoring moieties.[87] Cao *et. al.* anchored a cobalt-based pyrene-functionalized corrole to the surface of CNTs (**Figure 1.21.**). Corrole-CNT hybrid material can catalyze the water oxidation reaction at an onset overpotential of 0.33V. Control experiments using a structurally related complex in which the pyrene was replaced with a pentafluorophenyl moiety revealed that the pyrene substituent through its strong π-π interaction plays an important role in facilitating electron transfer and therefore improved the catalytic activity.

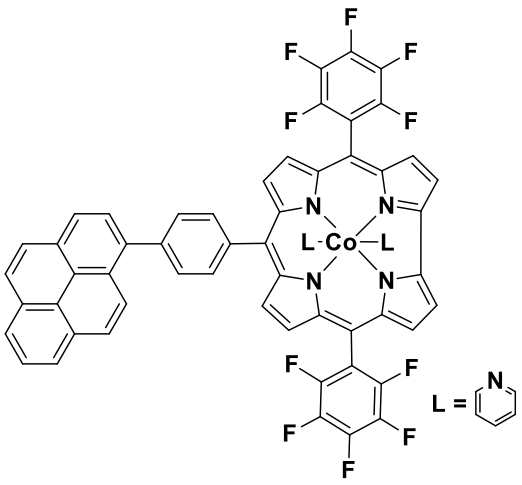

Figure 1.21. Cobalt-based pyrene-functionalized corrole used by Cao *et al.*

Sun *et. al.* have extensively studied the use of ruthenium-based picolinate complexes as efficient water oxidation catalysts.[88-93] Building upon their extensive experience with the ligand system, they functionalized the axial ligand with pyrene moieties which allowed the catalyst to be anchored onto the surface of CNTs (**Figure 1.22.a**).[76] At a pH of 7, the functionalized CNTs were capable of catalyzing water oxidation an at onset overpotential of 0.3 V and yielded a TOF of 1100 h^{-1}. The molecular nature of the catalysis was ascertained by the stability of the redox behavior of the surface-bound molecules before and after catalysis.

In another study, Sun *et. al.* showed that CNTs can also be functionalized using a dodecyloxy substituted Ru WOC (**Figure 1.22.b**).[77] The electron donating effect of the alkoxy substituent had a moderating effect on the $Ru^{III/II}$ redox potential making it less positive. At pH 7 the functionalized CNTs showed an onset of catalytic current at 1.2 $V_{NHE,}$ which corresponds to an overpotential of 0.38 V. Although the catalyst had a high initial activity which allowed it to achieve a TOF of 7.6 s^{-1} following 1 hour of electrolysis, the activity decreased over time to reach a TOF of 3.5 s^{-1}. Nonetheless, this decrease in activity is represents a significant improvement on the stability of the catalyst before it was anchored onto the surface of CNTs.[94]

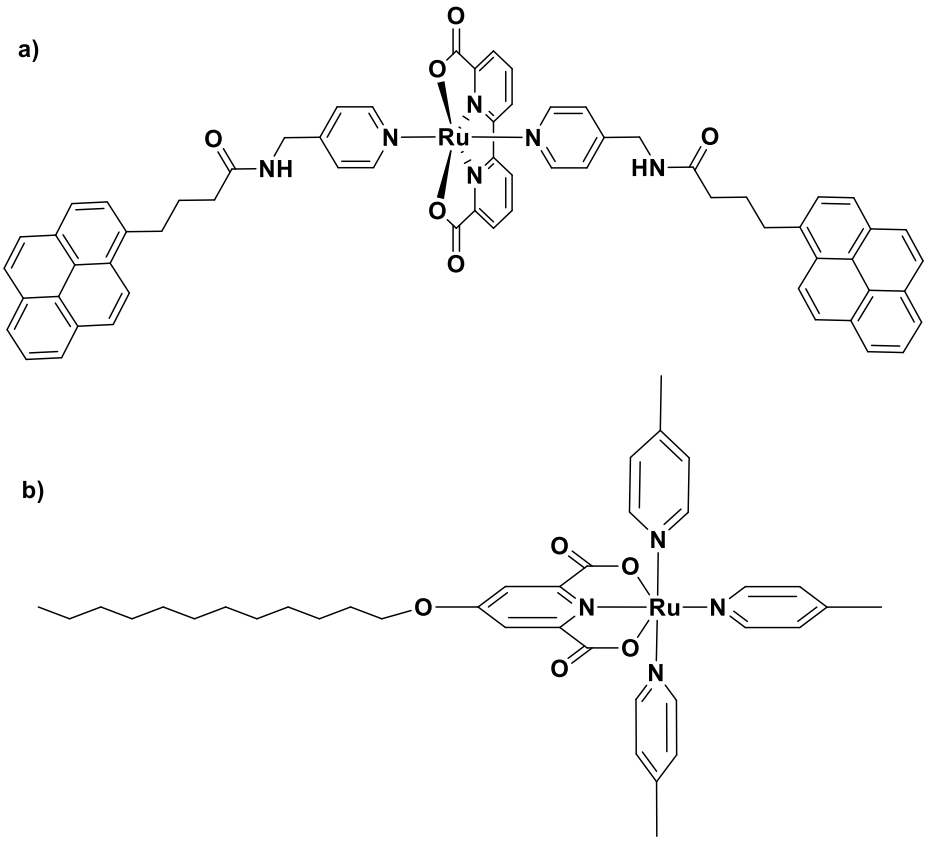

Figure 1.22. The ruthenium-based picolinate complexes studied by Sun *et al.*

Aiming at the functionalization of the surface of conductive metal oxides using physisorption, we have recently reported on the first usage of Langmuir-Blodgett films to drive catalytic water oxidation.[75] This was achieved by utilizing a trisphenolate amphiphilic ligand that

we have used extensively before for the purposes of molecular electronics[55-56, 58-59] and replacing the iron(III) metal center with a cobalt(III) metal center (**Figure 1.23**).

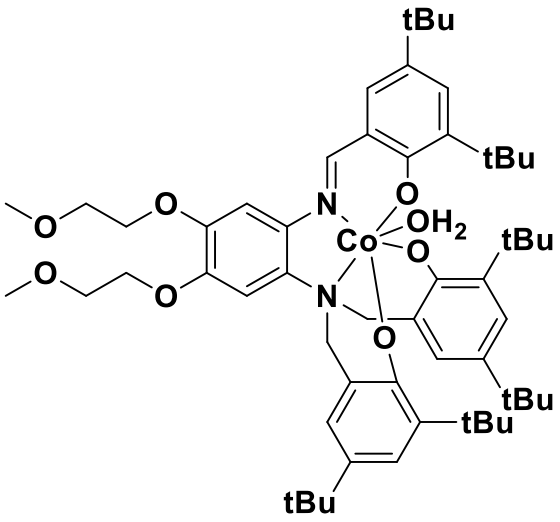

Figure 1.23. The amphiphilic cobalt precatalyst used in the Langmuir-Blodgett films on FTO.

One of the advantages of the Langmuir-Blodgett method is that uniform conformal coverage is provided and the number of deposited layers can be accurately varied. Therefore, the effect of having multilayers as opposed to having monolayers can be studied. As such, mono and multilayers (1-13 layers) of the cobalt metallosurfactant were deposited onto the surface of fluorine-doped tin-oxide (FTO) using the Langmuir-Blodgett method.

Increasing the number of deposited layers was found to have a positive effect on the catalytic activity of the functionalized FTO electrode only up to 9 deposited layers. More layers did not improve activity. For a monolayer, we were able to estimate the turnover number based on the average molecular area occupied by a singly cobalt molecule (this value can be obtained from the LB method) and we obtained an observed TOF of 5400 ± 1500 h^{-1}.

However, we were unable to ascertain the molecular nature of the catalyst using XPS analysis due to the extremely small amount catalyst on the surface. We therefore had to infer the nature of the active species from standard experiments. Cycling the electrode 100 times leads to

a marked enhancement in the catalytic current (**Figure 1.24.**). Moreover, rinsing the surface of the electrode with organic solvents before electrolysis lead to the formation of inactive electrode; however, rinsing the surface of the electrode following electrolysis did not diminish the catalytic activity of the electrode. These results point to the rearrangement of the catalyst on the surface of the electrode. Although we were unable to directly measure the nature of the rearranged species, we assume that it is similar to that obtained by Du et. al.[95] where structurally related cobalt complexes decomposed on the surface of FTO to produce catalytic cobalt oxide films.

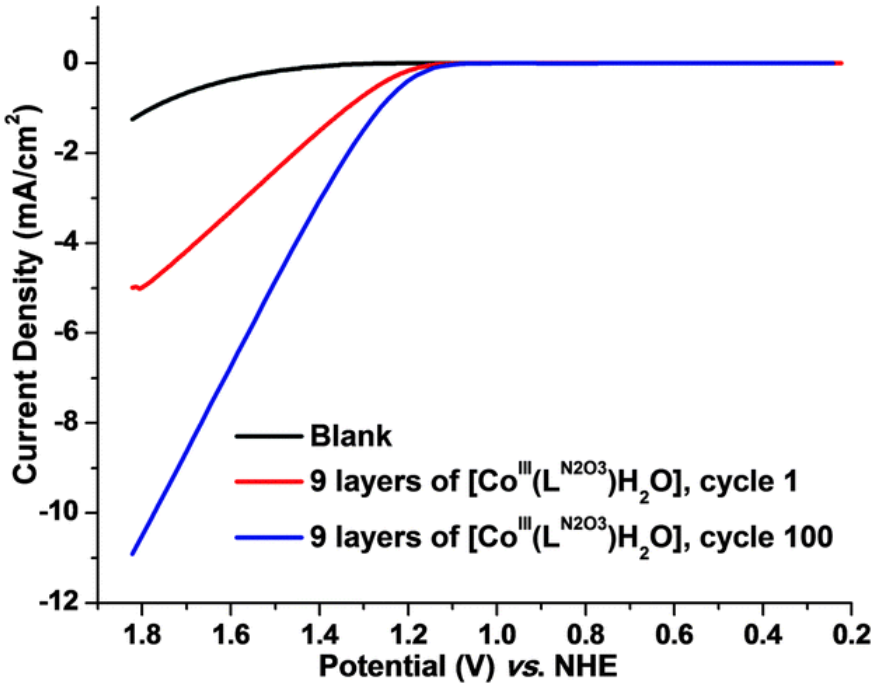

Figure 1.24. The polarization curves obtained for 9 LB layers during the 1st cycle and the 100th cycle.

1.5. Research Statement and Objectives

Research in the Verani group focuses on the study of the electrochemical, physical, and structural aspects of coordination metal complexes. The knowledge that is gained from these basic studies are then utilized in the study of molecular systems in the solution phase and on solid substrates (using the Langmuir-Blodgett method) that are geared towards catalysis, molecular electronics, and corrosion mitigation. The research that is discussed in this thesis

borrows aspects from all the general research themes that are pursued in our group. The first project focuses on the study of the catalytic behavior of a new amidopyridine platform towards water reduction catalysis. Given the short lifetime of this species special emphasis is placed on its deactivation pathway. The second project uses the lessons learned from the first project to modify the ligand design and to obtain enhanced catalytic performance. The third project deals with modifying the surface of carbon supports using an octadeceloxy substituted amidopyridine cobalt complex towards water oxidation.

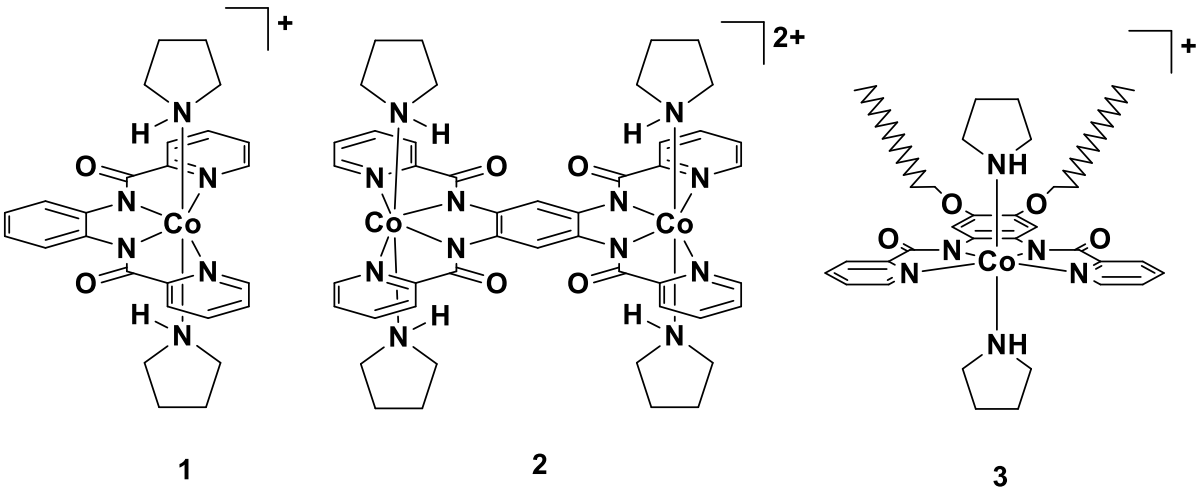

Figure 1.25. The catalysts that are studied in this thesis.

- ***Goal # 1: Deactivation of a Cobalt Catalyst for Water Reduction through Valence Tautomerism.***

Having shown that amidopyridines seem to be enhancing the catalytic activity of cobalt catalysts, in chapter 3 we study the catalytic activity of the water reduction catalyst $[Co^{III}(L^1)(pyr)_2]PF_6$ (**1**), where L^1 is a bis-amido pyridine ligand and pyr is pyrrolidine. Catalyst **1** has an overpotential of 0.54 V and a high observed TOF of 23 min^{-1}, albeit for a relatively short time. Considering the significant activity of **1** and aiming to improve catalyst design, a detailed structural and electronic study is performed to understand the mechanisms of deactivation. Experimental and theoretical evidence support that the metal-reduced $[Co^{I}(L^1)]^-$ is

in tautomeric equilibrium with the ligand-reduced $[Co^{II}(L^{1\bullet})]^-$ species. While $[Co^{I}(L^{1})]^-$ favors formation of a Co^{III}-H^- relevant for catalysis, the $[Co^{II}(L^{1\bullet})]^-$ species leads to ligand protonation, structural distortions and, ultimately, catalyst deactivation.

- ***Goal # 2: Enhanced Catalytic Activity and Activity in a Bimetallic Cobalt Catalysts for Water Reduction.***

The use of bimetallic complexes has been proposed as a means of enhancing the catalytic activity of proton reduction catalysts. Building on the results obtained for **1** we synthesized the homobimetallic counterpart $[(Co^{III})_2L^2(pyr)_4](PF_6)_2$ (**2**) where L^2 is 1,2,4,5-tetrakis(2-pyridinecarboxamido)benzene, the binucleating counterpart of L^1. We show that **2** operates at an onset overpotential that is 0.1 V lower than **1**. Moreover, we show that both **1** and **2** have the same Co^{II}/Co^{I} reduction potential in CH_3CN. These two observations lead us to conclude that **1** and **2** operate using different catalytic mechanisms, where **1** requires the formation of a catalytically active $[Co^{I}]$ while **2** undergoes a PCET process from $[Co^{II}]$ to $[Co^{III}\text{-}H^-]$. This change in mechanism allowed us to avoid the formation of a $[Co^{I}]$ during catalysis, thereby stabilizing the catalyst for prolonged periods of time.

Goal # 3: Immobilization of a Long-Chain Cobalt Amido Complex on Carbon Black for Heterogeneous Water Oxidation.

Chapter 5 will deal primarily with functionalization of the surface of carbon black with the alkoxy-substituted molecular catalyst, $[Co^{III}(L^{OC18H37})(pyr)_2]ClO_4$ (**3**). We show that the oxidation of **3** leads to the formation of primarily ligand-oxidized instead of metal-oxidized species. Then we demonstrate that **3** can be anchored onto carbon black to catalyze water oxidation at an onset overpotential of 0.32 V and can reach a current density of 10 mA/cm^2 at an overpotential of 0.37 V. Moreover, **3** has an observed TOF of 2700 h^{-1} at an applied potential of

0.9 V_{NHE}. XPS analysis suggests that the molecular nature of the catalyst is retained. Finally, a mechanism is proposed based on DFT calculations.

CHAPTER 2. MATERIALS, METHODS, AND INSTRUMENTATION

2.1. Materials

Throughout this thesis several ligands and metal complexes have been synthesized and characterized. All starting materials and solvents needed for synthesis were obtained from commercial sources and used without further purification. For the catalytic studies, ultrapure water (18.1 MΩ) was used. Where necessary, anhydrous solvents were used.

2.2. Methods and Instrumentation

A multitude of techniques were used to accomplish the research being presented in this thesis. The synthesized organic molecules were characterized using Fourier transform infrared spectroscopy (FTIR) in order to ascertain the presence of several key functional groups. Proton nuclear magnetic resonance (^{1}H-NMR) spectroscopy was used to obtain information about the number of protons present within the molecule as well as their local environment. The presence of presumed structures was confirmed using electrospray ionization mass spectrometry (ESI-MS). Metal complexes were also characterized using FTIR, and ESI-MS. Moreover, elemental analyses were used to confirm the purity of the bulk materials. When X-ray quality single crystals could be grown, the crystal structure was determined. For metal complexes the ^{1}H-NMR spectra could only be determined for diamagnetic species. As such, in this research the ^{1}H-NMR spectra of low spin $3d^6$ [Co^{III}] and $3d^8$ [Co^{I}] metal complexes could be readily obtained. However, the spectra of the $3d^7$ [Co^{II}] were not available. Altogether, these techniques allow us to unambiguously determine the chemical structures of the synthesized molecules.

Following this step, several other methods where used to determine relevant properties of the synthesized materials. UV-visible spectroscopy (UV-Vis) was used to reveal the nature of the electronic transitions in the system; cyclic voltammetry (CV) was used to determine the different

redox states that can be stabilized by the metal complexes. Furthermore, spectroelectrochemistry and bulk electrolysis (BE) were used to gain insight about the electronic nature of the complex in different oxidation states. Structural information about the reduced species was acquired by performing chemical reduction followed by isolation of crystals from solution to obtain the X-ray crystal structure. Finally, the catalytic behavior of the metal complexes was determined using CV, BE, and gas chromatography (GC). Where appropriate, density functional theory (DFT) calculations were performed in collaboration with the Schlegel Group at Wayne State University in order to confirm or further explain experimental results.

2.2.1. Fourier Transform Infrared Spectroscopy

Fourier transform infrared spectroscopy (FTIR) spectroscopy is an essential method that can be used to confirm the presence of functional groups in the synthesized molecules. It is especially useful in the determination of the presence of C=O, C=N, C=C, C-H, N-H, O-H and C-O functional groups in the ligands as well as the complexes. Furthermore, counterions such as ClO_4^-, and PF_6^-, have highly characteristic peaks in the IR region that indicate their presence in the synthesized complex; this has important implications in determining the oxidation state of the synthesized complex. FTIR spectra were recorded using KBr pellets in the spectral range of 4000-650 cm^{-1} on a Bruker Tensor 27 FTIR spectrometer.

2.2.2. Proton Nuclear Magnetic Resonance Spectroscopy

Proton Nuclear Magnetic Resonance Spectroscopy (^{1}H-NMR) spectroscopy is used to obtain structural information about the synthesized organic molecules and diamagnetic metal complexes ([Co^{III}] and [Co^{I}] in this thesis). A typical spectrum is obtained as intensity *vs.* chemical shift (ppm). Several structural features can be deduced from an ^{1}H-NMR spectrum. The chemical shift of the obtained peak can be directly correlated to the environment of the proton in

question, and the integration of the peak can be directly correlated to the number of protons being measured.[96] Finally, the splitting pattern of the peak can lead to information about the protons neighboring the proton that is being measured.[96] The spectra are generally recorded in deuterated solvents such as $CDCl_3$, C_6D_6, CD_3CN, and ^{6}d-DMSO.

2.2.3. Mass Spectrometry

Mass spectrometry is a technique that allows us to determine the mass-to-charge ratio (m/z) of samples, thereby confirming our presumed structural assignment. In general, we have employed electrospray ionization mass spectrometry (ESI-MS) in most of our studies. ESI-MS ionizes molecules by applying a high voltage to the solution, leading to the formation of a charged aerosol that is later analyzed by the detector.[97] Organic molecules were analyzed using low resolution MS (LRMS) and the peaks that were obtained were generally of the form $(M+H^+)^+$, or $(M+Na^+)^+$. On the other hand, metal complexes were generally analyzed using high resolution MS (HRMS). The advantage of using HRMS lies in the high precision with which m/z values can be determined. This increased precision allows us to compare the isotopic distribution obtained experimentally to that of the isotopic distribution expected based on the theoretical elemental composition. LRMS spectra were generally obtained on either a ZQ-Waters/Micromass system equipped with a single quadrupole mass spectrometer or a Schimadzu TQ LCMS-8040 system equipped with a triple quadrupole mass spectrometer. The HRMS spectra were obtained on a Micromass LCT Premier XE mass spectrometer.

2.2.4. Elemental Analysis

While the aforementioned analytical techniques can provide us with important structural information about the synthesized molecules, they provide limited information about purity. In order to ascertain the purity of the samples, elemental analysis is the method of choice. In a

typical experiment a known amount of sample is weighed out and combusted in the presence of excess oxygen gas in order to insure complete combustion. Then the gas that is evolved is analyzed for its H_2O, CO_2, and N_2 contents. These values can then be converted into elemental percentages of C, H, and N in the bulk material. If the experimental and theoretical percentages agree within ± 0.5 % then the sample is deemed pure. All reported elemental analyses were performed by Midwest Microlab in Indianapolis, Indiana on an Exeter analytical CHN analyzer.

2.2.5. X-ray Crystallography

X-ray crystallography is a technique that allows us to unambiguously determine the structure of the synthesized complex. Not only does it provide us with the connectivity within a certain molecule, it also provides us with the bond lengths and bond angles within the structural lattice of the crystal. Although X-ray quality crystals can be obtained by a wide variety of methods, in this thesis the crystals were obtained through either slow evaporation or vapor diffusion. Once X-ray quality crystals are obtained, a suitable crystal is chosen under a microscope and mounted on a mitogen loop. The loop is subsequently mounted on a Bruker X8 APEX-II Kappa geometry diffractometer equipped with a Mo radiation source and an Oxford Cryosystem low temperature device that operates at a temperature of 100 K. Then the sample is exposed to X-ray radiation which then interacts with the crystal lattice based on Bragg's law ($n\lambda = 2d\sin\theta$) where λ is the wavelength of the incident radiation (0.71073 Å in this case), d is the distance between the planes of the crystal lattice, and θ is the scattering angle. The diffraction patterns were collected in a charge coupled detector (CCD). The structure was solved by direct methods using the SHELXS-97[98] program which is part of APEX II and refined by least squares method on F^2, SHELXL-97,[98] which is incorporated in OLEX2.[99]

2.2.6. UV-visible Spectroscopy

UV-Visible spectroscopy can be used probe the electronic transitions of a given metal complex, and therefore it can be used to infer pivotal information about the oxidation states. The spectrum is typically presented as a plot of molar absorptivity (ε in L mol^{-1} cm^{-1}) *versus* wavelength (λ in nm). Molar absorptivity ε can be obtained using the Beer-Lambert law in which ε = A/(C*l), where A is the absorption, C is the concentration of the solution, and l is the length of the cell. Moreover, ε is directly correlated to the probability that a certain transition is allowed.[96] According to the selection rules, a transition can be either Laporte allowed/forbidden or spin-allowed/forbidden.[96] Metal complexes typically exhibit four distinct types of electronic transitions: intraligand charge transfer (ILCT), metal-to-ligand charge transfer (MLCT), ligand-to-metal charge transfer (LMCT), and d-d transitions. These transitions can be distinguished based on the intensity of their molar absorptivity. The ILCT bands (allowed by spin and Laporte selection rules) have an ε between 20,000 and 60,000; MLCT and LMCT processes have an ε between of 5,000 and 20,000; d-d transitions are low intensity transitions with an ε between 50 and 1,000. UV-visible spectra were recorded on a Shimadzu 3600 UV-VIS-NIR spectrophotometer.

2.2.7. Cyclic Voltammetry

Cyclic voltammetry (CV) can be used to probe the different redox states that can be accessed by a certain metal complex, as well as the energies required to reach those states.[100] A typical experiment was conducted using a BAS 50W potentiostat, with a standard three electrode cell setup in which a glassy carbon electrode is used as the working electrode, a platinum wire is used as the auxiliary electrode, and finally an Ag/AgCl electrode is used as the reference electrode. In a typical experiment, a solution of the complex in question and supporting electrolyte (such as tetrabutylammonium hexafluorophosphate, $TBAPF_6$) is prepared and the

voltammograms are measured. At the end of the experiment, ferrocene is added as an internal redox standard (E^0 = 400 mV *vs.* NHE) to standardize the measured potentials.[101]

The reversibility of a process is typically measured in one of two ways. The first way is by taking the absolute value of the ratio of the anodic current to that of the cathodic current ($|i_{pa}/i_{pc}|$). For an ideal reversible process the value of $|i_{pa}/i_{pc}|$ is equal to 1.[100] The other measure of reversibility is the peak separation of the anodic and cathodic processes; the ideal value of this separation for a reversible process is equal to 59 mV.[97] If a process is reversible, the potential is reported as $E_{1/2}$ which is equal to the average of the anodic and the cathodic potentials.[99] However, in the case of irreversible processes one must report the E_{pc} and E_{pa} values.

2.2.8. Spectroelectrochemistry

Spectroelectrochemistry is a technique that allows us to obtain the UV-Vis spectra of the oxidized and reduced species. The information *via* spectroelectrochemistry is vital in obtaining structural information about the changes that takes place upon oxidation or reduction of the complex. In a typical experiment, a U-shaped platinum wire is sandwiched between two indium tin oxide (ITO) plates that are subsequently placed inside a quartz cuvette. A Pt wire is used as an auxiliary electrode, and a silver wire is used as a pseudo reference electrode. Both electrodes are also placed inside the quartz cuvette. The complex is then dissolved in a suitable solvent and supporting electrolyte ($TBAPF_6$) is added to the solution. The solution is placed in the cuvette and the solution goes up between the two ITO plates *via* capillary action. The cuvette is placed inside a UV-Vis spectrophotometer and the electrodes are connected to a BAS 50W potentiostat. A suitable potential is applied, and the UV-Vis spectra are recorded.

2.2.9. Electron Paramagnetic Resonance Spectroscopy

While NMR can be used to determine the structure of diamagnetic species such as organic ligands and $^{LS}3d^6$ [Co^{III}] metal complexes, it cannot be used to determine the structure of paramagnetic species such as $3d^7$ [Co^{II}] and $3d^5$ [Co^{IV}]. In such cases Electron Paramagnetic Resonance Spectroscopy (EPR) spectroscopy needs to be utilized.[102] However, EPR spectra can only be obtained for species that possess an odd number of unpaired electrons (non-integer spin).[102] EPR spectroscopy allows us to determine the spin state of the metal complex (high spin *vs.* low spin) as well as the coordination environment around the metal center.

Electrons can exist in one of two spin states where the electron spin quantum number (m_s) is either +1/2 or -1/2. In the absence of a magnetic field, both of these states are isoenergetic. However, when a magnetic field is applied the different spin state split according to the Zeeman effect in which they are aligned either parallel or antiparallel to the magnetic field. The difference in energy (ΔE) between the two spin states can be obtained according to **equation 2.1.**, where $\mu_B$is the Bohn magneton, B_0 is the applied magnetic field, and finally g is known as the g factor.

$$\Delta E = g\mu_B B_0 \qquad \textbf{equation 2.1.}$$

In a typical experiment, the sample is frozen and placed inside a magnetic field. The temperature inside around the sample can vary from 4.2 K to room temperature. While exposed to a constant frequency of microwaves, the magnetic field is varied. This variation in the magnetic field changes ΔE between the two electronic states. When the obtained ΔE matches the energy of the incident microwave radiation a peak is observed in the spectrum. In order to make the signal more prominent, a typical spectrum is presented as the first derivative plot of the obtained signal versus the applied magnetic field.

Experiments conducted by Oleg Poluektov and Jens Niklas at Argonne National Laboratory were performed using a Bruker ELEXSYS E580 EPR spectrometer (Bruker Biospin, Rheinstetten, Germany), equipped with a Bruker ER 4102ST resonator or a Bruker ER 4122SHQ resonator. The temperature was controlled using a helium gas-flow cryostat (ICE Oxford, UK) and an ITC (Oxford Instruments, UK). Data processing was done using Xepr (Bruker BioSpin, Rheinstetten) and Matlab 7.11.2 (The MathWorks, Inc., Natick) environment. Experiments performed at Wayne State University were performed using a Bruker EMX X-band spectrometer equipped with an Oxford variable-temperature cryostat. Samples were placed in a 4 mm quartz tube and they were subsequently frozen in liquid nitrogen before being placed inside the spectrometer.

2.2.9. Bulk Electrolysis

Bulk electrolysis (also known as controlled potential electrolysis) is a method that is used to electrochemically isolate reduced or oxidized species. Coupled with UV-Visible-NIR and EPR spectroscopies we are able to gain important information regarding the electronic nature of the isolated species. A typical experiment is performed in a custom-built air-tight H-type cell shown in **Figure 2.1.** which consists of two compartments separated by a fine frit. The two compartments of the H-type cell are used to separate the working and the auxiliary electrodes. The oxidized/reduced species is isolated by using a vitreous carbon working electrode, an Ag/AgCl reference electrode, and a Pt coil auxiliary electrode in the presence of $TBAPF_6$ as a supporting electrolyte. The electrodes are then connected to a potentiostat and a suitable potential is applied in order to complete the conversion. The advantage of using bulk electrolysis over chemical reductants/oxidants is that the applied potential can be controlled and unwanted side reactions can be avoided. On the other hand, the large amount of supporting electrolyte that is

needed (typically 0.1 mol/L) limits our ability to isolate the complex (beyond spectroscopic characterization) and to grow x-ray crystals.

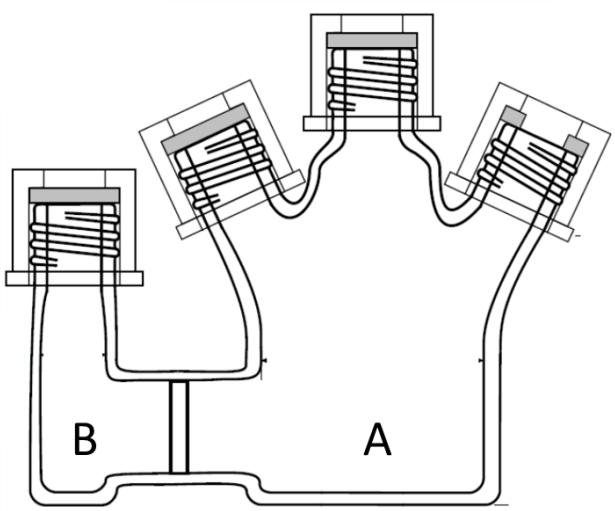

Figure 2.1. A schematic representation of the H-type cell that is used during bulk electrolysis. Compartment A is used to house the working and reference electrodes, while compartment B is used to house the auxiliary electrode.

2.2.10. Chemical Reduction Experiments

One way of avoiding the complications posed by the supporting electrolyte in bulk electrolysis is to use redox transfer agents.[15] The reducing agents that were chosen were cobaltocene ($E^{0'}$ = -1.33 $V_{Fc/Fc+}$)[15], decamethylcobaltocene ($E^{0'}$ = -1.94 $V_{Fc/Fc+}$)[15], and potassium intercalated in graphite[103] (KC_8, $E^{0'}$ = -3.64 $V_{Fc/Fc+}$). KC_8 is by far the strongest reducing agent that was employed, however one of the limitations of KC_8 is its ability to react with most polar solvents. Therefore, THF was primarily used as the solvent for KC_8 reduction reactions. As such the scope of metal complexes that could be studied with KC_8 was severely limited by the lack of solubility in THF. To overcome this limitation we resorted to aforementioned weaker reducing agents that are compatible with polar organic solvents such as MeCN.

2.2.11. Catalytic Studies

Two main methods are used to evaluate catalytic performance for water reduction and water oxidation. The first is cyclic voltammetry, which is used to determine if the synthesized species is catalytic and to derive the overpotential needed for catalysis. Following the initial determination of catalytic activity, bulk electrolysis is performed to determine the turnover number and catalytic stability. The following sections describe the catalytic methods used in this thesis for water reduction and oxidation.

2.2.11.1. Water Reduction Experiments

Cyclic voltammetry tests were performed using a three-electrode setup with a mercury pool working electrode, Pt-wire auxiliary electrode, and Ag/AgCl reference electrode (1 mol/L KCl). Phosphate buffer (1 mol/L, pH = 7) was used as the electrolyte during catalysis. If a shift in the catalytic wave is observed following the introduction of the metal complex (compared to the blank), the complex is catalytic. The overpotential is calculated by subtracting 0.617 V from the onset potential measured in V *vs.* Ag/AgCl (**equation 2.2.**).

$$\text{Overpotential } (\eta) = \text{onset potential } (V_{Ag/AgCl}) - 0.617 \text{ V} \qquad \textbf{equation 2.2.}$$

Turnover numbers were determined using a similar setup to that described in section **2.2.9.** but the vitreous carbon working electrode is replaced by a mercury pool working electrode. The mercury pool electrode consists of a pool of mercury at the bottom of the cell into which a platinum wire was dipped to provide electrical conductivity. A glass capillary tube sheathed the exposed portion of the Pt wire, protecting it from contact with the surrounding solution. Before the application of a potential the headspace was thoroughly purged with nitrogen gas. The amount of hydrogen gas produced was determined by using a Gow-Mac 400 gas chromatograph (GC) equipped with a thermal conductivity detector, and an 8 ft x 1/8 in., 5

Å molecular sieve column operating at a temperature of 100 °C. Nitrogen was used as a carrier gas at a flow rate of 30 ml/min. A calibration curve was obtained by purging a Schlenk flask with hydrogen gas, then known volumes of hydrogen were injected into the GC. The volumes were converted to number of moles using the ideal gas equation, and a plot of moles of hydrogen *versus* peak area was obtained. In a typical experiment, 100 µL of headspace were injected into the GC. This allowed the determination of the total amount of hydrogen in the headspace. The turnover number (TON) was determined by dividing the total number of moles of hydrogen produced (n_{H2}) by the number of moles of catalyst (n_{cat}) used (**equation 2.3.**). The Faradaic efficiency (%F) shown in **equation 2.4.** was determined by multiplying twice n_{H2} by the Faraday constant (F) and then dividing the product by charge consumed (Q).

$$TON = n_{H2}/n_{cat} \qquad \textbf{equation 2.3.}$$

$$\%F = (2.F.n_{H2}/Q).100 \qquad \textbf{equation 2.4.}$$

2.2.11.2 Water Oxidation Experiments

Unlike water reduction, which was done homogenously, the water oxidation catalysis described in this thesis is based on surface functionalization. As such, the methods used differ. The cyclic voltammograms were recorded using an EC Epsilon potentiostat equipped with an RDE2 rotating disc electrode. A three-electrode setup included an Ag/AgCl reference electrode, a Pt wire auxiliary electrode, and a glassy carbon working electrode (surface area = 0.07 cm^2). The catalyst was deposited on the glassy carbon surface of the working electrode and dried under an infrared heat lamp. The cyclic voltammograms were measured at a scan rate of 10 mV/S at 1600 rpm in a 1 M KOH solution. The use of a slow scan rate is critical for measuring the steady-state behavior at the electrode's surface, while the use of the RDE electrode is important for facilitating the removal the evolved gasses from the surface of the electrode, allowing for

more accurate determination of current density.[104] After measuring the potentials against Ag/AgCl, they were converted to the normal hydrogen electrode (NHE) using equation by adding 0.197 V. Additionally, using the iR compensation function of the Epsilon software, the resistivity of the solution was measured and corrections were calculated using **equation 2.5**.

$$E_{NHE} = E_{Ag/AgCl} + 0.197 - iR \qquad \textbf{equation 2.5.}$$

Bulk electrolysis was performed as previously described, with the only difference being that a piece of carbon cloth as the working electrode. The working electrode was prepared by depositing 100 uL of the functionalized ink onto a 1 cm x 4 cm piece of carbon cloth, allowing it to dry for 15 minutes, and threading it onto a copper wire. The TON was determined similarly to water reduction as in **equation 2.6.**, while the %F was determined using **equation 2.7**.

$$TON = n_{O2}/n_{cat} \qquad \textbf{equation 2.6.}$$

$$\%F = (4.F.n_{O2}/Q).100 \qquad \textbf{equation 2.7.}$$

A GOW-MAC series 400 gas chromatograph equipped with a TCD detector and an 8 ft x 1/8 in., 5 Å molecular sieve column held at 60 ˚C were used to quantify the amount of oxygen produced. Helium was used as the carrier gas and flowed at a rate of 30 mL/min. Atmospheric nitrogen was used as an internal standard.

CHAPTER 3. DEACTIVATION OF A COBALT CATALYST FOR WATER REDUCTION *VIA* VALENCE TAUTOMERISM

Reproduced with permission from Baydoun, H.; Mazumder, S.; Schlegel, H. B.; Verani, C.;

Chem. Eur. J. **2017**, *23*, 9266

3.1. Introduction

Substantial efforts have been directed towards the development of molecular catalysts for water reduction based on abundant and affordable 3*d* transition metals.[5, 7, 10-11, 14, 16, 27-28, 30, 105-108] Such catalysts must withstand drastic electronic and structural changes from high to low redox states required for hydride formation that precedes H_2 evolution. To this end, cobalt complexes have been extensively studied because of the energetically affordable stepwise conversions from $3d^6$ [Co^{III}] to $3d^8$ [Co^{I}] and back to [Co^{III}–H^-] and [Co^{II}–H^-] hydride species. [5, 7, 10-13, 37-38, 106] As such, mechanistic understanding of catalytic pathways —including those of deactivation— becomes a necessary condition to the development of robust catalysts.

Our group has studied the mechanisms of several proton and water reduction cobalt catalysts, including some phenolate-rich Co^{III} [N_2O_3] catalysts that served as the stepping stone to much improved pyridine-rich $Co^{II/III}$ [$N_2N^{py}_3$] catalysts for water reduction that display TON > 7000 mol^{-1}.[9-10] We have gathered evidence that some molecular catalysts such as cobalt oximes [12] are converted into nanoparticulates through ligand hydrolysis triggered by radical-based mechanisms.[11] Therefore, although the involvement of ligands in the catalytic cycle has been reported,[109-111] we conclude that radical formation may have deleterious effects on H_2 production.[45, 112-113] Here we examine this issue in detail and suggest that formation of energetically equivalent valence tautomers, *viz*. $[Co^{I}(L)]^- \leftrightarrow [Co^{II}(L\bullet)]^-$ offers additional conversion pathways that lead to catalyst deactivation.

3.2. Experimental

3.2.1. Synthetic procedures

Synthesis of N,N'-(1,2-phenylene)dipicolinamide (L^1). The ligand L^1 was synthesized by adapting a literature reported procedure.[114] Briefly, 7.8 g of o-phenelenediamine (72.2 mmol) were reacted with 18 g of picolinic acid (14.6 mmol) and 39 mL of triphenyl phosphite (46 g, 14.8 mmol) in pyridine as solvent. The reaction mixture was heated under reflux overnight and then the pyridine was concentrated and the ligand was crashed with ether. The precipitate was filtered and washed with isopropanol and ether then it was dried under vacuum to yield the pure ligand. ^{1}H NMR, ppm ($CDCl_3$, 400 MHZ): δ 10.27 (s, 2H), δ 8.57 (d, 2H), δ 8.33 (d, 2H), δ 7.90 (m, 4H), δ 7.46 (m, 2H), δ 7.31 (m, 2H).

Synthesis of $[Co^{III}L^1(pyr)_2]PF_6$ (1). A MeOH solution of 1.6 g of $Co(OAc)_2.4H_2O$ (6.2 mmol) was added dropwise to a MeOH solution containing 2.0 g of H_2L^1 (6.2 mmol) To this mixture an excess of 10 mL of pyrrolidine was added. The solution was allowed to stir overnight at room temperature. Then oxygen was bubbled into the solution for 5 minutes. The reaction mixture was filtered and an excess of 1.5 g of NH_4PF_6 (9.2 mmol) were added to precipitate **1**. X-ray quality crystals were grown *via* diethylether vapor diffusion into an acetonitrile solution of **1**. Yield: 86%. ESI (m/z^+) = 517 for $[Co^{III}L^1(pyrrolidine)_2]^+$. IR (KBr, cm^{-1}) 3167 (ν_{N-H}), 1626 ($\nu_{C=O}$), 1599 and 1572 ($\nu_{C=N}$, and $\nu_{C=C}$), 844 (ν_{PF6}). ^{1}H NMR, ppm (CD_3CN, 400 MHZ): δ 9.45 (d, 2H), δ 8.90 (m, 2H), δ 8.41 (t, 2H), δ 8.29 (d, 2H), δ 8.00 (t, 2H), δ 7.12 (m, 2H), δ 3.22 (2H), 2.11 (4H), δ 1.53 (4H), δ 1.29 (8H). Anal. Calc. for $C_{26}H_{30}CoN_6O_2PF_6$: 47.14; H: 4.56; N: 12.69; Found: C: 47.05; H: 4.44; N: 12.49.

Synthesis of $[Co^{II}L^1(pyr)]^o$ (2). $[Co^{II}L^1(pyr)]^o$ (2). was isolated using standard glovebox techniques. A sample of **1** (108 mg, 0.16 mmol) was dissolved in THF and added into a vial containing of KC_8 (22 mg; 0.16 mmol). The solution immediately changed from green to red and

was allowed to stir for 2h. The sample was filtered and a solution was obtained that yielded crude **2**. X-ray quality crystals were obtained by recrystallization in acetonitrile. Anal. Calc. for $C_{22}H_{21}CoN_5O_2$: 59.20; H: 4.74; N: 15.69; Found: C: 57.27; H: 4.45; N: 14.50.

Synthesis of [Co^{I}L^{1}]K. (3). [Co^{I}L^{1}]K was isolated in a similar way as for **2** using 44 mg of KC_8 (2 equiv. ; 0.32 mmol). The solution changed color from green to dark blue. X-ray quality crystals of **3** were obtained after filtration via slow evaporation from the THF solution. ^{1}H NMR, ppm (CD_3CN, 600 MHZ, Figure S5): δ 9.36 (2H), δ 8.37 (2H), δ 8.26 (t, 2H), δ 6.72 (2H), δ 6.53 (2H), δ 6.46 (2H).

3.2.2. Water Reduction Experiments

Cyclic voltammetry tests were performed using a 3-electrode setup with a mercury pool working electrode, Pt-wire auxiliary electrode, and an Ag/AgCl reference electrode (1 mol/L KCl). 1 mol/L phosphate buffer was prepared by dissolving NaH_2PO_4 (0.227 mol) and Na_2HPO_4 (0.273 mol) in 500 mL of ultrapure water. After complete dissolution, the pH was adjusted to 7.00 by adding appropriate amounts of NaOH and monitoring the solution pH of the solution using an Orion 5 star pH meter. Turnover numbers were determined using a custom-built H-type bulk electrolysis setup. The cell consisted of two airtight compartments separated by a fine frit. One compartment was used to house the auxiliary electrode (Pt coil) while the other compartment was used to house the reference electrode (Ag/AgCl) and the working electrode (mercury pool). The mercury pool electrode consisted of a pool of mercury at the bottom of the cell into which a platinum wire was dipped so as to provide electrical conductivity, the exposed part of the platinum wire was protected from being in contact with the solution by surrounding it with a glass capillary. Before the application of a potential the headspace was thoroughly purged with nitrogen gas. The amount of hydrogen gas produced was determined by using a Gow-Mac

400 gas chromatograph (GC) equipped with a thermal conductivity detector, and a 8 ft x 1/8 in., 5 Å molecular sieve column operating at a temperature of 100 °C. Nitrogen was used as a carrier gas at a flow rate of 30 ml.min^{-1}. A calibration curve was obtained by purging a Schlenk flask with hydrogen gas, then known volumes of hydrogen were injected into the GC. The volumes were converted to number of moles using the ideal gas equation, and a plot of moles of hydrogen versus peak area was obtained. In a typical experiment 100 µL of headspace were injected into the GC this allowed the determination of the total amount of hydrogen in the headspace. The turnover number was determined by dividing the total number of moles of hydrogen produced by the number of moles of catalyst used. While the faradaic efficiency was determined by dividing the actual number of moles of hydrogen produced by the number of moles of hydrogen that should have been produced based on the charge consumed.

3.2.3. Computational Methods

Electronic structure calculations were carried out using the B3LYP* functional[115] as implemented in a development version of Gaussian.[116] The SDD basis set and effective core potential[117] were used for the Co atom and the 6-31G(d,p) basis set[118-119] was used for the other atoms. Solvation effects in acetonitrile and water were incorporated using the implicit SMD solvation model[120] and were included during structure optimization. All of the optimized structures were confirmed as minima by harmonic vibrational frequency calculations and the converged wave functions were tested for the SCF stability. The zero-point energy and thermal corrections were included for the calculation of the free energies. The standard states of 1 M concentration were considered for all the reactants and products for calculating the free energies of reactions. The literature value of –270.3 kcal/mol is used for the free energy of proton in water.[121] The spin density plots (isovalue = 0.004 au) were visualized using GaussView.[122]

Vertical electronic excitation energies and intensities were evaluated using time-dependent DFT (TD-DFT)[123-125] and the orbital transitions of each excited state were characterized using the natural transition orbital (NTO) method.[126]

3.2.4. X-ray Structural Determination:

Data were collected on a Bruker APEX-II Kappa geometry diffractometer with Mo radiation and a graphite monochromator using a Bruker CCD (charge coupled device) based diffractometer equipped with an Oxford Cryostream low-temperature apparatus. All crystals were mounted on a mitogen loop using paratone oil and frozen at 100 K. The structures were solved by the direct method using the SHELXS-97 program which is part of APEX II[127] and refined by least squares method on F^2, SHELXL-97[98], which is incorporated in OLEX2.[99] Hydrogen atoms were placed in calculated positions. For **1** a dark green block-shaped crystal of dimensions 0.2 x 0.4 x 0.9 mm was obtained vapor diffusion from diethylether into an acetonitrile solution. Omega and phi scans of 0.5° per frame for 20 s were used during collection. The crystal was solved to a resolution of 0.72 Å with a completeness of 100%. The structure was solved in the space group P-1. The asymmetric unit consists of a molecule of **1**, an acetonitrile and a hexaflourophosphate counter ion. For **2** a green needle-shaped crystal of dimensions 0.01 x 0.1 x 0.4 mm was obtained *via* slow evaporation from an acetonitrile solution. Omega and phi scans of 0.5° per frame for 50 s were used during collection. The crystal was solved to a resolution of 0.84 Å with a completeness of 100%. The structure was solved in the space group $P2_1/n$. The

asymmetric unit consists of a discrete molecule of **2**. For **3** a dark blue plate-shaped crystal of dimensions 0.01 x 0.3 x 0.9 mm was obtained *via* slow evaporation from a THF solution. Omega and phi scans of 0.5° per frame for 30 s were used during collection. The crystal was solved to a resolution of 0.85 Å with a completeness of 98%. The structure was solved in the space group P-1. The asymmetric unit consists of two molecules of **3** three THF solvent molecules, and two potassium counter ions.

	$[Co^{III}L^{1}(pyr)_2]PF_6$	$[Co^{II}L^{1}(pyr)]$	$[Co^{I}L^{1}]K$
Empirical formula	$C_{28}H_{33}CoF_6N_7O_2P$	$C_{22}H_{21}CoN_5O_2$	$C_{48}H_{48}Co_2K_2N_8O_7$
Formula weight	703.51	446.37	1045.00
Temperature (K)	100.1	100.1	100.1
Wavelength (Å)	0.7107	0.7107	0.7107
Crystal system, space group	Triclinic, P-1	Monoclinic, P21/C	Triclinic, P-1
a (Å)	9.6672(4)	12.8083(10)	11.4058(15)
b (Å)	11.7496(6)	10.1395(8)	12.2282(16)
c (Å)	13.0206(6)	14.7503(12)	16.747(2)
α (º)	86.633(2)	90	89.903(6)
1β (º)	85.105(2)	91.819(3)	75.105(6)
γ (º)	85.265(2)	90	83.263(6)
Volume ($Å^3$)	1466.54(12)	1897.8(3)	2240.7(5)
Z	2	4	2
Calculated density (Mg/m^3)	1.593	1.562	1.549
Absorption coefficient (mm^{-1})	0.719	0.936	0.990
F (000)	724.0	924.0	1080.0
R(F) (%)	4.63	3.97	6.05
R_w(F) (%)	7.63	5.79	15.72
CCDC number	CCDC 1533010	CCDC 1533009	CCDC 1533008

Table 3.1. Crystal structure data for $[Co^{III}L\text{-}pyr_2]PF_6$, $Co^{II}L$-pyr, and $[Co^{I}L]K$. $R(F) = \sum \| F_o | - | F_c \| / \sum | F_o |$; $Rw(F) = [\sum w(F_o^2 - F_c^2)^2 / \sum w(F_o^2)^2]^{1/2}$ for $I > 2\sigma(I)$

3.3. Results and discussion

In order to evaluate this hypothesis, we examined the electronic and redox structure of the pseudo-octahedral $[Co^{III}L^{1}(pyr)_2]PF_6$ (**1**) complex, where $(L^{1})^{2-}$ is the doubly deprotonated form of a bis-amido pyridine ligand and pyr denotes axially coordinated pyrrolidines. Complex **1** was synthesized by adapting reported procedures,[114, 128-129] where the ligand was treated under aerobic conditions with **1** equiv. of $Co(OAc)_2 \cdot 4H_2O$ in presence of pyrrolidine using methanol as the solvent. The formation of a microcrystalline precipitate was induced by the addition of NH_4PF_6. Complex **1** was thoroughly characterized using ^{1}H–NMR, FTIR, ESI-MS(+), and elemental analysis (See Experimental Section for details), as well as X-ray crystallography (*vide infra*). As it will be discussed, this species is capable of robust water reduction followed by rapid deactivation.

The cyclic voltammogram (CV) of **1** was taken in CH_3CN and shows five independent redox processes **(Figure 3.1.**). The processes at $E_{1/2}$ = 1.34 V_{NHE} (ΔE = 0.10 V, $|I_{pa}/I_{pc}|$ = 1.08) and E_{pa} = 1.94 V_{NHE} are assigned as amido to amidyl radical oxidations[130-131] (for potentials *vs.* Ag/AgCl and Fc^{+}/Fc see **Table 3.2.**).[101] The process at E_{pc} = -0.32 V_{NHE} is assigned to the Co^{III}/Co^{II} couple.[129, 132] The process at -1.08 V_{NHE} (ΔE_p = 0.16 V, $|I_{pa}/I_{pc}|$ = 0.84) is tentatively assigned to a Co^{II}/Co^{I} couple, while the third process at -1.79 V_{NHE} (ΔE = 0.11 V) is attributed to a pyridine-based reduction.

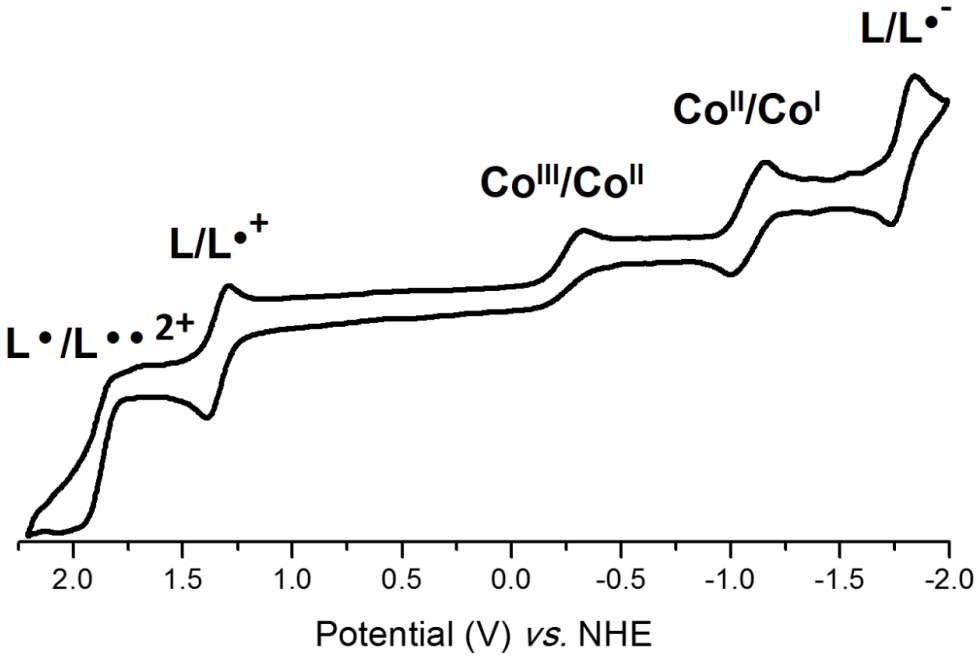

Figure 3.1. The CV of **1** (1 mM) in MeCN. Glassy carbon, Ag/AgCl, Pt wire, $TBAPF_6$ (0.1 M). Ferrocene is used as an internal standard.

	V_{NHE}	$V_{Fc/Fc+}$	$V_{Ag/AgCl}$
$L^{\bullet+}/L^{\bullet\bullet 2+}$	1.94	1.30	1.73
$L/L^{\bullet+}$	1.34	0.70	1.13
Co^{III}/Co^{II}	-0.32	-0.96	-0.53
Co^{II}/Co^{I}	-1.08	-1.72	-1.23
$L/L^{\bullet-}$	-1.79	-2.34	-1.91

Table 3.2. The voltages for the processes obtained in **Figure 3.1.** reported versus NHE, ferrocene, and Ag/AgCl. The experimental value of ferrocene was 0.43 V *vs.* Ag/AgCl.

The CV of **1** in phosphate buffer (1 mol/L, pH 7, **Figure 3.2.**) shows a catalytic wave at -0.95 V_{NHE} in presence of **1** with concurrent evolution of gas at the surface of the electrode. This corresponds to an overpotential of 0.54 V. Moreover, the onset potential of -0.95 V_{NHE} closely resembles that of the Co^{II}/Co^{I} couple observed at $E_{1/2}$ = -1.08 V_{NHE} obtained in acetonitrile. This observation confirms that the active species in catalysis is the [Co^{I}] complex in accordance with

the accepted mechanisms for proton reduction using cobalt complexes; catalysis is initiated by the reaction of [Co^{I}] with a proton to form a [Co^{III}–H^{-}] hydride intermediate.[5, 7, 10-13, 37-38, 106] The identity of the evolved gas was determined as H_2 by means of gas chromatography following a bulk electrolysis experiment that was performed in an air-tight H-type cell.

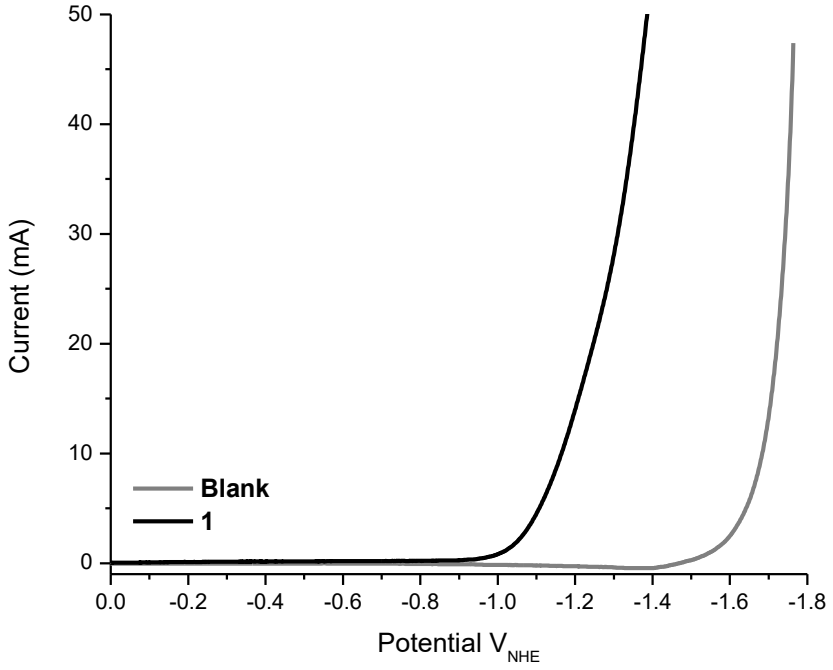

Figure 3.2. Polarization curve for **1** in phosphate buffer (1 mol/L, pH 7).

The catalyst showed significant initial activity yielding a TON of 675 ± 30 after 30 min of electrolysis (TOF = 23 min^{-1}) with Faradaic efficiency of 97 ± 3%. However, this high activity persisted only for a short period of time. After *ca.* 30 minutes of catalysis, considerable decrease in charge consumption was observed (**Figure 3.3.**). The observed TON is only a lower limit of the maximum value as it was measured following significant deacivation. Similar catalytic behavior has been observed for certain polypyridine frameworks.[133-134] Moreover, the solution changes color from green to colorless (**Figure 3.4.**). Compared to the UV-visible spectrum of the solution prior to catalysis, the post-catalytic spectrum shows the disappearance of charge transfer (CT) processes at *ca.* 413 nm associated with an N_{amido} → Co^{III} ligand-to-metal CT. However,

the peaks associated with intraligand CT and observed below 300 nm persist (**Figure 3.5.**). This suggests that the complex is undergoing demetallation. These observations prompted us to investigate the mechanism by which catalyst degradation takes place with the aim of providing guiding principles for future catalyst design.

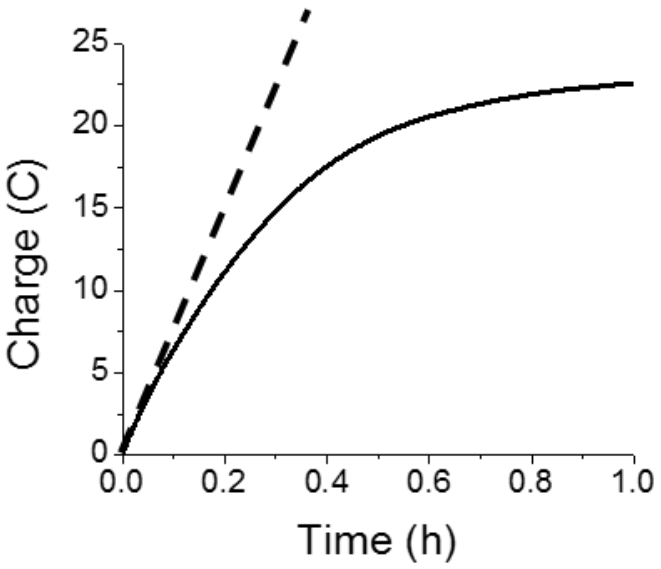

Figure 3.3. Charge consumption over time for **1** (8 µmol/L) at -1.16 V_{NHE}. The dotted line represents an idealized charge consumption. Electrodes: Hg-pool (w), Pt (aux), Ag/AgCl.

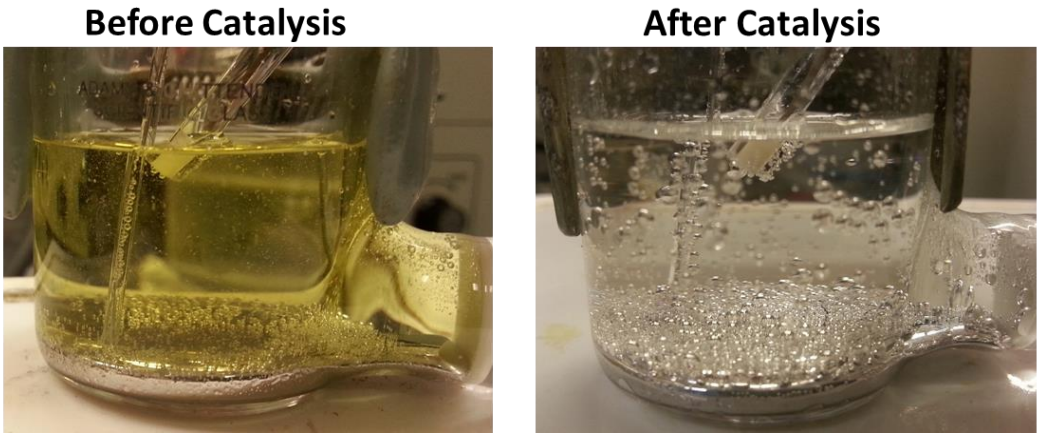

Figure 3.4. The initial color of the solution (green), and the color of the solution at the end of the catalytic run (colorless).

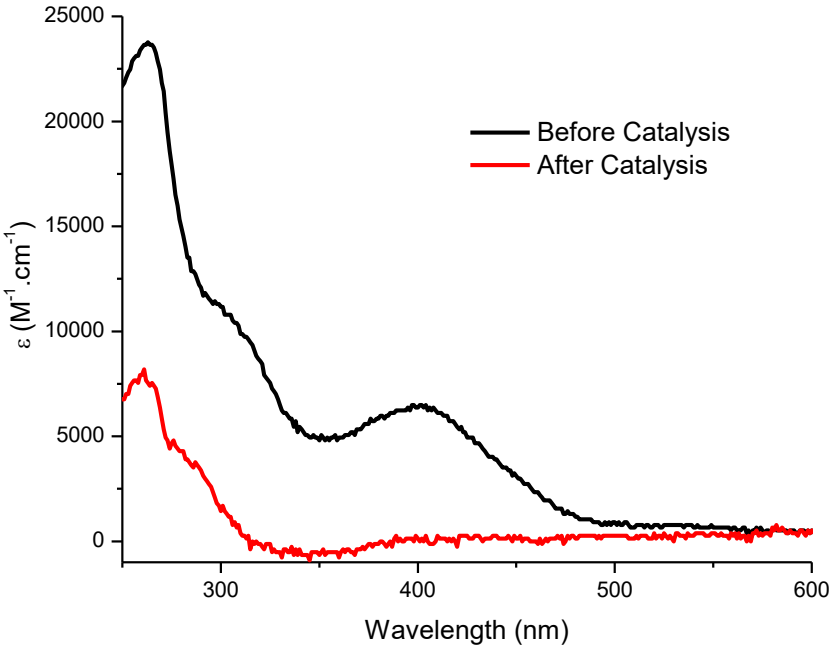

Figure 3.5. The UV-Vis spectrum before and after catalysis (same conditions as **Figure 3.3.**).

Because the active form of the catalyst must contain [Co^{I}], the elucidation of the deactivation pathways requires the investigation of the structural and electronic properties of the complex in distinct reduced oxidation states. To this end we used experimental observations along with DFT calculations. The structural information was obtained using potassium graphite (KC_8) as a stoichiometric reducing agent in order to isolate chemically the [Co^{II}] and [Co^{I}] reduced forms of our catalyst. Starting from **1** we were able to isolate the singly reduced [Co^{II}]

analogue $[Co^{II}L^{1}(pyr)]^{o}$ (**2**) and the doubly reduced $[Co^{I}]$ analogue $[Co^{I}L^{1}]K$ (**3**). We were able to grow X-ray quality crystals for **1**, **2**, and **3** (**Figures 3.6., 3.7., and 3.8. respectively**). The structure of the $[Co^{III}]$ species **1** (**Figure 3.6.**) shows the expected pseudo-octahedral geometry, with the ligand $(L)^{-2}$ occupying the equatorial plane and the two pyrrolidines binding to the axial positions. Excellent agreement was observed between the obtained bond lengths and angles and that of structurally related complexes with a trivalent cobalt ion.[128-129]

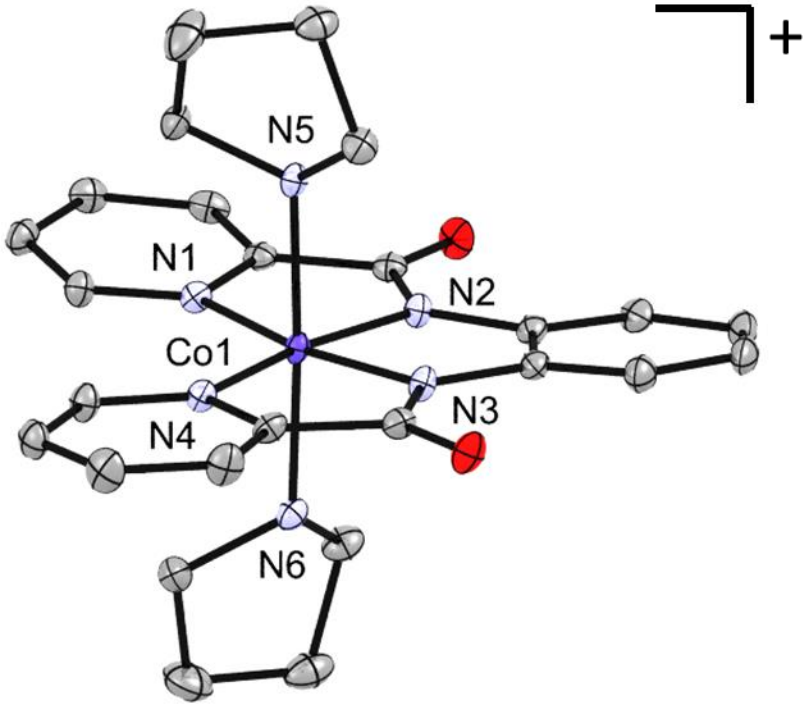

Figure 3.6. Crystal structures of **1** (CCDC 1533010). Hydrogen atoms, solvents, and counter ions removed for clarity. Ellipsoids shown at 50% probability. Selected bond lengths: Co1-N1 1.9861(18), Co1-N4 1.9998(17), Co1-N2 1.8887(18), Co1-N3 1.8887(18), Co1-N5 2.0154(18), Co1-N6 2.0047(18).

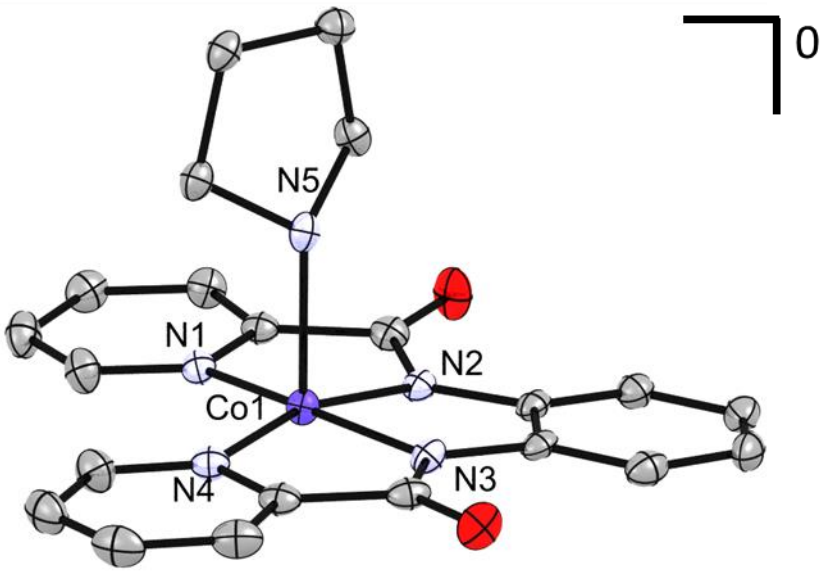

Figure 3.7. Crystal structures of **2** (CCDC 1533009). Hydrogen atoms, solvents, and counter ions removed for clarity. Ellipsoids shown at 50% probability. Selected bond lengths: Co1-N1 1.971(2), Co1-N4 1.993(2), Co1-N2 1.882(2), Co1-N3 1.882(2), Co1-N5 2.139(2).

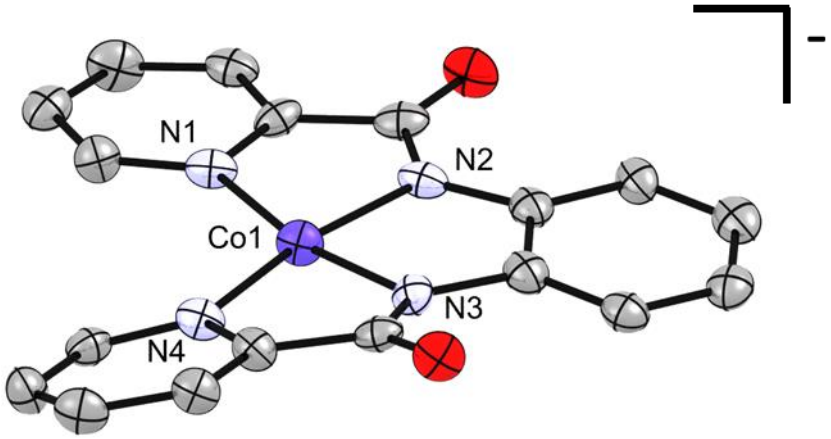

Figure 3.8. Crystal structures of **3** (CCDC 1533008). Hydrogen atoms, solvents, and counter ions removed for clarity. Ellipsoids shown at 50% probability. Selected bond lengths: Co1-N1 1.889(4), Co1-N4 1.892(4), Co1-N2 1.874(4), Co1-N3 1.865(4).

The structure of the [Co^{II}] species **2** shown in **Figure 3.7.**, on the other hand, displays a square pyramidal geometry in which τ = 0.018.[135] This decrease from six- to five-dentate coordination upon reduction from [Co^{III}] to [Co^{II}] agrees with similar results from our group observed in oxime environments.[12] Similarly, it is interesting to note that when compared to **1**, minor changes occur in the Co-L bond lengths, while a considerable 0.135 Å elongation takes place along the Co-N5 bond. The maintenance of the bond lengths within the equatorial plane

suggests that upon metal-centered reduction from [Co^{III}] to [Co^{II}] the incoming electron is transferred to the unoccupied d_{z2} orbital, while the electrons in the d_{xy}, d_{xz}, and d_{yz} orbitals remain largely unaffected, as previously proposed by our group.[12] The d_{x2-y2} orbital remains unoccupied. Moreover, the EPR spectrum of **2** (**Figure 3.9.**) shows a signal with a g value of 2.018 which is consistent with the presence of one unpaired electron. Hence, the [Co^{II}] ion is found in a doublet $^{LS}3d^7$ configuration. This proposition was further examined by DFT calculations that showed excellent agreement between the crystal structure of **2** and the optimized structure of a doublet $^{LS}3d^7$ [Co^{II}] ion (**Figure 3.10.**).

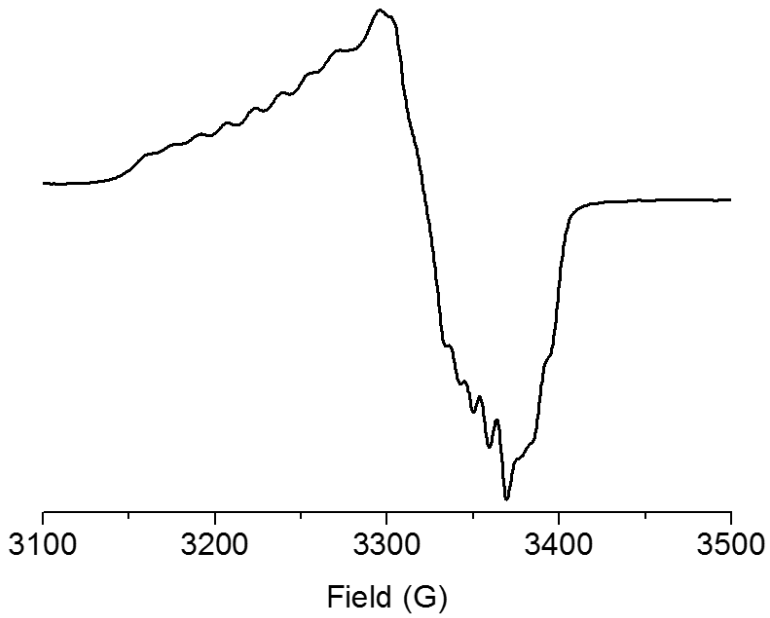

Figure 3.9. EPR spectrum of **2** taken at 110 K in MeCN.

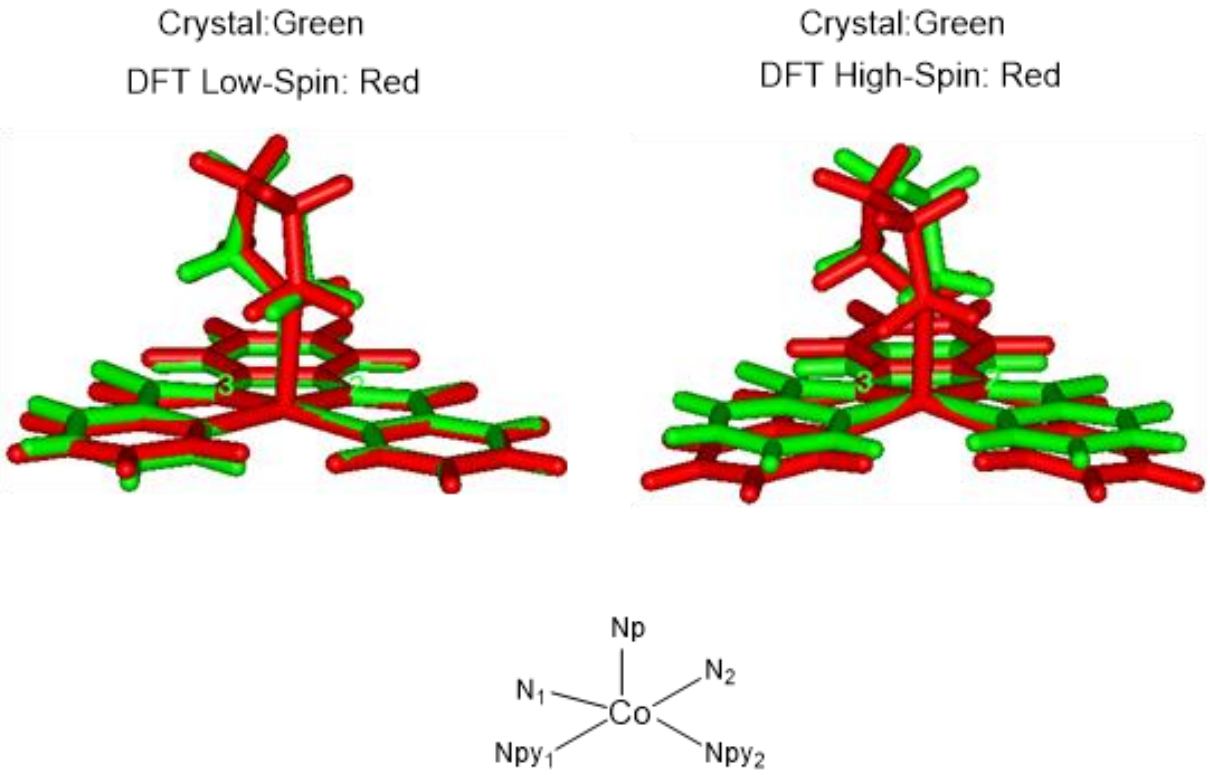

	Crystal	DFT:LS	DFT:HS
Co–Np	2.138	2.236	2.158
Co–N1	1.882	1.907	2.067
Co–N2	1.882	1.910	2.077
Co–Npy1	1.971	2.025	2.147
Co–Npy2	1.993	2.033	2.143

Figure 3.10. Overlay of the crystal structure with DFT-calculated high-spin (HS) and low-spin (LS) structures for [Co^{II}–(L^1)(pyr)] and comparison of the Co–N bond lengths (Å) between the crystal and calculated structures.

The structure of **3** (**Figure 3.8.**). warrants some detailed discussion; unlike its 5-coordinate [Co^{I}] oxime congener,[12] this doubly reduced derivative of **1** is composed of a

tetracoordinate cobalt complex in a distorted square planar geometry, where the maximal distortion between any two opposing planes among the Co-N bonds deviates by 9.5° from the idealized 0° (An idealized square planar structure displays 0° between opposing angles, whereas an idealized tetrahedral structure displays those planes at 90°).[136] Compared to the previous two structures, the Co-N_{amide} bond lengths remain unchanged while its Co-$N_{pyridine}$ bond lengths are elongated by *ca.* 0.1 Å. Moreover, other bond lengths on the ligand framework remain largely unchanged (**Figure 3.11.**). This observation implies that occupation of the d_{z2} orbital is favored in the solid state, and that the structure contains a *bona fide* $3d^8$ [Co^I] ion. Interestingly, DFT results indicate that two lowest lying isoenergetic states are possible for the nominal "Co^I species": (i) a metal-centered singlet species $[^{3d8}Co^IL^1]^-$ akin to the crystal structure, or (ii) a ligand-reduced and radical-containing triplet $[^{3d7}Co^{II}(L^{1\bullet})]^-$ species with the unpaired electron centered on the amido-pyridine moiety. These two states display a calculated energy difference of *ca.* 3 kcal/mol, thus within the limits of the method (**Figure 3.12.**). Furthermore, both the $3d^8$ $[Co^IL^1]^-$ and the coupled $(3d^7 - ½)$ $[Co^{II}(L^{1\bullet})]^-$ species yield spin integers that are NMR active (**Figure 3.13.**). However, comparison of the Co-N bond lengths, including those in the ligand framework, show better agreement with the metal-centered $[Co^IL^1]^-$ than with the ligand-reduced $[Co^{II}(L^{1\bullet})]^-$ species (**Figures 3.14.-3.16.**).

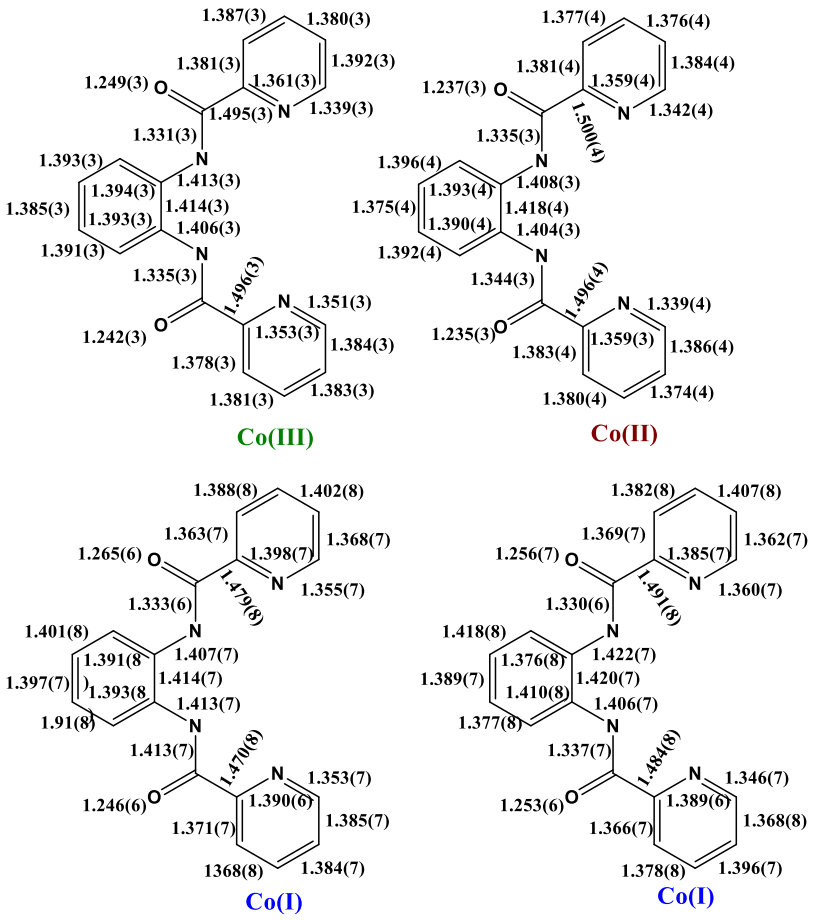

Figure 3.11. Bond lengths on the ligand backbone of complexes **1**, **2**, and **3.**

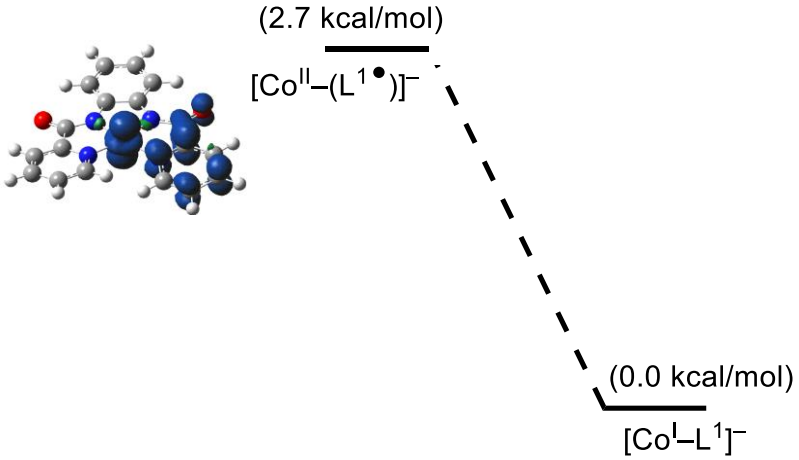

Figure 3.12. Free energy difference between $[Co^{I}\text{-}L^{1}]^{-}$ and $[Co^{II}\text{-}(L^{1\bullet})]^{-}$ and the spin density (isovalue = 0.004 au) plot of $[Co^{II}\text{-}(L^{1\bullet})]^{-}$.

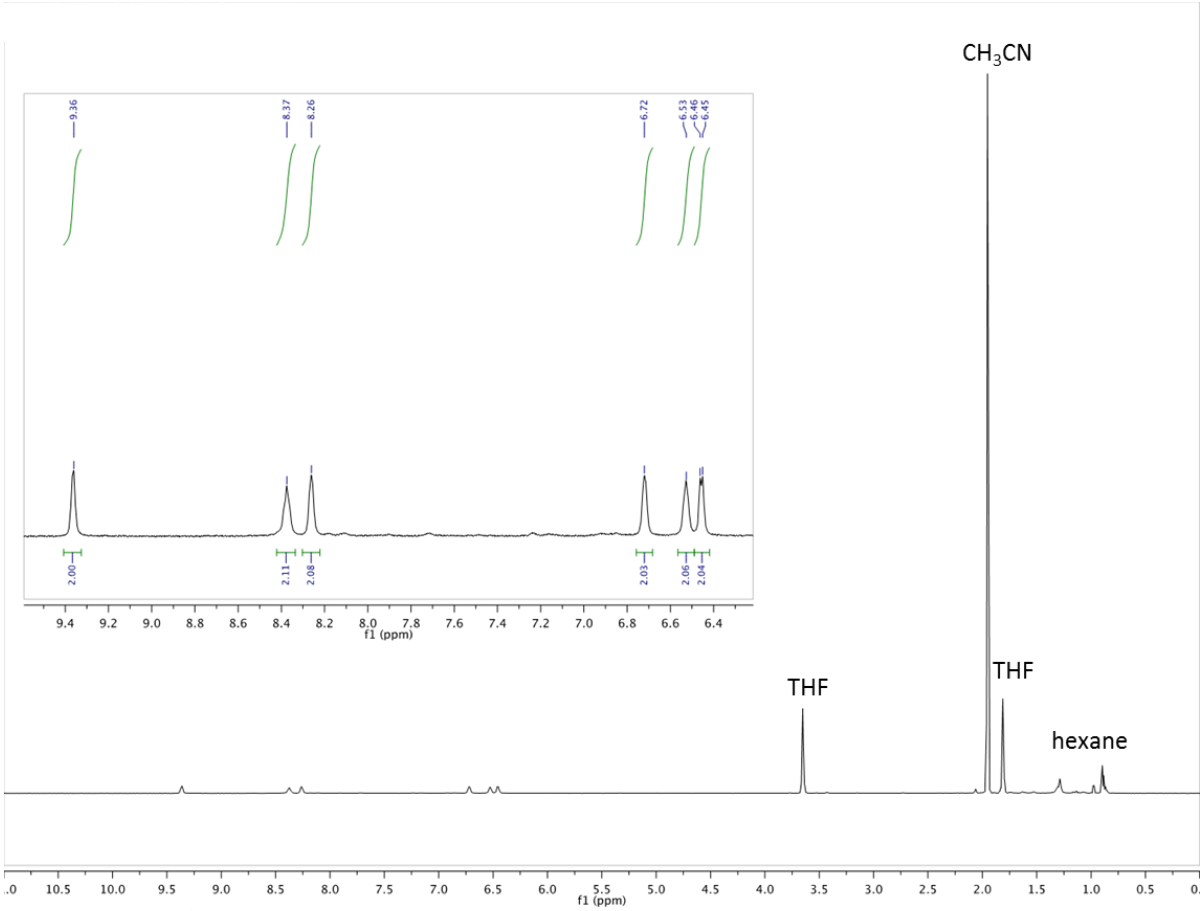

Figure 3.13. ^{1}H NMR spectrum of **3** in CD_3CN. Inset: zoomed in view of the aromatic region. Conditions: 600 MHz, CD_3CN was dried over molecular sieves and subsequently reacted with metallic sodium to remove impurities that can react with [Co^{I}]. The solvent was filtered before use.

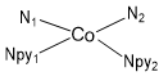

	Crystal Structure 1	Crystal Structure 2	DFT $[Co^{II}–(L^{1\bullet})]^{-}$	DFT $[Co^{I}–(L^{1})]^{-}$
Co–N1	1.864	1.869	1.887	1.887
Co–N2	1.878	1.875	1.900	1.889
Co–Npy1	1.887	1.895	1.961	1.940
Co–Npy2	1.885	1.894	2.000	1.938

Figure 3.14. Comparison of the Co–N bond lengths (Å) between the crystal structures and the DFT-calculated $[Co^{I}\text{-}L^{1}]^{-}$ and $[Co^{II}\text{-}(L^{1\bullet})]^{-}$ geometries.

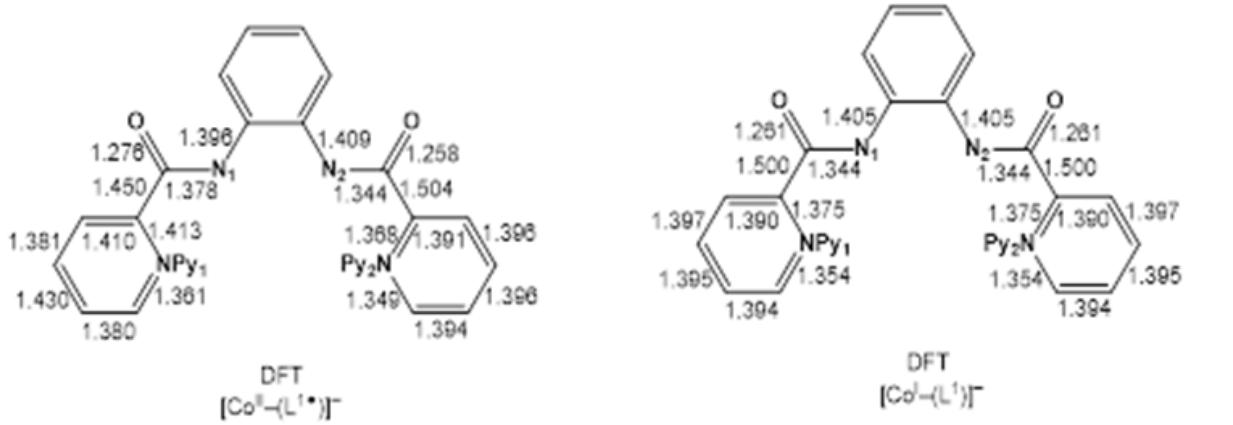

Figure 3.15. DFT-calculated bond lengths (Å) on the ligand framework of $[Co^{I}\text{-}L^{1}]^{-}$ and $[Co^{II}\text{-}(L^{1\bullet})]^{-}$.

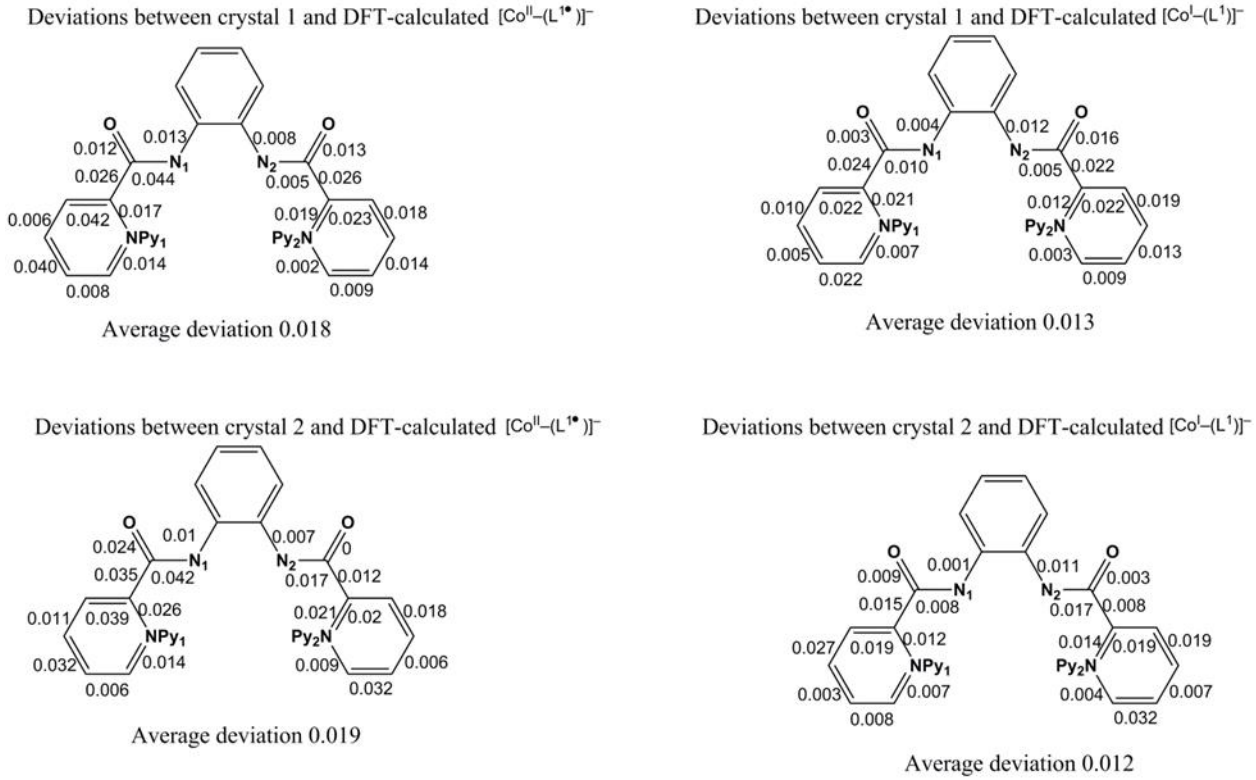

Figure 3.16. Comparison of the bond lengths on the ligand framework between the crystal structures (**Figure 3.11**) and DFT-calculated structures (**Figure 3.15**). Differences are reported in Å.

Pivotal information necessary to probe the electronic nature of the reduced species comes from the UV-Visible-NIR spectra of **1**, **2**, and **3 (Figure 3.17.).** As previously discussed, the spectrum of **1** shows a strong LMCT absorption at 413 nm. The spectrum of **2**, on the other hand, is characterized by an absorption at 336 nm with a shoulder at 452 nm assigned to a $Co^{II} \rightarrow$

$N_{amidopyridine}$ MLCT transition that confirms metal reduction. However, the spectrum of **3** also shows strong absorptions in the NIR region at 1028 and 1160 nm unquestionably attributed to ligand-stabilized radicals.[53, 137-140] Complex **3** was independently generated *via* electrochemical reduction, and a spectrum with identical features was obtained (**Figure 3.18.**) indicating that the same species can be conveniently obtained chemically or electrochemically. Therefore, analysis of these results suggest that in the solid state the $[Co^{I}L^{1}]K$ species prevails for **3**, while in an acetonitrile solution the species described as $[Co^{II}(L^{1\bullet})]K$ is accesible. This conclusion receives further support from time-dependent-DFT calculations shown in **Figures 3.19.** and **3.20.** where the simulated UV-Visible-NIR spectrum of $[Co^{I}L^{1}]^{-}$ lacks significant absorption processes above 800 nm, while the simulated spectrum for $[Co^{II}(L^{1\bullet})]^{-}$ shows absorption peaks at 1023 and 1205 nm of the NIR region. These transitions are mainly due to intraligand π-π* charge transfers centered on the amidopyridine moiety shown in **Figures 3.21.**

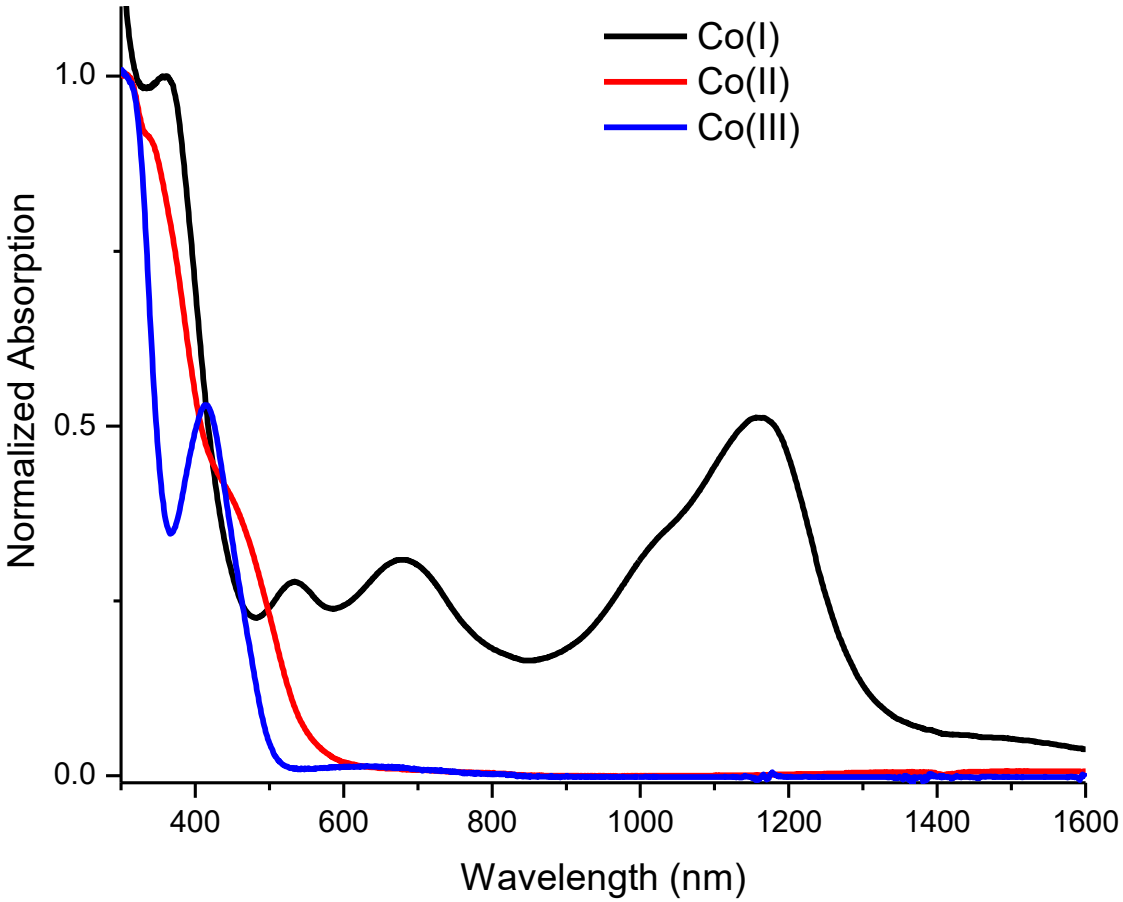

Figure 3.17. Normalized UV-Visible-NIR spectra of **1, 2,** and **3** in MeCN.

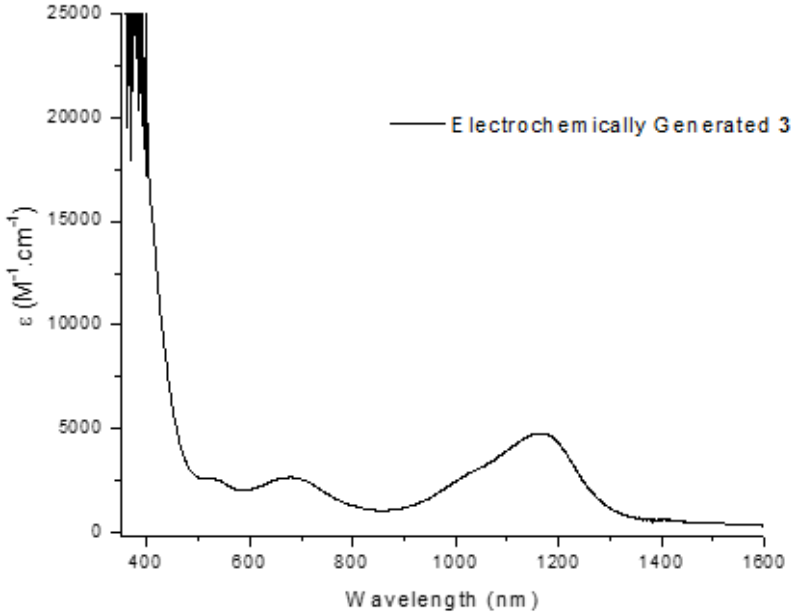

Figure 3.18. The UV-Vis-NIR spectrum for the electrochemically generated **3**.

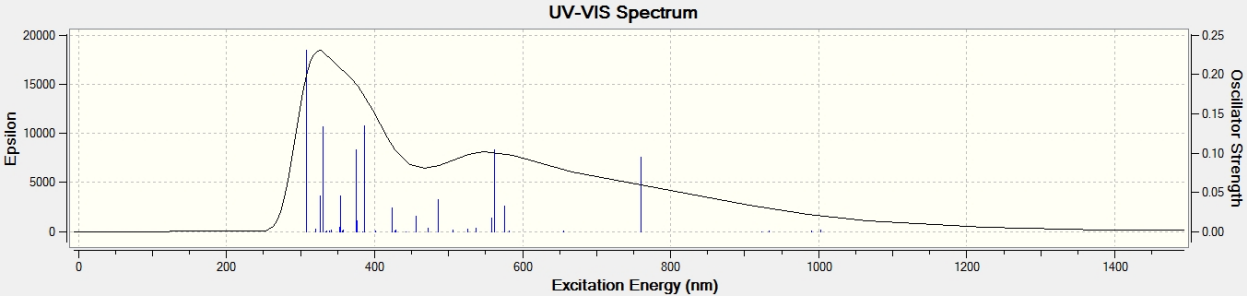

Figure 3.19. TD-DFT calculated UV-Vis spectrum for $[Co^{I}L^{1}]^{-}$ in acetonitrile solvent.

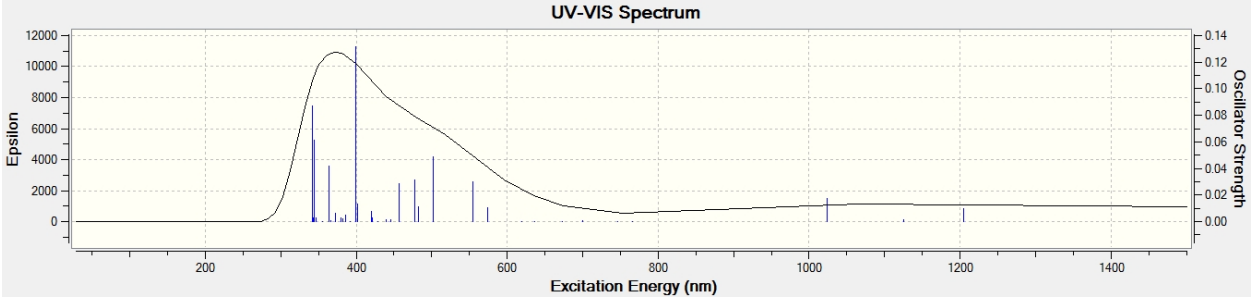

Figure 3.20. TD-DFT calculated UV-Vis spectrum for $[Co^{II}(L^{1\bullet})]^{-}$ in acetonitrile solvent.

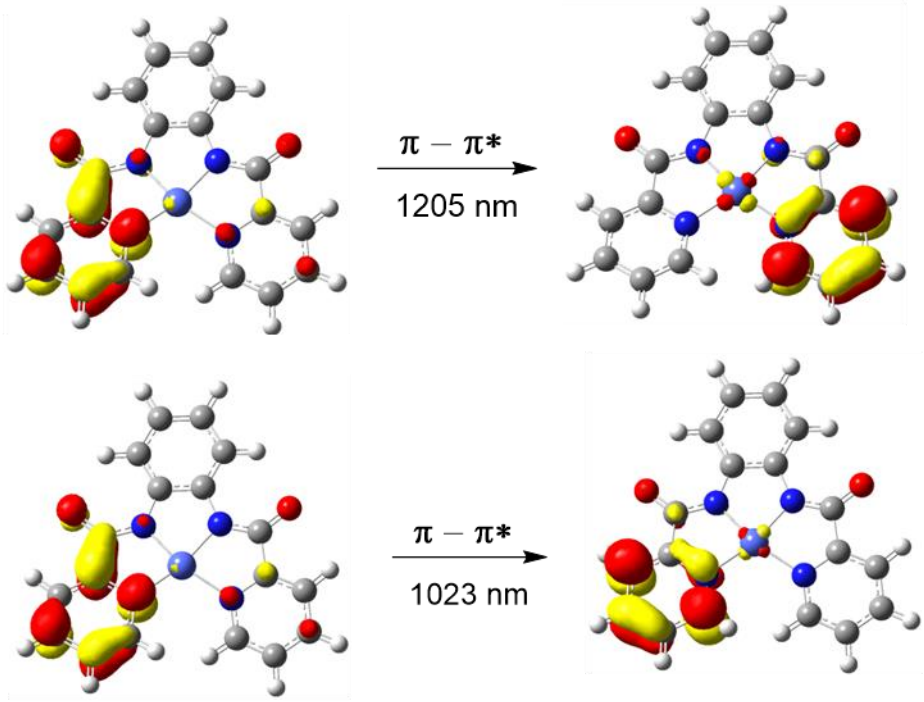

Figure 3.21. Calculated natural transition orbitals (NTOs at isovalue = 0.05 au) showing π-π* ILCT transition at 1023, and 1205 nm for $[Co^{II}\text{-}(L^{1\bullet})]^{-}$ in acetonitirle solvent.

The small calculated energy difference of 2.7 kcal/mol between the two species is well within the limit of the DFT method, and coupled with the detection of $[Co^{I}L^{1}]K$ in the solid state and $[Co^{II}(L^{1\bullet})]K$ in acetonitrile, suggests that there is an equilibrium between the two states.

Ergo, it is conceivable that both species will coexist under catalytic aqueous conditions. Such an equilibrium is consistent with the formation of valence tautomers.[141-143] As such, we propose that the difference in reactivity of the two tautomers with protons can be used to explain the deactivation of the catalyst. In presence of protons, the $[Co^{I}L^{1}]^{-}$ tautomer significantly favors the formation of a $[Co^{III}–H^{-}]$ species (-22 kcal/mol), which is the first step in the catalytic cycle for H_2 production (**Figure 3.22.** pathway *a* and **Figure 3.23.**). Conversely, concomitant formation of the $[Co^{II}(L^{1\bullet})]^{-}$ tautomer favors ligand protonation (**Figure 3.22.** pathways *b*-*d*). Upon such protonation of the ligand framework the structure deviates significantly from planarity (pathways *b* and *c*) with pathway *b* leading to a tridentate metal complex and from there to demetalation. These observations lead us to conclude that $[Co^{I}L^{1}]K$ is active in catalysis and leads to the formation of H_2, while $[Co^{II}(L^{1\bullet})]K$ is protonated, and eventually leads to the deactivation of the catalyst. This observation prompted us to hypothesize that running catalysis at a lower pH would favor protonation of the ligand and lead to deactivation. Indeed, catalytic runs at pH $\leq$ 6 led to a faster decay in the consumption of charge over time associated with an overall decrease in activity (**Figure 3.24.**).

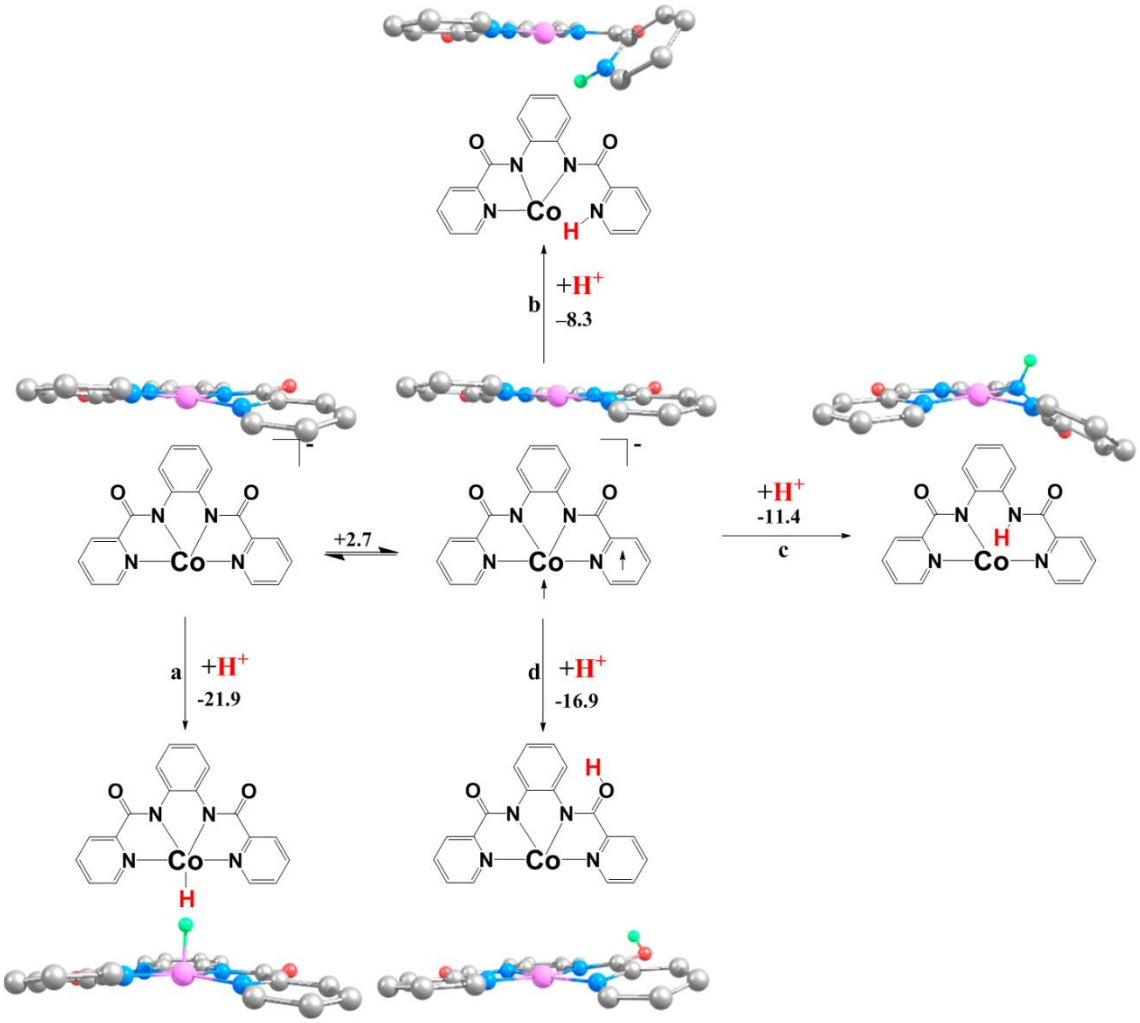

Figure 3.22. Energetics of protonation of the $[Co^{I}L^{1}]^{-}$ and $[Co^{II}(L^{1\bullet})]^{-}$ at different sites in water solvent. Free energies are reported in kcal/mol.

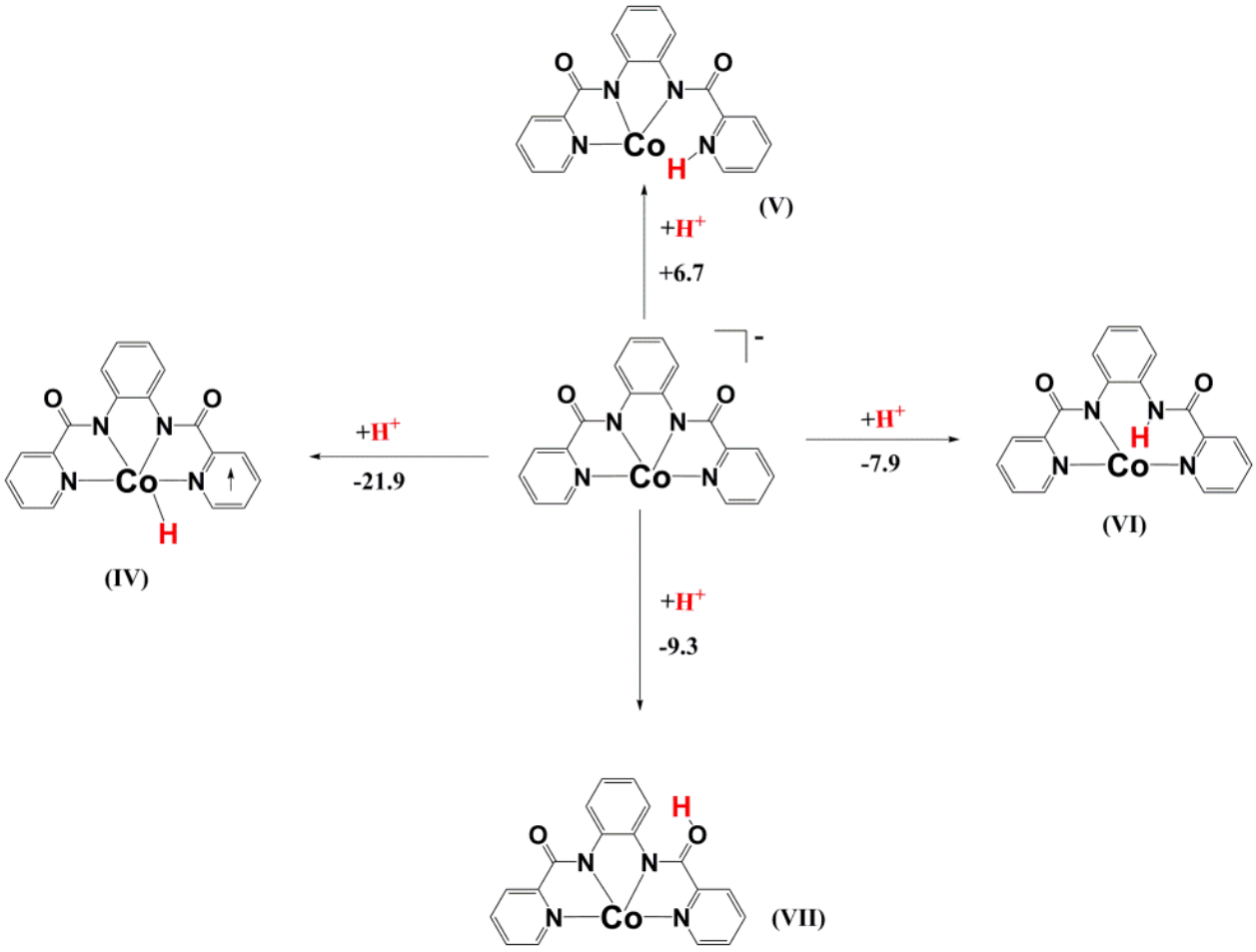

Figure 3.23. Free energies (in kcal/mol) of protonation of [Co^{I}–L^{1}] at different sites in water solvent.

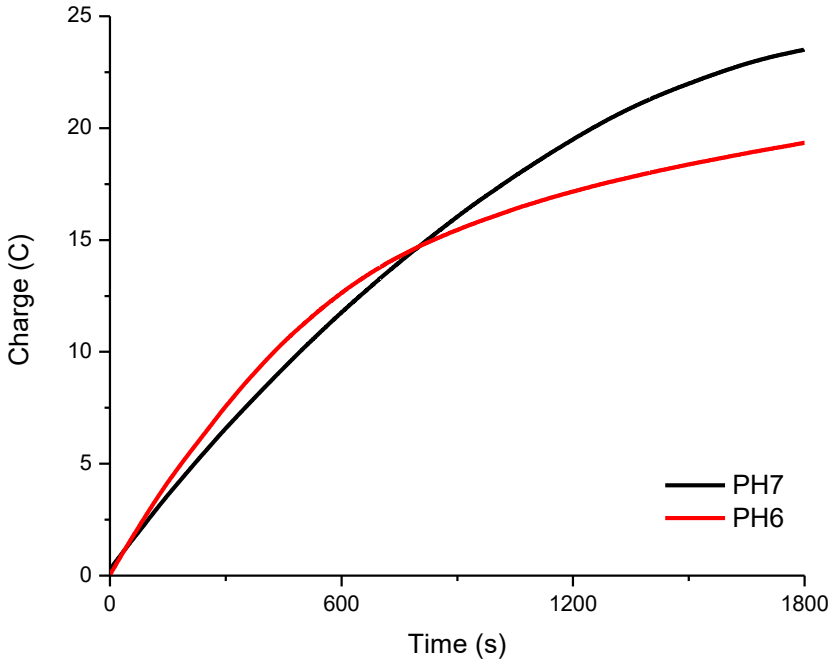

Figure 3.24. Charge consumption over time for **1** (8 µmol/L) at -1.16 V_{NHE} using pH = 7 buffer (black) and pH=6 buffer (red).

3.4. Conclusions

In summary, this work reports on a novel cobalt complex capable of performing water reduction at an overpotential of 0.54 V with TOF of 23 min^{-1} following 30 min of electrolysis with Faradaic efficiency of *ca.* 97 %. This initial catalytic activity decreases significantly after 30 minutes, and structural and electronic evaluation revealed that valence tautomerization is possible. The "[Co^{I}] state" can afford either $[Co^{I}L^{1}]^{-}$ or $[Co^{II}(L^{1\bullet})]^{-}$ within less than 3 kcal/mol. While the $[Co^{I}L^{1}]^{-}$ species supports the formation of a catalytically active $[Co^{III}–H^{-}]$ species required for H_2 formation, the tautomer $[Co^{II}(L^{1\bullet})]^{-}$ favors ligand protonation accompanied by significant structural distortion that ultimately leads to catalyst deactivation associated with demetallation. These results allow us to postulate that efficient catalytic water reduction based on square planar ligands must proceed exclusively by means of the metal center while carefully

avoiding ligand protonation. Future work in our will build on these results for the design of systems where the $[Co^{I}L^{1}]^{-}$ tautomer is energetically separated from its $[Co^{II}(L^{1\bullet})]^{-}$ tautomer.

CHAPTER 4. ENHANCED CATALYTIC ACTIVITY AND ACTIVITY IN A BIMETALLIC COBALT CATALYSTS FOR WATER REDUCTION

4.1. Introduction

The use of bimetallic complexes has been proposed as a means of enhancing the catalytic activity of proton reduction catalysts.[16, 61-64, 144] To this end Gray and coworkers[63-64] have explored using different bridging moieties between the active sites of the catalysts. They concluded that using dicobaloximes that are covalently linked *via* an alkyl chain leads to no apparent enhancement in the rate of hydrogen production.[63] Later on, and using the much shorter BO_4^- bridge, they observed that the overpotential needed for proton reduction increased compared to the monometallic catalyst.[64] Moreover, Fukuzumi[16] and coworkers have shown that even when using bis(pyridyl)-pyrazolato and terpyridine ligands, which lead to a metal complex with the cobalt centers in close proximity to each other, the heterolytic mechanism is preferred and the hemolytic cleavage of two the $[Co^{III}\text{-}H^-]$ species is not observed. Verani *et. al.*[66] have recently shown that using a bimetallic catalyst based on a fused $[NN'_2O_2]$ ligand leads to cooperativity between the two metal centers in which during catalysis a $[Co^ICo^I]$ active species is formed. At this point one of the metal centers acted as a reaction center, while the other center acted as an electron reservoir. This leads to the concerted formation of a $[Co^{II}Co^{II}\text{-}H^-]$ species.

In this work, we compare the catalytic behavior of the monometallic and bimetallic cobalt-based amidopyridine catalysts (**1**, and **2** respectively) (**Figure 4.1.**). We have recently shown that **1** undergoes deactivation *via* the valence tautomerism of the Co^I active species ($[Co^I(L)] \leftrightarrow [Co^{II}(L^{\bullet})]$) in which $[Co^I(L^1)]$ leads to the formation of the catalytically relevant $[Co^{III}\text{-}H^-]$ while $[Co^{II}(L^{\bullet})]$ leads to the protonation of the ligand which is followed by the deactivation of catalyst.[60] In this chapter, we show that by using the bimetallic framework, we can lower the overpotential, enhance the turnover frequencies (TOFs), and stabilize the activity

of **2** compared to **1**. To the best of our knowledge this is one of the first examples of a bimetallic catalyst that is demonstrably more efficient than its monometallic counterpart.

Figure 4.1.: The metal complexes $[Co^{III}L^{1}(pyrr)_2]PF_6$ (**1**) and $[(Co^{III})_2L^{2}(pyrr)_4](PF6)_2$ (**2**) discussed in this work.

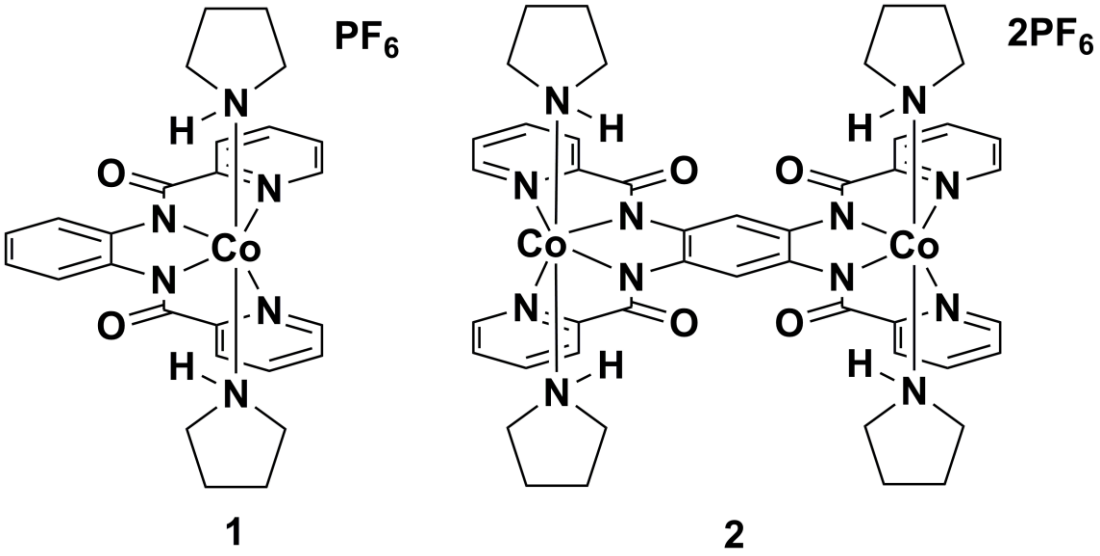

4.2. Experimental

4.2.1. Synthetic procedures

Synthesis of the ligand N,N'-(1,2-phenylene)dipicolinamide (H_2L^1). The synthesis of this ligand has been described in **Section 3.2.1.**

Synthesis of the ligand N,N',N'',N'''-(benzene-1,2,4,5-tetrayl)tetrapicolinamide (H_4L^2). The ligand L^2 was synthesized by adapting a literature reported procedure.[131] Briefly, 0.55 g of 1,2,4,5-benzenetetramine tetrahydrochloride (1.94 mmol) were reacted with 1.0 g of picolinic acid (8.13 mmol) and 2.5 g of triphenyl phosphite (8.06 mmol) in pyridine as solvent. The reaction mixture was heated under reflux overnight and the ligand formed as a precipitate. The precipitate was filtered and washed with methanol, isopropanol, and ether then it was dried under vacuum to yield the ligand. Due to the insolubility of the H_4L^2 in regular organic solvents, it was used without further characterization.

Synthesis of $[Co^{III}L^{1}(pyrr)_2]PF_6$ (1). The synthesis of this metal complex has been described in **Section 3.2.1.**

Synthesis of $[(Co^{III})_2L^{2}(pyrr)_4](PF_6)_2$ (2). $[(Co^{III})_2L^{2}(pyrr)_4](PF6)_2$ was synthesized by mixing a suspension of H_4L^2 (1.25 mmols, 0.7 g) in methanol with two equivalents of cobalt acetate tetrahydrate (2.5 mmol, 0.62 g) in the presence of excess pyrrolidine (2 mL) and stirring overnight. Then the solution was purged with oxygen for 15 minutes to ensure the complete oxidation of all the cobalt centers into the Co^{III} state. Finally, precipitation was induced by adding excess NH_4PF_6 (~4 equivalents, 0.8 g). The precipitate was washed with diethyl ether and dried under vacuum. Yield: 82%. IR (KBr, cm^{-1}) 1627 (s, C=O); 1597 (s, C=N), 833 (s, PF_6^-). ^{1}H-NMR [400MHz, CD_3CN, 300K] δ/ppm = 1.30 [br s, 16H (pyrrolidine CH_2-CH_2)]; 1.58 [m, 8H pyrrolidine CH_2)]; 2.19 [m, 8H pyrrolidine CH_2)]; 3.21 [br s, 4H pyrrolidine (NH)]; 7.98 [t, 4H (aryl)]; 8.31 [d, 4H (aryl)]; 8.41 [t, 4H (aryl)]; 9.45 [d, 4H (aryl)]; 10.38 [s, 2H (aryl)]; ESI pos. in MeOH: m/z = 478 for $[2]^{2+}$. Anal. for $[(Co^{III})_2L^{2}(pyrr)_4](PF6)_2$: $C_{46}H_{54}Cl_2Co_2N_{12}O_{12}$: Calcd: 44.31; H: 4.37; N: 13.48; Found: C: 44.46; H: 4.27; N: 13.22. X-ray quality crystals were obtained as the ClO_4 salt.

Synthesis of $[(Co^{III})_2L^{2}(pyrr)_4](ClO_4)_2$. This species was synthesized for the purpose of obtaining the crystal structure. $[(Co^{III})_2L^{2}(pyrr)_4](ClO_4)_2$ was synthesized similarly to $[(Co^{III})_2L^{2}(pyrr)_4](PF6)_2$ but using $NaClO_4$ instead of NH_4PF_6. IR (KBr, cm^{-1}) 3268 (m, N-H), 1628 (s, C=O); 1595 (s, C=N), 1090 (m, $ClO4^-$). Anal. for $[(Co^{III})_2L^{2}(pyrr)_4](ClO_4)_2.3H_2O$: $C_{46}H_{54}Cl_2Co_2N_{12}O_{12}$: Calcd: 45.67; H: 5.00; N: 13.89; Found: C: 45.56; H: 4.71; N: 13.61. X-ray quality crystals were obtained from vapor diffusion of diethyl ether into acetonitrile.

Synthesis of $[(Co^{II})_2L^{2}(pyrr)_2]^0$ (3). $[(Co^{II})_2L^{2}(pyrr)_2]^0$ was obtained by reacting **2** (100 mg, 0.08 mmol) with two equivalents of cobaltocene (30 mg, 0.16 mmol) in acetonitrile under a

nitrogen atmosphere inside a labmaser 130 glovebox. The mixture was stirred for two hours and filtered. After letting the solution stand for several weeks, X-ray quality crystals grew.

4.2.2. Catalytic measurements. The same procedures used for catalysis described in **Chapter 3** were used in this chapter.

4.2.3. X-ray Structure Determination. Crystals were mounted on a mitogen loop using paratone oil. Data were collected on a Bruker APEX-II Kappa geometry diffractometer with Mo radiation and a graphite monochromator using a Bruker CCD (charge coupled device) based diffractometer equipped with an Oxford Cryostream low-temperature apparatus. The data was measured at a temperature of 100 K with omega and phi scans of 0.5° per frame. 30 s frames were used for **2** and 50 s frames were used for **3**. The structure was solved by the direct method using the SHELXS-97 program which is part of APEX II[145] and refined by least squares method on F^2, SHELXL-97,[98] which is incorporated in OLEX2.[99]

For **2**, a brown plate-shaped crystal of dimensions 0.05 x 0.05 x 0.1 mm was used, and the structure was solved to a resolution of 0.83 Å with a completeness of 98%. The structure was solved in the space group P-1. The asymmetric unit consists of half a molecule of **2**, an acetonitrile and a perchlorate counter ion. Hydrogen atoms were placed in calculated positions.

For **3**, a brown plate-shaped crystal of dimensions 0.03 x 0.07 x 0.1 mm was used, and the structure was solved to a resolution of 0.78 Å with a completeness of 100%. The structure was solved in the space group $P2_1/n$. The asymmetric unit consists of half a molecule of **3**. Hydrogen atoms were placed in calculated positions.

	$[(Co^{III})_2L^2(pyrr)_4](ClO_4)_2$	$[(Co^{II})_2L^2(pyrr)_2]$
Empirical formula	$C_{25}H_{30}ClCoN_7O_6$	$C_{19}H_{18}CoN_5O_2$
Formula weight	618.94	407.31
Temperature (K)	100.1	100.1
Wavelength (Å)	0.7107	0.7107
Crystal system, space group	Triclinic, P-1	Monoclinic, $P2_1/n$
a (Å)	8.9568(5)	7.6419(7)
b (Å)	9.0812(5)	15.2159(13)
c (Å)	15.7505(8)	14.3145(12)
α (°)	95.108(2)	90
1β (°)	90.949(2)	94.536(5)
γ (°)	93.501(2)	90
Volume (Å^3)	1273.34(12)	1659.3(3)
Z	2	4
Calculated density (Mg/m^3)	1.614	1.631
Absorption coefficient (mm^{-1})	0.837	1.061
F (000)	642.0	840.0
R(F) (%)	3.93	5.28
R_w(F) (%)	8.43	9.04

Table 4.1. Crystal structure data for **$[(Co^{III})_2L^2(pyrr)_4](ClO_4)_2$**, and **$[(Co^{II})_2L^2(pyrr)_2]$**. $R(F) = \sum \| F_o | - | F_c \| / \sum | F_o |$; $Rw(F) = [\sum w(F_o^2 - F_c^2)^2 / \sum w(F_o^2)^2]^{1/2}$ for $I > 2\sigma(I)$.

4.3. Results and discussion

4.3.1. Synthesis and characterization

The ligands H_2L^1 and H_4L^2 as well as complex **1** were synthesized according to reported procedures.[60, 114, 131] Complex **2** was synthesized by reacting two equivalents of cobalt acetate with one equivalent of H_4L^2. Precipitation was induced by the addition of NH_4PF_6 to yield a microcrystalline product that was thoroughly characterized using ^{1}HNMR, MS, FTIR, and elemental analysis. The sharp peaks in the ^{1}HNMR spectrum (**Figure 4.2.**) coupled with the observation of the signature PF_6 band at 833 cm^{-1} in the FTIR spectrum reaffirm that the expected formation of a [Co^{III}] in a $^{LS}3d^6$ environment took place. Moreover, the mass spectrum revealed five distinct peaks at m/z = 478.1, 442.6, 407.1, 371.5, and 336.0 that are consistent with the sequential loss of the axial pyrrolidines to form $[(Co^{III})_2L^2(pyrr)_4]^{2+}$, $[(Co^{III})_2L^2(pyrr)_3]^{2+}$, $[(Co^{III})_2L^2(pyrr)_2]^{2+}$, $[(Co^{III})_2L^2(pyrr)]^{2+}$, and $[(Co^{III})_2L^2]^{2+}$ respectively (**Figure 4.3.**). Finally, we were able to grow a crystal structure that reaffirms our structural assignments for $[(Co^{III})_2L^2(pyrr)_4](ClO_4)_2$, the perchlorate counterpart of **2** (*vide infra*). This complex was obtained as **2** but using $NaClO_4$ instead of NH_4PF_6.

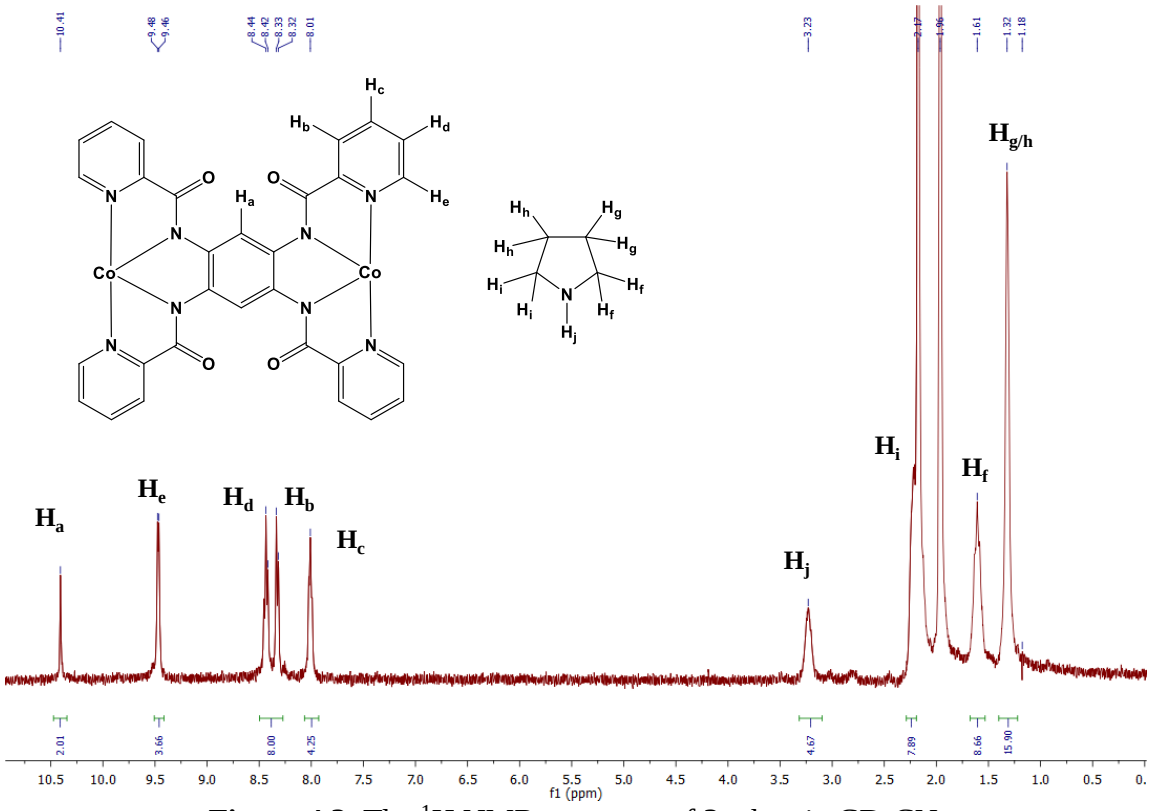

Figure 4.2. The ^{1}H NMR spectrum of **2** taken in CD_3CN.

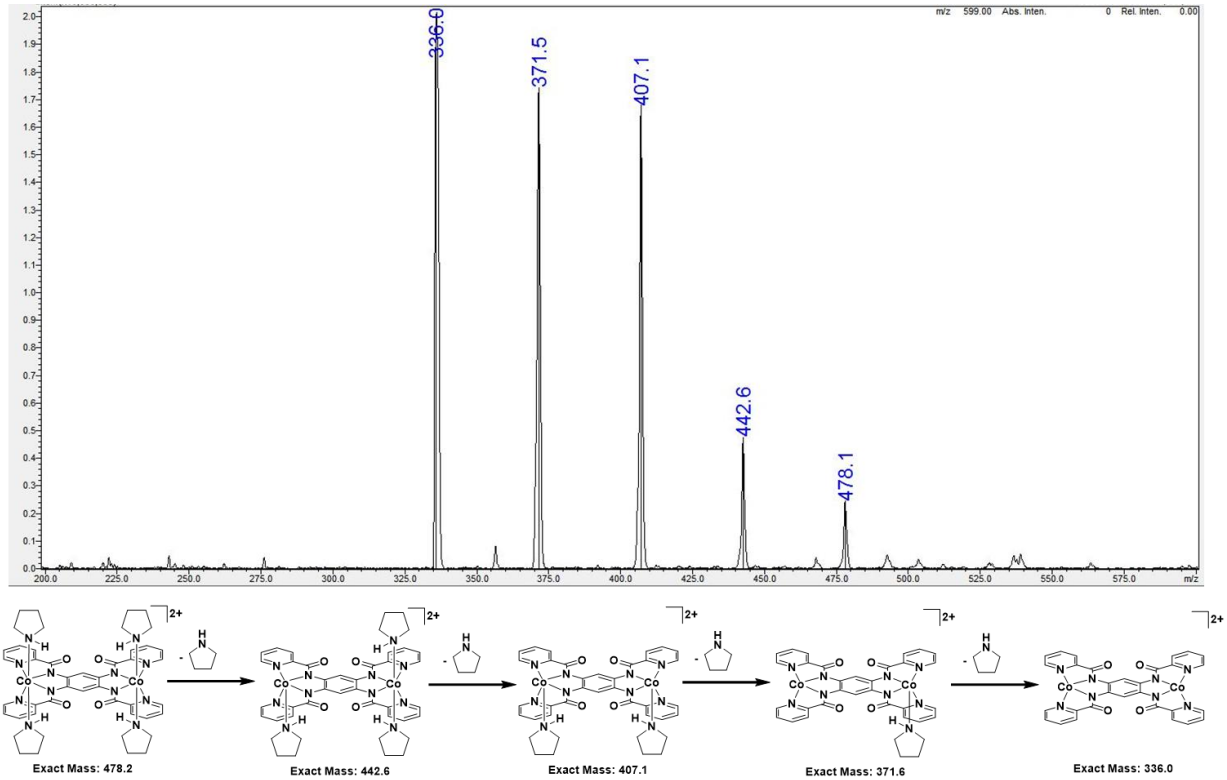

Figure 4.3. The mass spectrum of **2** obtained in CH_3CN in ESI(+) mode, as well as the observed fragmentation pattern.

In order to compare the catalytic activity of **1** and **2**, polarization curves were obtained in phosphate buffer (1 mol/L, pH = 7) and are shown in **Figure 4.4.** While **1** had an onset overpotential of 0.55 V, **2** shows a catalytic peak at an onset overpotential of 0.45 V. This corresponds to a 0.1 V improvement in the overpotential. Based on these observations, we were able to separate the catalytic activity into three voltage ranges (as denoted by the letters in **Figure 4.4.**). In the first voltage range, (region A) V < -0.95 V_{NHE} **1** and **2** are catalytically active. In the second voltage range (region B) where -0.95 V_{NHE} < V < -0.85 V_{NHE}, only **2** is catalytically active. Finally, in the third voltage range (region C) no catalytic activity is observed. Therefore, we compared the TONs of **1** and **2** in region A and studied the catalytic behavior of **2** in region B. In region **A** under identical catalytic conditions (an applied potential of -1.21 V_{NHE}), **1** had an observed TOF of 23 min^{-1} while **2** had an observed TOF of 60 min^{-1} following 30 min of catalysis. It is important to note that the same overall amount of cobalt in solution (*i.e.* twice the concentration of **1** compared to **2**) was used, and that the calculated TOFs are based on the amount of cobalt used not the number of moles of catalyst used. To the best of our knowledge this is one of the first reported examples where a bimetallic metal complex is measurably a better water reduction catalyst than its monometallic counterpart in a similar ligand environment. However, **2** had similar stability to **1** (see Chapter 3 for details) in which there was a period of rapid charge consumption (~ 45 minutes). Following this initial phase of rapid catalysis, there was a severe drop in charge consumption that is associated with catalytic deactivation (**Figure 4.5.**).

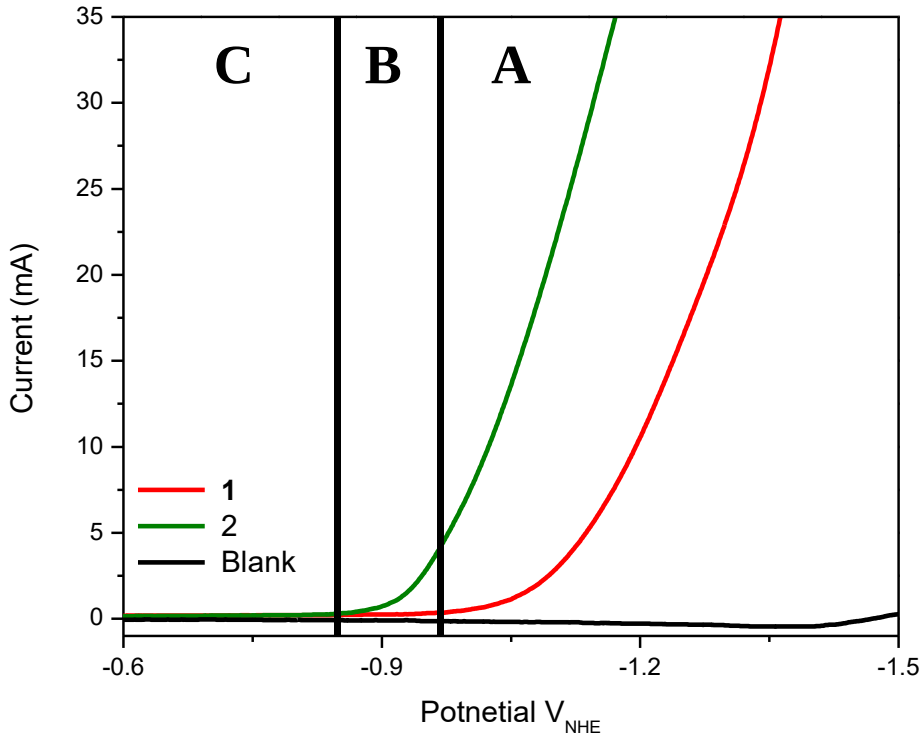

Figure 4.4.: Polarization curves for **1** and **2** in phosphate buffer (1 mol/L, pH 7). Hg-pool working electrode, a Pt auxiliary electrode, and an Ag/AgCl reference electrode. The letters represent the different voltage regions discussed in this chapter.

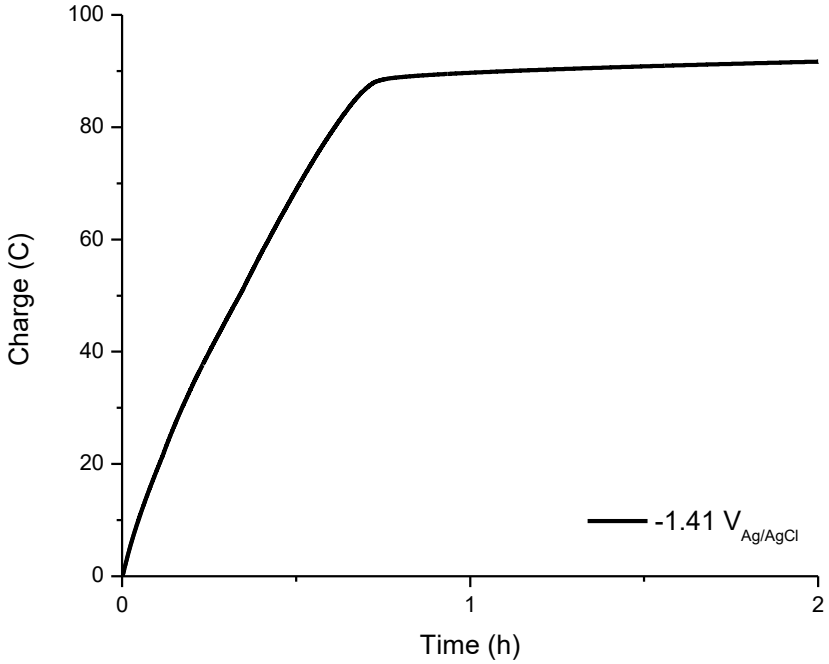

Figure 4.5.: Charge consumption of **2** (4 µmol/L of **2**, 8 µmol/L of Co) in phosphate buffer (pH = 7, 1 mol/L) at an applied potential of -1.21 V_{NHE}.

Conversely, when we ran a bulk electrolysis experiment in region B (at an applied potential of -0.94 V_{NHE}) we observed a much lower TOF of 2.9 min^{-1}. This decrease in the TOF can be directly ascribed to the lower applied potential, since the applied potential is directly related to the driving force for catalysis. However, unlike catalysis in region A in which deactivation took place, catalysis in region B could be sustained for prolonged periods of time. **Figure 4.6.** shows the UV-Visible spectrum of the solution before and after five hours of catalysis. Moreover, following a 20 h catalytic run we were able to observe sustained charge consumption (**Figure 4.7.).** This is in stark contrast to the catalytic behaviour observed in region **A (Figure 4.5.**). We therefore conducted a detailed electronic, and structural study aimed at explaining the observed behaviour.

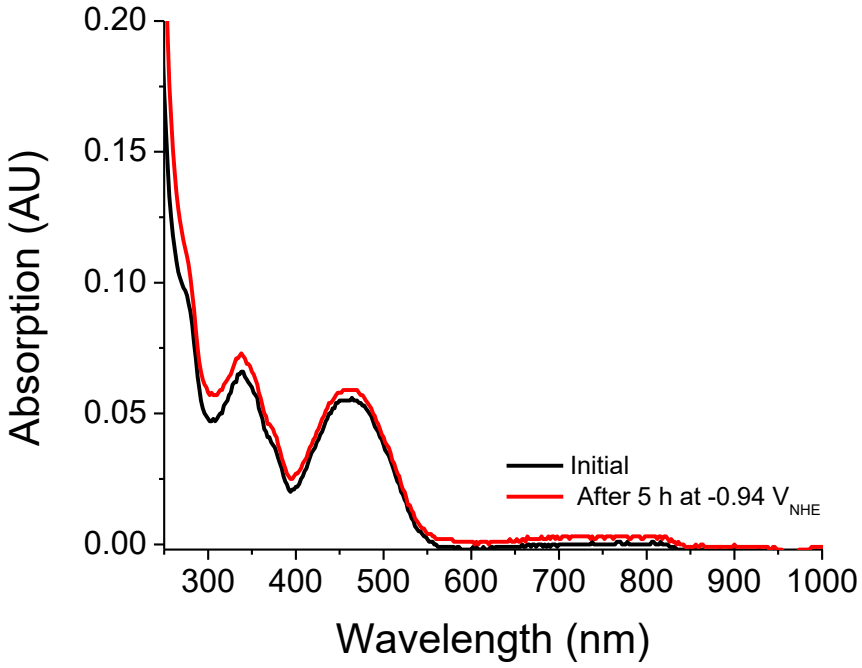

Figure 4.6.: UV-Vis spectrum before and after five hours of catalysis at an applied potential of -0.94 V_{NHE}.

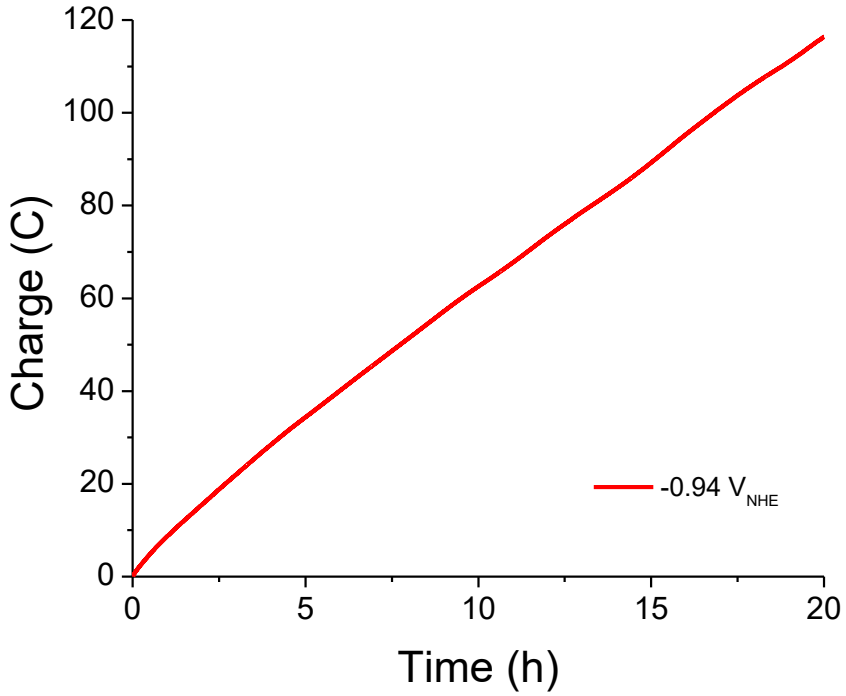

Figure 4.7.: Charge consumption over time of **2** (4 µmol/L), at -0.94 V_{NHE}. Hg-pool working electrode, Pt auxiliary electrode, and Ag/AgCl reference electrode.

We have previously shown that for **1**, deactivation likely takes place due to the formation of valance tautomers in which the metal-reduced state favors the formation of H_2 while the ligand-reduced state favors ligand protonation and eventual deactivation.[60] Aiming at probing whether or not **2** undergoes a similar deactivation mechanism to that of **1**, we performed a detailed structural, spectroscopic, and electrochemical study.

The cyclic voltammograms of **1** and **2** were obtained under identical conditions using acetonitrile as a solvent. The processes which are relevant for catalysis are shown in **Figure 4.8**. Complex **1** shows a quasi-reversible process at -0.93 $V_{Fc/Fc+}$ (E_{pc}) and a reversible process at an $E_{1/2}$ of -1.72 $V_{Fc/Fc+}$ (ΔE = 0.14 V). These two processes are assigned as the sequential reduction from [Co^{III}] to [Co^{II}] and [Co^{II}] to [Co^{I}]. Interestingly, instead of showing a redox behavior that consists of the sequential reduction of the cobalt centers, the CV of **2** shows a similarly quasi-reversible process at -0.94 $V_{Fc/Fc+}$ (E_{pc}) and a reversible process at -1.73 $V_{Fc/Fc+}$ (ΔE = 0.12 V).

These processes are assigned as the sequential two-electron reduction from [Co^{III}-Co^{III}] to [Co^{II}-Co^{II}] and [Co^{II}-Co^{II}] to [Co^{I}-Co^{I}].

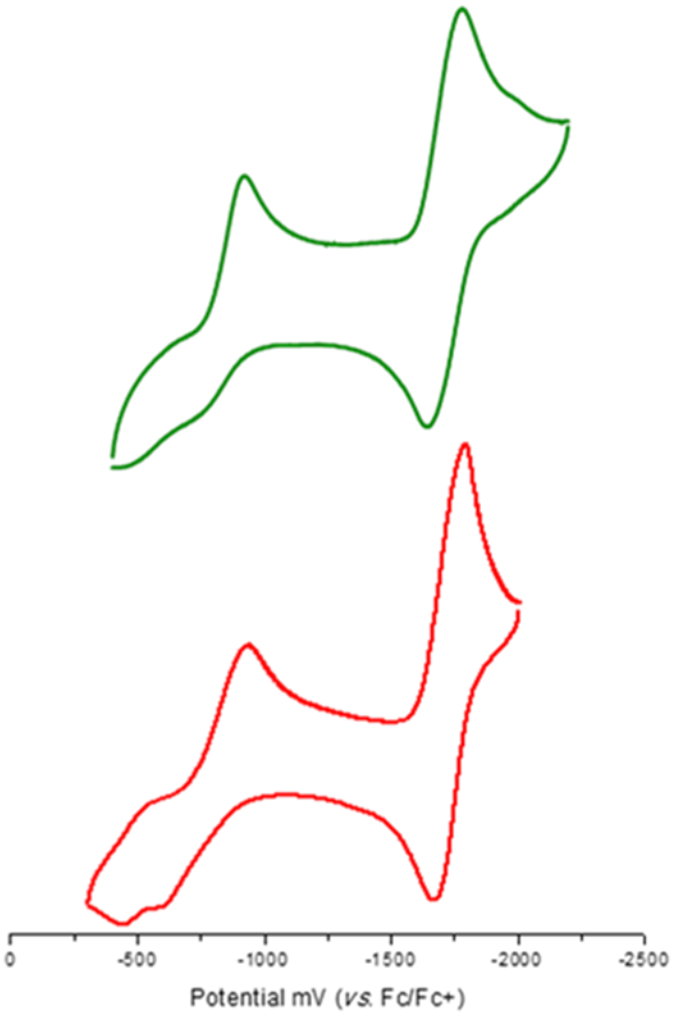

Figure 4.8. The CV of **1** (green) and **2** (red) (1 mM) in CH_3CN. Glassy carbon (WE), Ag/AgCl (RE), Pt wire (AE), $TBAPF_6$ (0.1 M). Ferrocene used as an internal standard.[101]

Our inability to observe the sequential electrochemical reduction of the cobalt centers in **2** suggests that the mixed-valent species are not stable enough to be crystallographically isolated.[61] As such, we focused our attention on isolating the crystal structures of the [Co^{III}-Co^{III}], [Co^{II}-Co^{II}], and [Co^{I}-Co^{I}] species. While we could isolate the [Co^{III}-Co^{III}] and the [Co^{II}-Co^{II}] structures, the [Co^{I}-Co^{I}] structure remains elusive. The crystal structure of $[(Co^{III})_2L^2(pyrr)_4](ClO_4)_2$ consists of the expected geometry where two cobalt centres in a psudo-

octahedral geometry are present in each one of the binding cavities of the ligand (**Figure 4.9.a**). The bond lengths and bond angles are consistent with structurally related monometallic [Co^{III}] complexes.[128-129] The ligand L^2 occupies the equatorial plain and two pyrrolidines are present in the axial position. The doubly reduced $[(Co^{II})_2L^2(pyrr)_2]^0$ (**3**) species was obtained *via* the reaction of **2** with cobaltocene as a stoichiometric reducing agent.[15] The crystal structure of **3** consists of two [Co^{II}] centers in distorted square pyramidal geometries (τ = 0.02) where the ligand L^2 occupies the equatorial plain and two pyrrolidines are present on opposite sides of the plain of L^2 in the axial positions (**Figure 4.9.b**).[135] A comparison of the Co-N bond lengths (**Figure 4.10.**) reveals little deviation in the Co-L^2 bond length. However, there was significant elongation in the Co-pyrrolidine bond length in going from [Co^{III}] to [Co^{II}]. We have previously shown that these observations are consistent with the occupation of the d_{z2} orbital in the transformation from [Co^{III}] in a $^{LS}3d^6$ environment to a [Co^{II}] in a $^{LS}3d^7$ environment. Moreover, the Co-N bond lengths that we observe for **3** are close to the ones that we have reported for the [Co^{II}] equivalent of **1** (**Figure 4.10.**).[60] We are therefore confident in assigning the spin state of [Co^{II}] in this case as a low spin species.

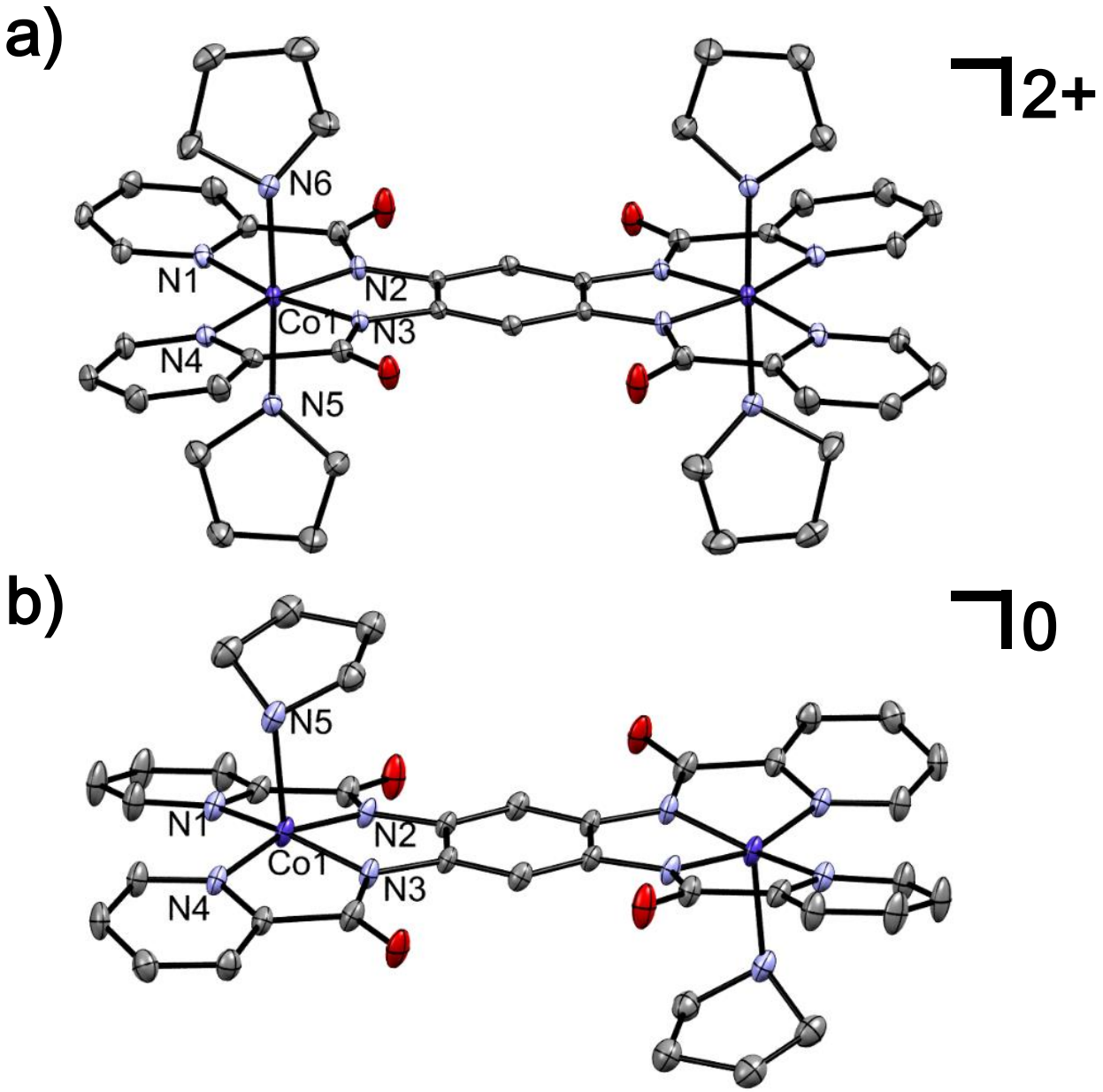

Figure 4.9. (a)The crystal structures of **2** as the perchlorate species. Hydrogens, solvent molecules, and counterions are removed for clarity. Ellipsoids are at 50% probability. Selected bond lengths: Co1-N1 2.000(2), Co1-N4 1.985(2), Co1-N2 1.891(2), Co1-N3 1.890(2), Co1-N5 1.988(2), Co1-N6 1.995(2). **(b)** The crystal structures of **3**. Hydrogens are removed for clarity. Ellipsoids are at 50% probability. Selected bond lengths: Co1-N1 1.985(3), Co1-N4 1.974(3), Co1-N2 1.875(3), Co1-N3 1.887(3), Co1-N5 2.148(3).

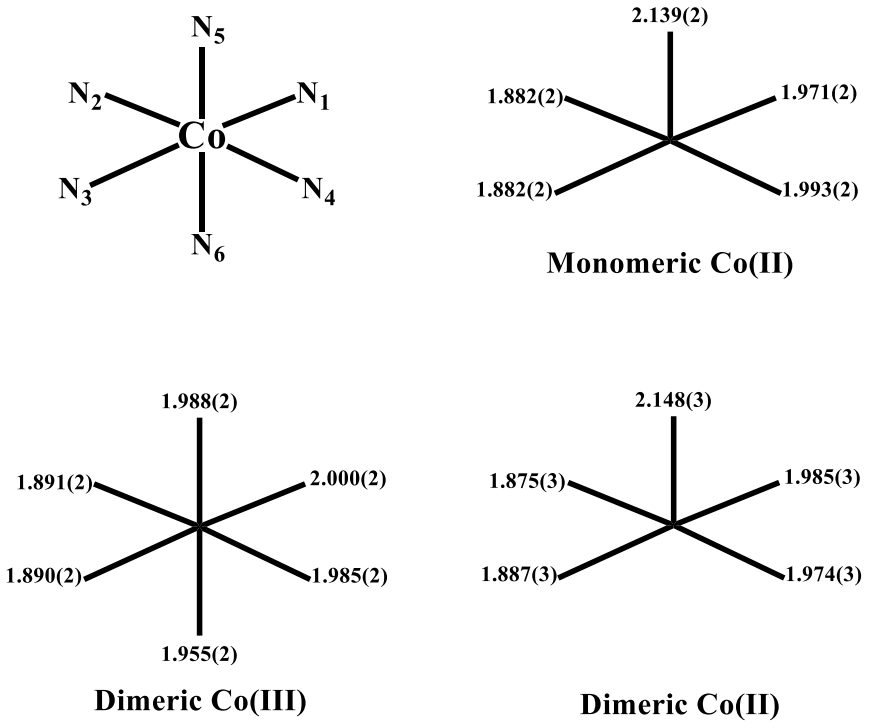

Figure 4.10. A comparison of the Co-N bond lengths for **2**, **3**, and the monomeric [Co^{II}] species discussed in **Chapter 3**.

Having shown that **1** undergoes deactivation due to the tautomeric equilibrium between [Co^{I}-L] and [Co^{II}-$L^{\bullet}$], in which [Co^{I}-L] leads to the catalytic formation of hydrogen and [Co^{II}-$L^{\bullet}$] leads to ligand protonation and eventual demetalation, it was of interest to study if such an equilibrium exists for **2**.[60] While we were unable to crystallographically ascertain the nature of the quadruply reduced $[(Co^{I})_2L^2]^{2-}$ species, we were able to isolate it electrochemically *via* bulk electrolysis. The UV-VIS-NIR spectrum of the electrochemically isolated $[(Co^{I})_2L^2]^{2-}$ is shown in **Figure 4.11**. The spectrum shows high-intensity low-energy transition at 1165 nm with a shoulder at ~1050 nm. These transitions are indicative of the formation of a ligand-based radical and have been assigned as π-π^* transitions centred on the amido-pyridine radical.[60] Therefore, we can conclude that the deactivation that we have observed for **2** is due to a similar mechanism.

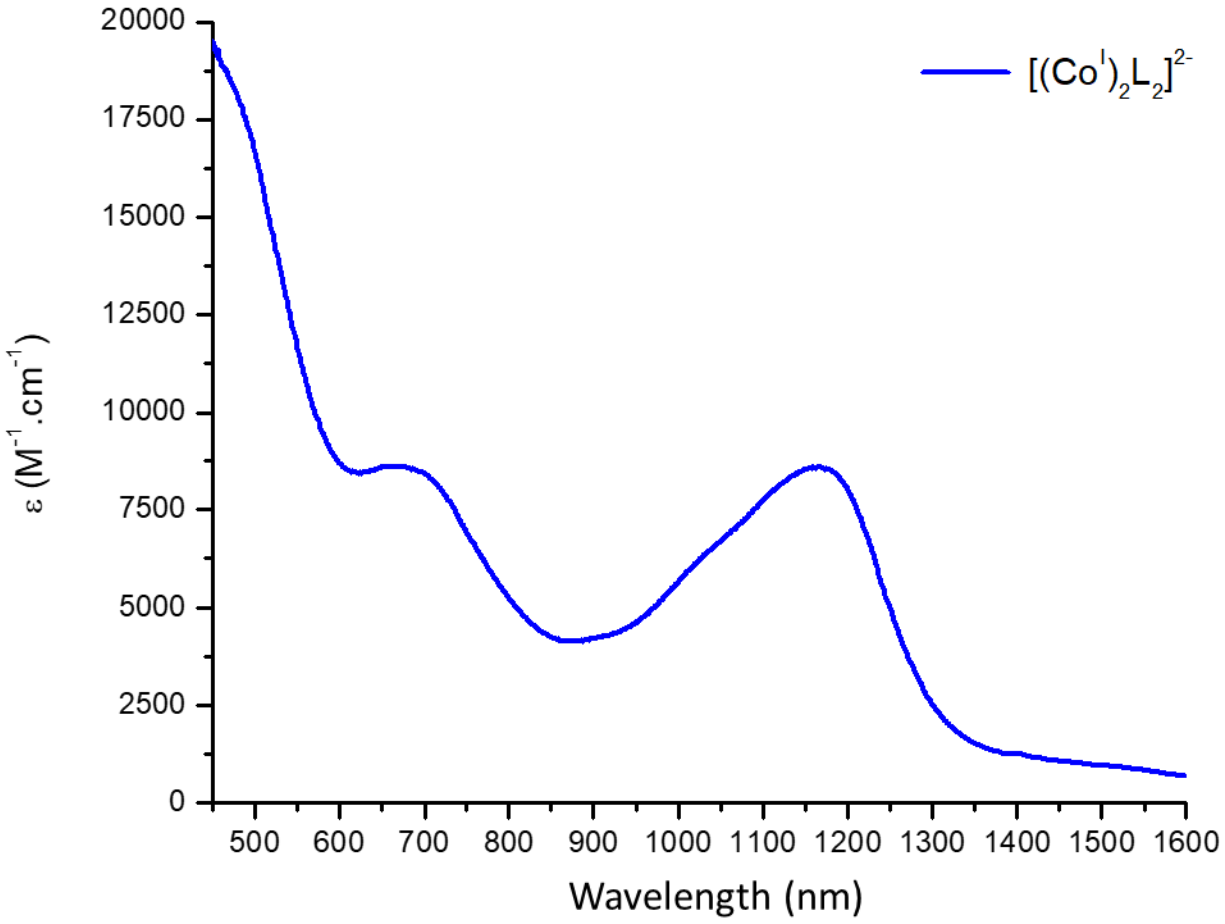

Figure 4.11. The UV-Visible-NIR spectrum of the electrochemically generated $[(Co^{I})_2L^2]^{2-}$.

Taken together, these observations allow us to reach the following conclusions. (i) The different behavior observed in regions A and B (**Figure 4.4.**) suggest that a voltage-dependent mechanism is at play. (ii) The observation of two-electron transfer processes in the CV as opposed to observing sequential one-electron reduction processes seems to disfavor electronic coupling between the two metal centers.[61] Therefore, it seems that the enhancement in activity is not likely due to an electron transfer process between the two metal centers in which one metal center acts as an electron reservoir while the other center performs catalysis. Instead it seems to point to a mechanism in which one of the metal centers is modifying the mechanism through the substituent effect by possibly favoring a PCET pathway as opposed to the direct formation of the

nucleophilic [Co^{I}]. And finally, (iii) the UV-Visible-NIR spectrum of $[(Co^{I})_2L^{2}]^{2-}$ is consistent with the formation of a ligand-based radical which we have previously shown to be directly linked to catalyst deactivation.[60] As such it seems that under relatively negative applied potentials (**Figure 4.4.**, potential region A) the [Co^{I}] state is energetically accessible and can therefore provide a pathway for catalyst deactivation. These conclusions are summarized in **Figure 4.12.** which depicts the proposed voltage-dependent mechanism. The green pathway is only accessible at low applied potentials (**Figure 4.4.**, voltage region B) while the red pathway is accessible at more negative applied potentials (**Figure 4.4.**, potential region A).

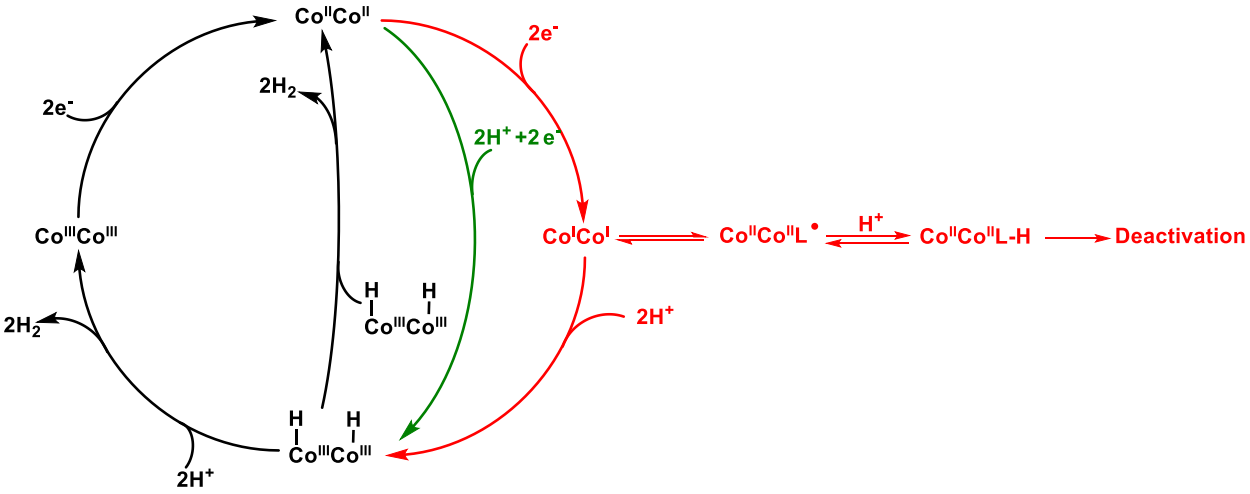

Figure 4.12. The proposed voltage-dependent catalytic mechanism for **2**. The green pathway is accessible at low applied potentials, and the red pathway is accessible at more negative applied potentials.

4.4. Conclusions

In conclusion, we have reported on a novel bimetallic catalytic platform capable of performing water reduction under neutral aqueous conditions. Compared to the monometallic catalyst **1**, the bimetallic catalyst **2** showed a marked improvement in overpotential and in the observed turnover frequencies. Moreover, we observed two potential regions in which **2** was catalytically active. In region A (more negative potentials), **2** had similar stability to **1** and there was a marked decrease in charge consumption following the initial phase of rapid catalysis. In

region B (less negative potentials), there was a significant improvement in catalytic stability of **2**. Aiming at probing this apparent voltage-dependent behavior we performed a structural, electronic, and electrochemical study which led us to conclude that in region A, [Co^{I}] seems to be inaccessible and a mechanism that favors a PCET from [Co^{II}] to [Co^{III}-H^{-}] is at play. By avoiding [Co^{I}], the deactivation side reactions that are based on valence tautomerism between [Co^{I}-L] and [Co^{II}-$L^{\bullet}$] are avoided. However, in region B the potentials are negative enough to access the [Co^{I}] state which leads to the eventual catalyst deactivation.

CHAPTER 5. THE IMMOBILIZATION OF A LONG-CHAIN COBALT AMIDO COMPLEX ON CARBON BLACK FOR HETEROGENEOUS WATER OXIDATION.

5.1. Introduction

Surface functionalization is pivotal to enable the use of homogenous catalysts anchored onto conductive solid supports. In this manner, integrated electrochemical water splitting devices can be developed in which water oxidation occurs at the anode and proton reduction occurs at the cathode. Traditionally, such electrodes are made from solid state materials such as metal oxides or hydroxides. However, understanding the surface chemistry of such extended and tridimensional materials is challenging. On the other hand, understanding the chemistry behind surfaces that are functionalized with discrete coordination complexes is more attainable due to the well-known electronic signatures of molecular materials. As such improving catalytic activity can be achieved using rational ligand design and established electrochemical and spectroscopic methods.

The water splitting reaction involves two half-reactions; water oxidation and proton reduction. With a standard potential of 1.23 V_{NHE}, water oxidation is the more energetically demanding of the two half-reactions in water splitting. This high-energy requirement is imparted by the need to perform four-electron chemistry and form O-O bonds. The mechanisms of water oxidation require the formation of high-valent oxo ($[M^{IV}=O]$, or $[M^{V}=O]$) or hydroperoxo ($[M^{III}\text{-O-O-H}]$) species. In order to lower the activation barrier required to reach such highly oxidized states needed for catalysis, redox active ligands have been utilized.[146-147] This is due to the formation of a radical-based species instead of the expected high-valent tautomer[148] in the electron-transfer sequence $[M^{n-1}L]^0 \xrightarrow{-e^-} [M^{n-1}L^{\bullet}]^+ \leftrightharpoons [M^{n}L]^+$. When the last equilibrium step favors the $[M^{n-1}L^{\bullet}]^+$ product the oxidized ligand acts as a catalytic electron reservoir prone to degradation.

Recent efforts have focused on anchoring molecules onto conductive solid supports in an attempt to favor the high-valent $[M^nL]^{n+}$ product, enhancing robustness of catalysts and favoring water splitting.[76-77, 149] We have recently shown that fluorine-doped tin oxide (FTO) coated glass can be functionalized using physisorbed Langmuir-Blodgett films of a procatalytic phenolate-rich cobalt complex.[75] The resulting modified electrode is an excellent water oxidation catalyst with an overpotential of 0.5 V. However, structural rearrangement takes place after applying a potential bias. This transformation coupled with the labor-intensive layer-by-layer deposition process precludes the large-scale application of the approach.

Produced by the incomplete combustion of petrochemicals, carbon black (CB) has been used as solid support along with Nafion to drive catalytic water oxidation.[150] As such, we hypothesized that CB can be functionalized with an amphiphilic metal complex, and that the van der Waals interactions between substrate and complex will lead to more robust water oxidation catalysts. Therefore, similar to other systems we reported in the recent past,[55-57, 75] we designed a new ligand with two octadecyloxy groups incorporated into the backbone. These aliphatic groups (i) serve as hydrophobic backbones to anchor the molecule onto CB, and (ii) lower the oxidation potential required for water oxidation.

5.2. Experimental

Ultrapure water (18.1 MΩ) was used in all manipulations. All other solvents and reagents were used from commercial sources and were not further purified. Proton nuclear magnetic resonance spectroscopy (^{1}HNMR) spectra were recorded on a Varian 400 MHz or 600 MHz spectrometer. Fourier transform infrared spectroscopy (FTIR) spectra were recorded on a Bruker Tensor 27 spectrometer using KBr pellets recorded between 4000 and 600 cm^{-1}. Elemental analysis was performed by Midwest Microlabs, Indianapolis, Indiana and measured using an

Exeter CE440 CHN analyzer. Cyclic voltammograms in organic solvents were recorded using a BAS 50W electrochemical analyzer. $TBAPF_6$ was used as a supporting electrolyte, an Ag/AgCl electrode was used as a reference electrode and a Pt wire was used as the auxiliary electrode. The voltammograms were recorded under an Ar atmosphere and ferrocene was added as an internal standard at a scan rate of 0.1 V/s.[101] XPS spectra were recorded using a Kratos Axis Ultra XPS, all the spectra were calibrated using the C 1s at 284.8 eV as a charge reference . XPS spectra of the electrode itself did not show any discernable Co peaks, therefore the functionalized carbon black was removed from the surface of the electrode by sonicating it in ethanol. Then the ethanol was removed and the concentrated sample was used for XPS analysis.

5.2.1. Synthetic procedures

The ligand ($H_2L^{OC18H37}$) was first reported by Dr. Lanka D. Wickramasinghe[151] and was synthesized using the multi-step procedure depicted in **Figure 5.1**. Where necessary standard Schlenk line techniques were used. The ligand and cobalt complex where characterized using

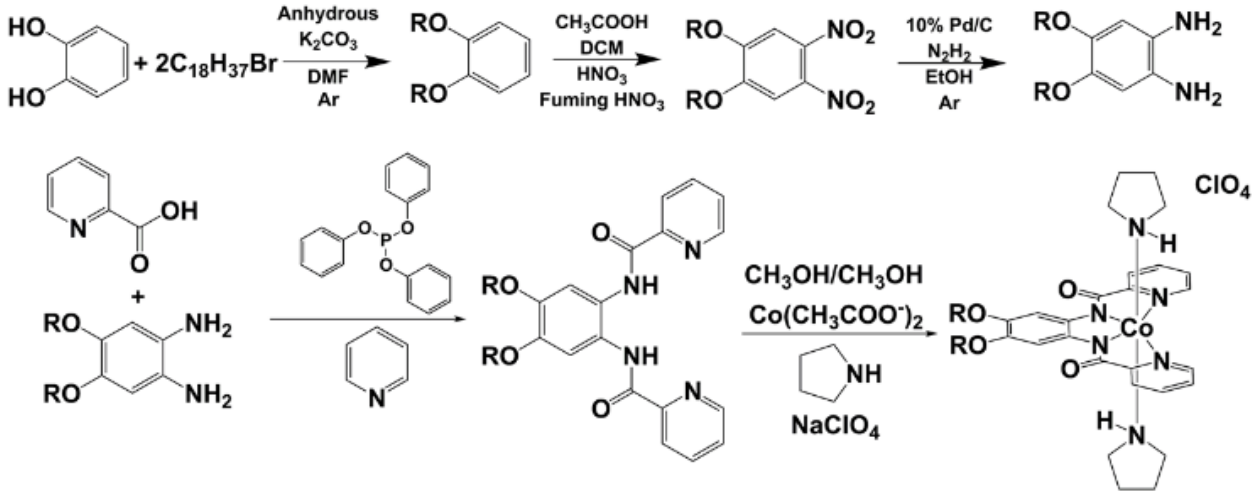

NMR, FTIR, and MS. Elemental analysis was performed for the metal complexes.

Figure 5.1. The multistep synthetic procedure used to synthesize ligand ($L^{OC18H37}$); R = $C_{18}H_{37}$.

Synthesis of 1,2-bis(octadecyloxy)benzene.

To a solution of catechol (3.50 g, 31.8 mmol) and anhydrous K_2CO_3 (16.0 g, 116 mmol) in anhydrous dimethylformamide (DMF) (52.5 mL), a solution of 1-bromooctadecane (23.4 g, 70.2 mmol) in DMF (70 mL) was added dropwise under inert conditions. The reaction was allowed to reflux for 18 hours after which it was poured into ice-cold water (150 mL) and subsequently extracted with dichloromethane (CH_2Cl_2) (100 mL). The organic layer was dried over anhydrous Na_2SO_4. The solvent was removed by rotary evaporation and the remaining yellow oil was dissolved in a 19:1 mixture of hexane and ethyl acetate. The solution was filtered through silica under vacuum. The isolated yellow solution was concentrated to half of its original volume and refrigerated to yield a white precipitate. Yield: 72 %. ^{1}H NMR, ppm ($CDCl_3$, 400 MHz): δ 6.88 (s, $4H^{ph}$), δ 3.98 (t, $4H^{OCH2}$), δ 1.82 (m, $4H^{CH2}$), δ 1.46 (m, $4H^{CH2}$), δ 1.25 (s, $56H^{CH2}$), δ 0.88 (t, $6H^{CH3}$).

Synthesis of 1,2-dinitro-4,5-bis(octadecyloxy)benzene.

2.05 g (3.33 mmol) of 1,2-bis(octadecyloxy)benzene were dissolved in 48 mL of a 1:1 CH_2Cl_2 : acetic acid mixture. The reaction mixture was subsequently placed in an ice bath and 3.50 mL of nitric acid were added. Then the reaction was stirred at room temperature for 30 minutes and then cooled back down in an ice bath before 8.50 mL of fuming HNO_3 were added. The reaction mixture was stirred at room temperature for 72 hours before being poured into water (100 mL, 0˚C). The organic layer was washed with (3 x 100 mL) of saturated $NaHCO_3$, and brine solution. The organic layer was subsequently dried over Na_2SO_4. The organic solvent was removed by rotary evaporation and recrystallized from acetone to yield yellow crystals. Yield: 86%. ^{1}H NMR, ppm ($CDCl_3$, 400 MHz): δ 7.29 (s, $2H^{ph}$), δ 4.09 (t, $4H^{OCH2}$), δ 1.85 (m, $4H^{CH2}$), δ 1.47 (m, $4H^{CH2}$), δ 1.25 (s,$56H^{CH2}$), δ 0.88 (t, $6H^{CH3}$).

Synthesis of N,N'-(4,5-bis(octadecyloxy)-1,2-phenylene)dipicolineamide ($H_2L^{OC18H37}$)

These reactions were performed under inert conditions. A mixture of 1,2-dinitro-4,5-bis(octadecyloxy)benzene (1.5 g, 2.03 mmol) and Pd/C (65 mg) was refluxed in the presence of $N_2H_4.H_2O$ overnight using EtOH as a solvent. The mixture was filtered through celite and allowed to dry under vacuum. To this flask, a mixture of picolinic acid (0.53 g, 4.25 mmol) and triphenyl phosphite (1.32 g, 4.25 mmol) in anhydrous pyridine was cannulated. Following this step, the reaction mixture was heated overnight in an oil bath. The product was crashed out by the addition of methanol to obtain a pale-yellow precipitate. Yield: 50%. ESI (m/z^+) = 855.7 (100 %) for [$C_{54}H_{86}N_4O_4 + H^+$]. ^{1}H NMR, ppm ($CDCl_3$, 400 MHz): δ 10.17 (s, $2H^{NH}$), δ 8.57 (dd, $2H^{py}$), δ 8.30 (dd, $2H^{py}$), δ 7.93 (td, $2H^{py}$), δ 7.48 (td, $2H^{py}$), δ 7.44 (s, $2H^{ph}$), δ 4.04 (t, $4H^{OCH2}$), δ 1.83 (m, $4H^{CH2}$), δ 1.47 (m, $4H^{CH2}$), δ 1.25 (s,$56H^{CH2}$), δ 0.87 (t, $6H^{CH3}$).

Synthesis of the complex [$Co^{III}(L^{OC18H37})(pyrr)_2$]$ClO_4$

0.200 g (0.232 mmol) of the ligand **$H_2L^{OC18H37}$** dissolved in 1 mL $CHCl_3$ 0.060 g (0.240 mmol) of $Co(CH_3COO^-)_2.4H_2O$ dissolved in 1 mL of methanol were added dropwise following this addition 0.5 mL (excess) of pyrrolidine were added. The solution was stirred overnight at room temperature then it was filtered, and oxygen was bubbled in for 10 minutes. Precipitation was induced by adding 0.020 g (0.269 mmol) of $NaClO_4$. Yield: 32 mg 47%. ESI (m/z^+) = 911.58251 (100 %) for [$C_{54}H_{84}N_4O_4Co^+$]. IR (KBr, cm^{-1}) 3430 (ν_{N-H}), 2852-2921 (ν_{C-H}), 1625 ($\nu_{C=O}$), 1598($\nu_{C=N\ pyridine}$), 1207 (ν_{C-O-C}), 1091 (ν_{ClO4}). ^1H NMR, ppm ($CDCl_3$, 600 MHz): δ 9.76 (d, $2H^{py}$), δ 8.60 (s, $2H^{ph}$), δ 8.26 (t, $2H^{py}$), δ 8.22 (d, $2H^{py}$), δ 4.06 ($4H^{OCH2}$), δ 3.05 ($2H^{NH}$), δ 2.10 ($4H^{pyr}$), δ 1.25-1.66 (m, 72H), δ 0.86 ($6H^{CH3}$). Anal. Calc. for [$C_{62}H_{102}CoN_6O_8Cl$]: C, 64.54; H, 8.91; N, 7.28% Found: C, 64.49; H, 8.91; N, 7.02%.

5.2.2. Ink preparation

Carbon black (6 mg) was suspended in CH_2Cl_2 and sonicated for 5 minutes. Following sonication, a known amount of a stock solution of [$Co^{III}(L^{OC18H37})(pyrr)_2$]$ClO_4$ (4 mg/mL in CH_2Cl_2) was added to the carbon black. The mixture was sonicated for a further fifteen minutes. Following sonication, ~40 mL of ethanol were added to the carbon black suspension. The suspension was centrifuged, the solvent was decanted, and the carbon black was allowed to dry overnight under ambient conditions. The dry carbon sample was re-suspended in 0.300 mL water, 0.600 mL ethanol, and 0.300 mL isopropanol. This suspension was sonicated for fifteen minutes and then 0.300 mL of Nafion were added. The suspension was further sonicated for fifteen minutes to form the ink used for catalysis.

5.2.3. Catalytic measurements

Cyclic Voltammetry (CV): All cyclic voltammograms were recorded using an EC Epsilon potentiostat equipped with an RDE2 rotating disc electrode. The three-electrode setup included an Ag/AgCl reference electrode, a Pt wire auxiliary electrode, and a glassy carbon working electrode (surface area = 0.07 cm^2). 5 µL of the ink were deposited on the glassy carbon surface of the working electrode and dried under an infrared heat lamp for 5 minutes. The cyclic voltammograms were measured at a scan rate of 10 mV/S at 1600 rpm in a 1 M KOH solution. After measuring the potentials against Ag/AgCl, they were converted to the standard hydrogen electrode (RHE) using **equation 5.1.** Additionally, using the iR compensation function of the Epsilon software, the resistivity of the solution was measured and corrections were calculated using **equation 5.2.**

$$E_{NHE} = E_{Ag/AgCl} + 0.197 \text{ (}\mathbf{equation\ 5.1.}\text{)}$$

$$E_{NHE} = E_{Ag/AgCl} + 0.197 - iR \text{ (}\mathbf{equation\ 5.2.}\text{)}$$

Bulk Electrolysis and Faradaic Efficiency: Bulk electrolysis was performed under an overpotential of 0.7 V in a custom H-type cell that is split into two compartments by a fine frit. The auxiliary electrode, a Pt coil, was placed in one compartment, and the reference (Ag/AgCl) and working electrodes were placed in the other. The working electrode was prepared by depositing 100 uL of the functionalized ink onto a 1 cm x 4 cm piece of carbon cloth, allowing it to dry for 15 minutes, and threading it onto a copper wire.

A GOW-MAC series 400 gas chromatograph equipped with a TCD detector and a 8 ft x 1/8 in., 5 Å molecular sieve column held at 60 ˚C were used to quantify the amount of oxygen produced. Helium was used as the carrier gas and flowed at a rate of 30 mL/min. Atmospheric nitrogen was used as an internal standard.

5.2.4. Computational methods

Electronic structure calculations were performed, with Jordyn Burdick (undergraduate researcher) in conjunction with Dr. Bishnu Thapa in the Schlegel Group at Wayne State University, using the Gaussian series of programs (version g09 revision E01).[152] Density Functional Theory (DFT) calculations were carried out using the B3LYP* functional.[115] Geometries were optimized using B3LYP* with the SDD basis set with effective core potential (ECP)[117] for the cobalt atom and 6-31G(d,p) basis set for all other atoms. The energetics of structures with different spin states were compared and lowest energy structures were used for the proposed catalytic cycle. The structures with lowest Gibbs free energy were reoptimized with the SDD (for Co) and 6-31+G(d,p) (for all other atoms) basis sets to obtain more accurate energies.[118-119] The SMD implicit solvation model was used to incorporate solvation effects in water and was included in all the geometry optimizations.[120] Previous studies[153-156] have shown that a small number of explicit water molecules need to be included to account some of the short-range interactions while modeling anions such as OH^- in aqueous solution using SMD implicit solvation model. Therefore, the lowest energy structures involved in the catalytic cycle were optimized with two explicit waters forming H-bonds with OH/O^-/OOH/OO^- moieties in SMD implicit solvation. All the geometries were confirmed to be minima on the potential energy surfaces by performing vibrational frequency calculation and had no imaginary frequency. Thermal and entropy contribution to for the free energies were calculated by standard statistical thermodynamical methods using unscaled B3LYP* frequencies and rigid rotor/harmonic oscillator approximation at 298.15 K. The converged wave functions were tested for SCF stability.

For a redox reaction, $A_{(aq)} \rightarrow A^{n+}_{(aq)} + ne^-_{(aq)}$, the standard redox potential is given by equation 5.3. where $\Delta G^*_{(aq)} = G^*_{A(aq)} - G^*_{A^{n+}(aq)} - G^*_{e(g)}$ is the standard free energy change for a redox couple in solution. Where. $G^*_{e(g)}$ = 0.867 kcal/mol is the free energy of electron at 298.15 K,[154, 157] obtained from literature, F is Faraday's constant (23.06 kcal/(mol V)), and n is the number of electrons, and SHE is the absolute potential of standard hydrogen electrode (4.281 V).[158-160]

$$E^o_{(aq)} = \frac{-\Delta G^*_{(aq)}}{nF} - SHE \qquad \textbf{(equation 5.3.)}$$

The pH dependent redox potential can be obtained by solving Nernst half shell equation where E^o is the standard redox potential at pH 0 (**equation 5.4.**). The redox potential at a particular pH can be obtained by including the equilibrium concentration of each of the relevant species at that pH by using acid dissociation constants (K_a's). For low ionic strength, the pH dependent redox potential is given by (**equation 5.5.**), where AH is the reduced form, $AH^{\bullet+}$ is the 1 electron oxidized form, and $A^\bullet$ is the oxidized form after proton coupled electron transfer process.

$$E_{1/2} = E^o - \frac{RT}{nF} \ln\left(\frac{[Red]}{[Ox]}\right) \qquad \textbf{(equation 5.4.)}$$

$$E_{pH} = E^o_{A^\bullet, H^+/AH} - \frac{RT}{nF} \ln\left(\frac{10^{-pK_a} + 10^{-pH}}{10^{-(pK_a + pH)}}\right) \qquad \textbf{(equation 5.5.)}$$

The aqueous phase free energy of proton is calculated as in **equation 5.6.**, where, $\Delta G^*_{H^+(aq)} = -265.9$ kcal/mol is the solvation energy of proton taken from literature[158-160], $G^o_{H^+(aq)} = -6.29$ kcal/mol is the gas phase standard free energy of proton, and ΔG^{corr} = 1.89 kcal/mol is the correction term for conversion of standard state of 1atm in gas phase to the standard state of 1M in solution.[157, 161]

$$G^{*}_{H^{+}(aq)} = G^{o}_{H^{+}(aq)} - \Delta G^{*}_{H^{+}(aq)} - \Delta G^{corr}$$ (**equation 5.6.**)

5.3. Results and discussions

The ligand H_2L^{OC18} was prepared *via* a multistep synthetic route outlined in **Figure 6.1.** that involved the functionalization of catechol with octadecyl groups to produce bis-octadecyloxy benzene. This precursor was then nitrated yielding 1,2-dinitro-4,5-bis(octadecyloxy)benzene that was subsequently reduced to form the air sensitive precursor 4,5-bis(octadecyloxy) benzene-1,2-diamine. The diamine was treated with picolinic acid to yield the ligand N,N'-(4,5-bis(octadecyloxy)-1,2-phenylene)dipicolineamide, H_2L^{OC18}.[114]

The complex $[Co^{III}(L^{OC18})(pyrr)_2]ClO_4$ (**1**) contains a doubly deprotonated $(L^{OC18})^{2-}$ ligand and was prepared following a modification to the previously reported procedure[128-129] in which stoichiometric amounts of H_2L^{OC18} were treated with cobalt acetate in presence of pyrrolidine. After stirring under aerobic conditions, **1** was precipitated using $NaClO_4$. Catalyst **1** was thoroughly characterized using ^{1}HNMR, FTIR, mass spectrometry (MS), and elemental analysis. A strong peak in the FTIR spectrum at 1091 cm^{-1} confirmed the presence of a perchlorate counter ion. This observation coupled with the occurrence of sharp peaks in the NMR spectrum (**Figure 5.2.**) suggests that we have formed a $[Co^{III}]$ complex in a pseudo-octahedral $^{LS}3d^6$ environment. High-resolution mass spectrometry (HRMS) shows a peak cluster at 911.5825 m/z corresponding to the metal complex without the two axial pyrrolidines. The elemental analysis results confirm these structural assignments.

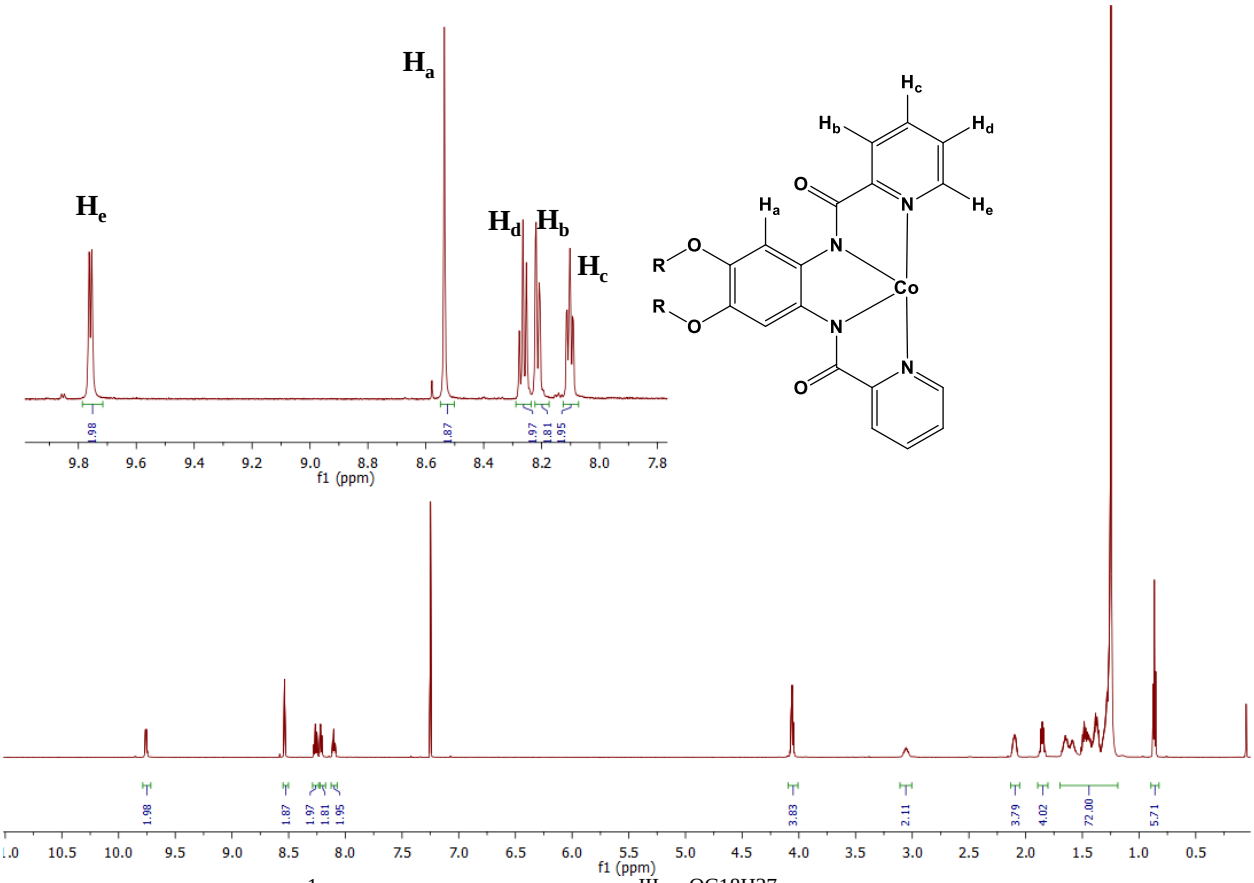

Figure 5.2. The ^{1}H NMR spectrum of $[Co^{III}(L^{OC18H37})(pyrr)_2]ClO_4$ taken in $CDCl_3$.

The CV of **1** was taken in CH_2Cl_2 in the presence of tetrabutyl-ammonium hexafluorophosphate ($TBAPF_6$) as a supporting electrolyte. The CV (**Figure 5.3.**) shows four independent redox events consisting of two oxidative and two reductive processes. The irreversible reductive processes at -1.01 and -1.77 $V_{Fc/Fc+}$ (EP_c) are tentatively assigned as the sequential reduction from $3d^6$ [Co^{III}] to $3d^7$ [Co^{II}] and [Co^{II}] to $3d^8$ [Co^{I}]. Two oxidation process at 0.27 $V_{Fc/Fc+}$ (ΔE = 92 mV, $|I_{pa}/I_{pc}|$ = 0.94) and 0.76 $V_{Fc/Fc+}$ (ΔE = 94 mV, $|I_{pa}/I_{pc}|$ = 1.45) are respectively associated with the formation of the high valent $3d^5$ [Co^{IV}] and possibly $3d^4$ [Co^{V}] species, but have been rather described as amido to amidyl radical transformations in unsubstituted systems.[130-131] It is interesting to note that compared to our previously studied and structurally related $[Co^{III}(L)(pyrr)_2]PF_6$ system with a similar non-alkoxo functionalized ligand,

the current oxidation processes occur at potentials that are about 0.5 V less positive.[60] This decrease in the oxidative potential is associated with the electron donating effect of the alkoxy chains.[77]

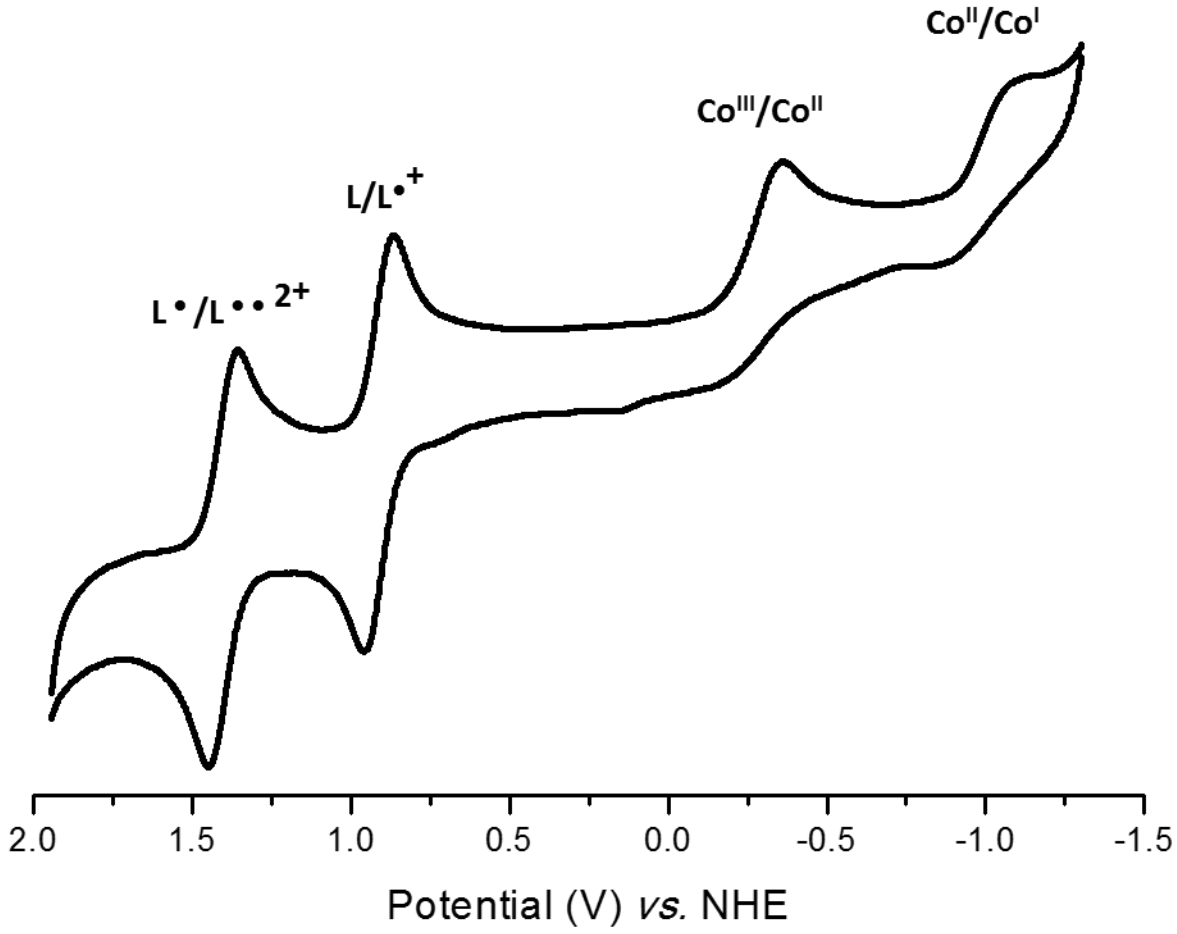

Figure 5.3. The CV of $[Co^{III}(L^{OC18})(pyrr)_2]ClO_4$ (1mM) in CH_2Cl_2. $TBAPF_6$ supporting electrolyte, glassy carbon (WE), Ag/AgCl (RE), Pt wire (AE). Ferrocene is used as an internal standard.[101]

The X-band EPR spectrum of the electrochemically generated singly oxidized cobalt complex, nominally $[Co^{IV}(L^{OC18})(pyrr)_2]^{2+}$, revealed a narrow isotropic signal at g = 2.00, close to the free electron g-value, with a line width of 3.5 mT (**Figure 5.4.**). The typical EPR signals expected for either HS or LS $[Co^{IV}]$ complexes are absent. Therefore, the observed inflection is consistent with an S = ½ state associated with the formation of a radical-bearing species like $[Co^{III}(L^{OC18\bullet})(pyrr)_2]^{2+}$. These conclusions are also supported by DFT calculations. For this S = ½ state the spin density plot (**Figure 5.5.a**) revealed a delocalized unpaired electron on the diamine moiety of the ligand, rather than on the metal center. This observation is in line with our previous report on the redox activity of phenylene diamine bridging moieties.[162] The doubly oxidized species is most stable as a diamagnetic singlet (S = 0) with no observable spin density due to its closed shell. However, the lowest-unoccupied LUMO (**Figure 5.5.b**) was calculated as ligand-based. This data suggests the assignment of the second oxidation as being ligand-based and best described as $[Co^{III}(L^{OC18\bullet\bullet})(pyrr)_2]^{3+}$.

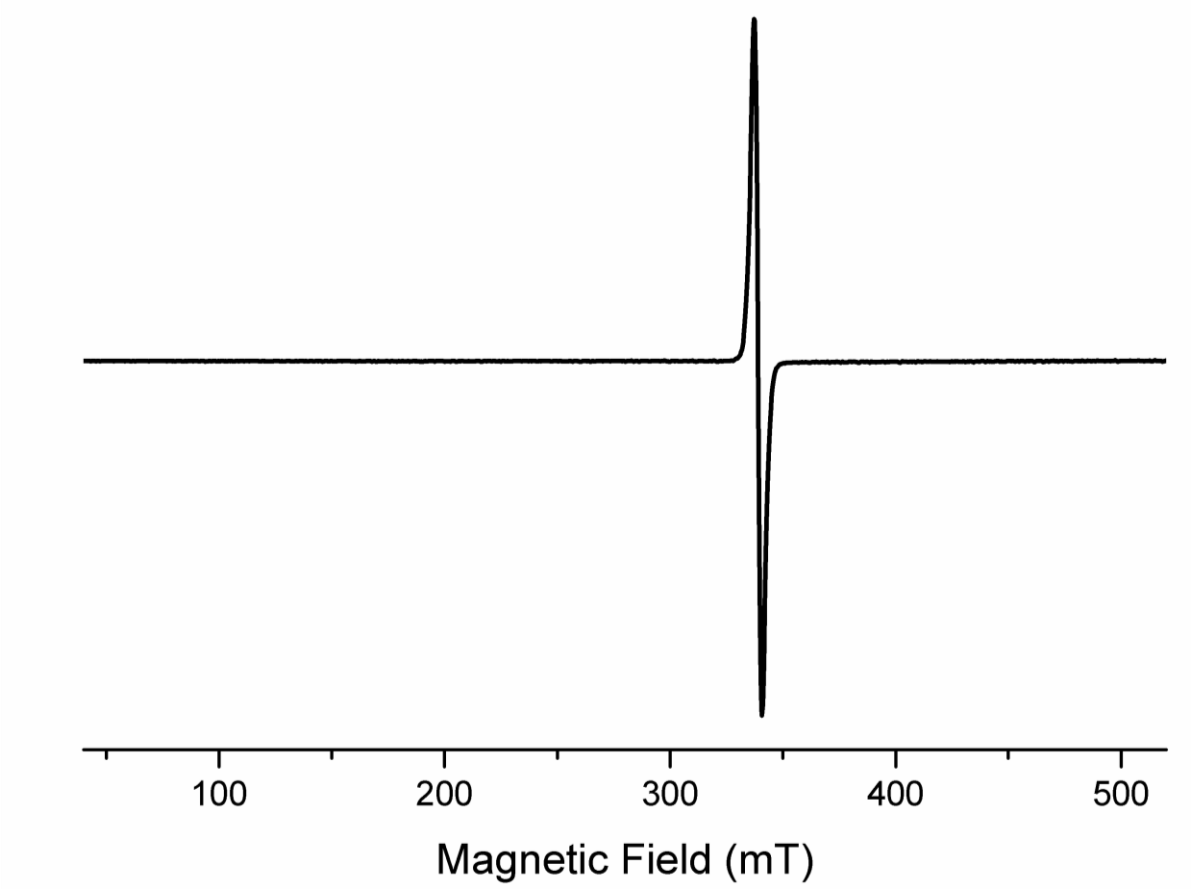

Figure 5.4. Continuous wave (cw) X-band EPR spectrum of the electrochemically singly oxidized cobalt complex in dichloromethane at T=30 K.

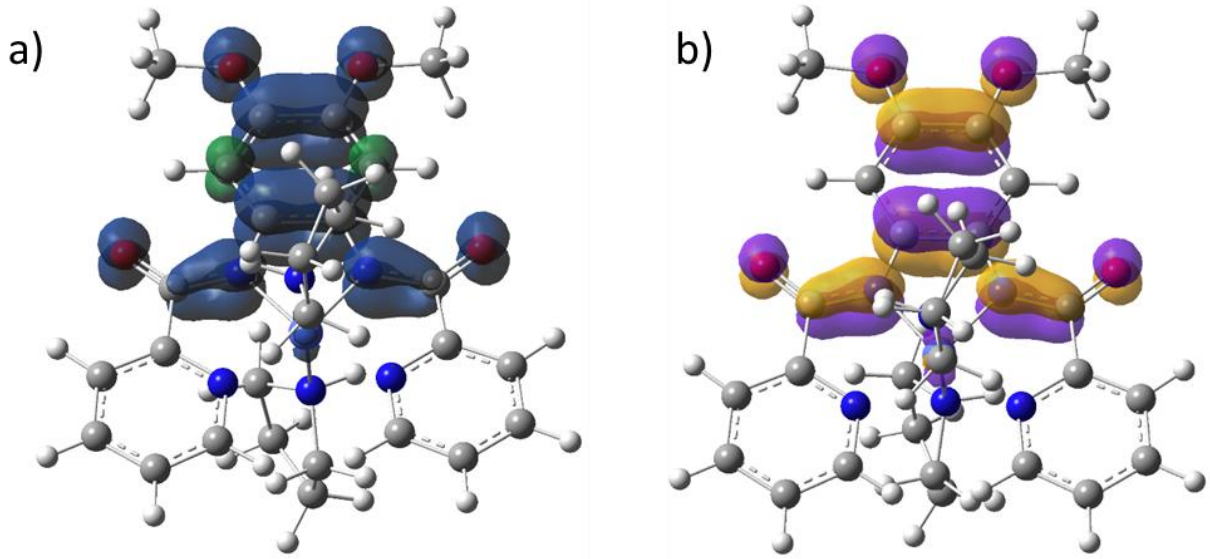

Figure 5.5. (a) The spin density plot for $[Co^{III}(L^{OC18\bullet})(pyrr)_2]^{2+}$, (b) the LUMO for $[Co^{III}(L^{OC18\bullet\bullet})(pyrr)_2]^{3+}$.

Although our observations agree with previous assignments[130-131] that favor formation of ligand radicals, Åkermark *et al* [163] have shown that a related Ru complex can efficiently catalyze water oxidation. Furthermore, Kim and coworkers[164-166] have shown that Fe, Co, and Mn ions act as oxygen transfer agents in similar $[N_4]$ planar environments and that high-valent oxo species were observed *in situ*. These same oxo-species stabilized during oxygen atom transfer are essential intermediates in the water oxidation mechanism. These observations suggest that the observed $[Co^{III}(L^{OC18\bullet})]^+$ and the putative $[Co^{IV}(L^{OC18})]^+$ species may be very close in energy, and that an oxo species may be better described as nominally $[Co^{IV}{=}O(L^{OC18})]^+$. Therefore, we hypothesized that **1** could perform water oxidation as a molecular catalyst. Evaluation of these results allows us to infer whether the metal or the bis-amidopyridine ligand is associated with the high-oxidation state required for catalysis. In order to assess the catalytic properties of $[Co^{III}(L^{OC18})(pyrr)_2]ClO_4$ (**1**), we anchored the molecule onto the surface of CB to yield an assembly denoted as **1@CB**. This was done by adding a solution of **1** to a suspension of CB in CH_2Cl_2. Then, ethanol was added to precipitate the resulting suspension. The precipitate was

isolated by centrifuging the sample. Following the decantation of the supernatant, the precipitate was dried overnight under ambient conditions and re-suspended using a 2:1:1:1 mixture of ethanol : isopropanol : water : Nafion. The sample was ultrasonicated to form the homogenous ink that was used in catalysis. Attempts to prepare a similar ink based on the unsubstituted $[Co^{III}(L)(pyrr)_2]ClO_4$ were unsuccessful.

The **1@CB** ink was tested for catalysis using a rotating disc electrode operating at 1600 rpm in a 1 M KOH solution. **Figure 5.6.** shows the iR-corrected polarization curves obtained for **1@CB** (black trace) in comparison to the blank CB (red trace). Significant current enhancement is attained by **1@CB** with onset overpotential of 0.32 V. At an overpotential of 0.37 V the current density reaches 10 mA/cm^2, an important figure of merit in the development of solar cells operating at 10% efficiency.[104] Remarkably, **1@CB** has an overpotential at 10 mA/cm^2 on par with recently reported nanostructured materials.[4, 104, 150, 167-169] Furthermore, our approach is advantageous because it enables detailed mechanistic studies, which can then be used to modify the ligand design to enhance the catalytic properties.

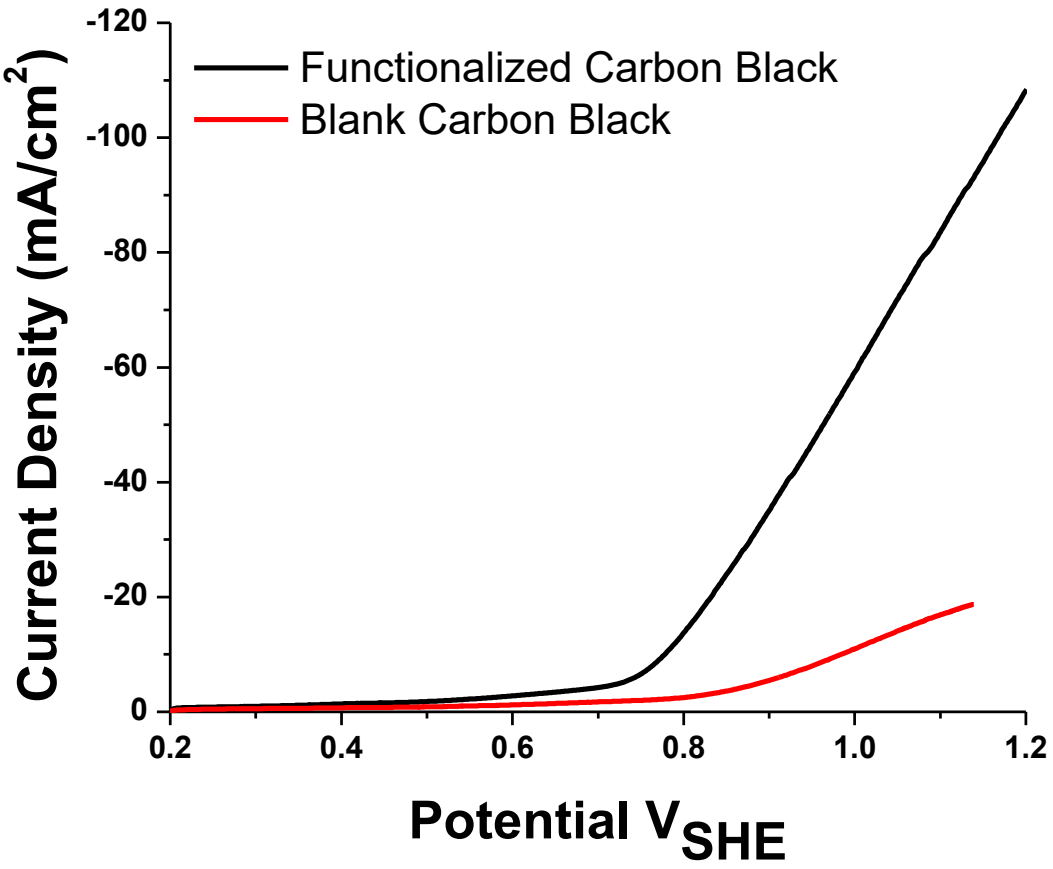

Figure 5.6. Polarization curves for **1@CB** and the blank CB in a 1 mol/L KOH solution pH 14 (RDE glassy carbon 1600 rpm (WE), Ag/AgCl (RE), Pt wire (AE)).

To evaluate the catalytic activity of **1@CB**, we performed a bulk electrolysis experiment to determine the turnover number and Faradaic efficiency using a custom-built H-type electrocatalytic cell. The ink was deposited onto a carbon cloth working electrode which was then used during catalysis. Following 2 h of electrolysis at an applied potential of 0.7 $V_{Ag/AgCl}$ (overpotential = 0.49 V), the assembly underwent 5400 turnovers, well above other molecular catalysts in solution.[144, 170-172] This corresponds to an observed turnover frequency of 2700 h^{-1}. **Figure 5.7** shows the plot of current *vs.* time. The slight decrease in current observed during catalysis suggests that the catalyst is undergoing a slow deactivation process in which the cobalt is possibly leaching out of the electrode. Based on the recently published behavior of the

analogous unsubstituted $[Co^{III}(L)(pyrr)_2]PF_6$ towards water reduction,[60] this deactivation is likely due to the formation of a ligand-based radical during the catalytic cycle.[173] Indeed ICP-MS analysis of the post catalytic solution reveals the presence of 4 ppb of cobalt ion, against trace amounts below the detection limit for the blank.

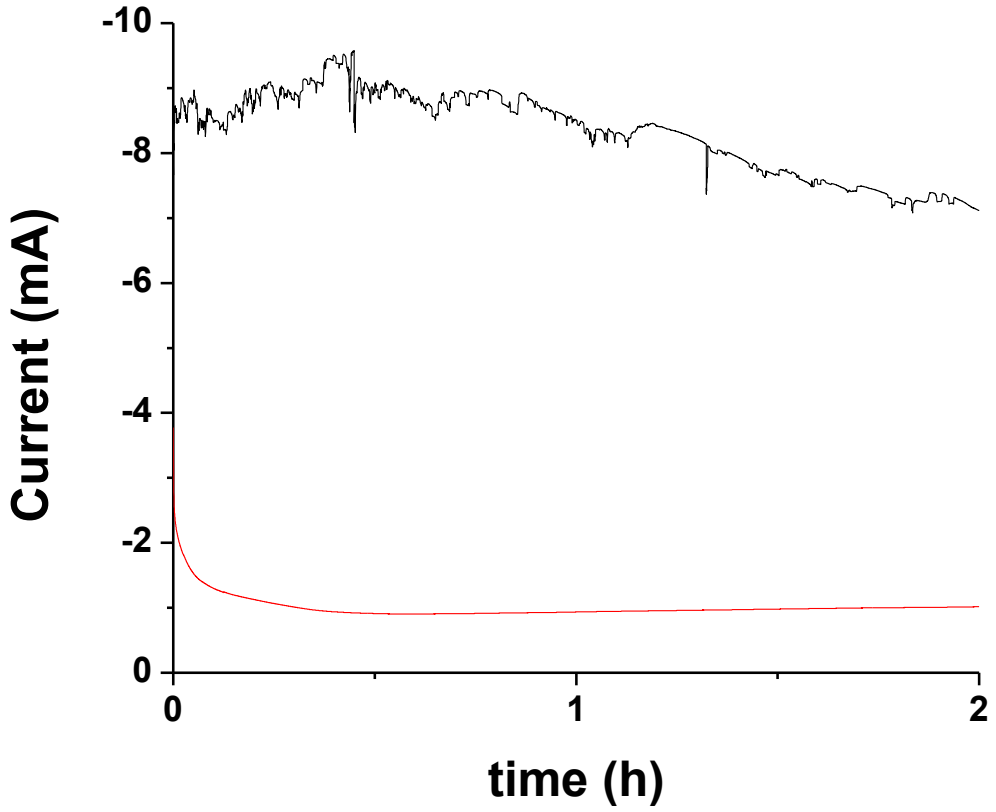

Figure 5.7. Plot of current versus time, both under an applied potential of 0.7 V for a two-hour catalytic run. **1@CB** (black), **CB** (red).

We also performed XPS analysis on **1@CB** to assess whether the surface immobilized molecules of **1** rearrange into CoO_x-based nanoparticulates. The results shown in **Figure 5.8.** reveal that the Co $2p_{3/2}$ and Co $2p_{1/2}$ energy peaks, respectively at 781 and 796 eV, remain unchanged before and after catalysis.

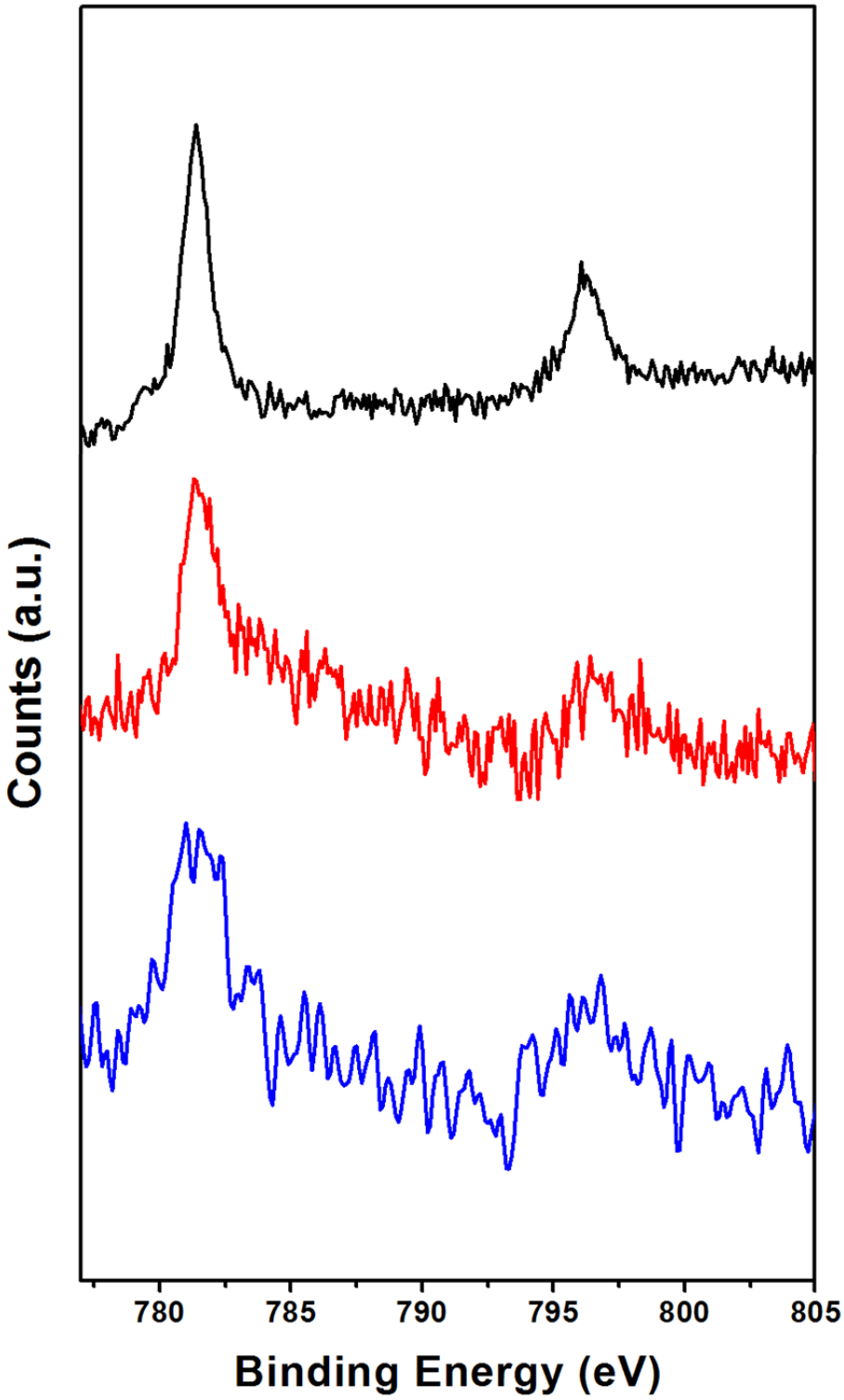

Figure 5.8. XPS spectra obtained for 1 (black), **1@CB** before catalysis (red), and after catalysis (blue).

In general O-O bond formation can occur *via* two possible pathways in the water oxidation mechanism. In the first pathway two Co=O species combines to form a μ-peroxo bridging intermediate (Co-O-O-Co). This mechanism is unlikely here because 1 is anchored onto CB with limited surface mobility. We therefore propose a second pathway in which a nucleophilic attack by an OH^- onto the Co=O species takes place. This possibility was evaluated using DFT calculations on a truncated analogue where $-OCH_3$ replaces $–OC_{18}H_{37}$, and our results suggest that catalysis is initiated by the substitution of one pyrrolidine by a hydroxide ion yielding $[Co^{III}(L^{OCH3})(pyr)(OH)]^0$ (**Figure 5.9.**). This transformation is favored by 7.4 kcal/mol. The catalytic cycle ensues with $[Co^{III}(L^{OCH3})(pyr)(OH)]^0$ undergoing a $1e^-$ oxidation to yield the ligand-oxidized $[Co^{III}(L^{OCH3\bullet})(pyr)(OH)]^+$ at a potential of 0.34 V_{SHE}. Following this step a proton coupled electron transfer takes place to form the formally $[Co^{IV}=O]$ containing species $[Co^{IV}(L^{OCH3\bullet})(pyr)(oxo)]^+$ at 0.97 V_{SHE}. It is important to note that the unpaired electron on the $[Co^{IV}]$ is significantly delocalized over the oxo moiety. Then an isothermal transformation (ΔG = 1.5 kcal/mol) in which a nucleophilic attach by an OH^- onto the Co=O oxo-species takes place to form the diamagnetic hydroperoxo species $[Co^{III}(L^{OCH3})(pyr)(OOH)]^0$. $[Co^{III}(L^{OCH3})(pyr)(OOH)]^0$ undergoes a $1e^-$ oxidation at 0.32 V_{SHE} to yield $[Co^{III}(L^{OCH3\bullet})(pyr)(OOH)]^0$ which is deprotonated into a superoxide species $[Co^{III}(L^{OCH3})(pyr)(OO^\bullet)]^+$ (ΔG = -19.8 kcal/mol). Following a further $1e^-$ oxidation to form $[Co^{III}(L^{OCH3\bullet})(pyr)(OO^\bullet)]^+$ at 0.35 V_{SHE} a nucleophilic attack by OH^- takes place to release O_2 and regenerate $[Co^{III}(L^{OCH3})(pyr)(OH)]^0$. It is interesting to note that throughout our transformations the oxidation state of the metal remains largely unchanged at $[Co^{III}]$ while the ligand acts as the site were oxidizing equivalents are stored. This is in contrast to most other

reported mechanisms which assume pure metal oxidation or highly limited ligand involvement.[147, 174-179]

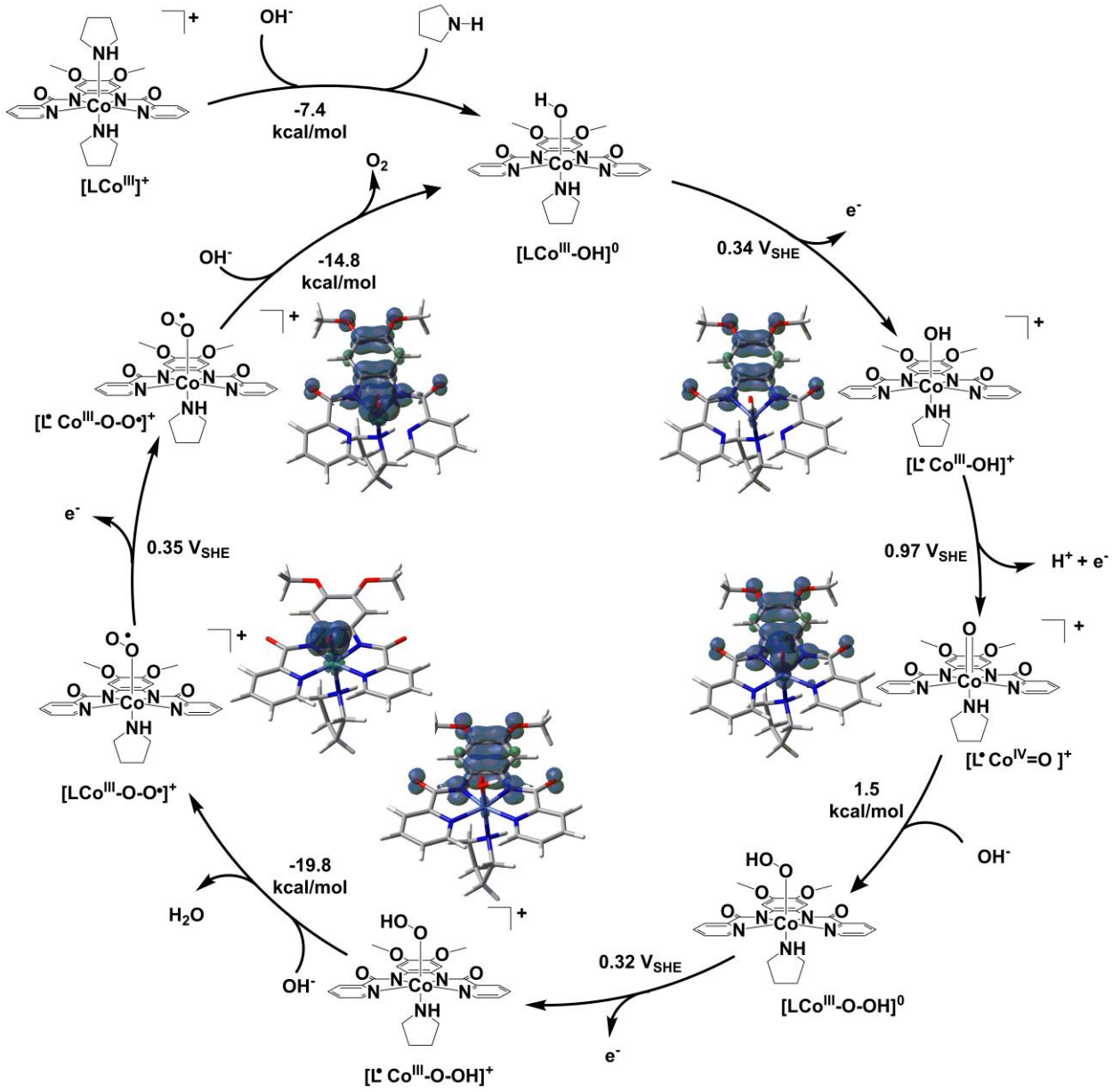

Figure 5.9. Proposed water oxidation mechanism of $[Co^{III}(L^{OCH3})(pyrr)_2]^+$. Spin density plots are shown next to the paramagnetic species (isovalue = 0.04 au).

6.4. Conclusions

In conclusion, we have reported on a novel alkoxy substituted cobalt complex that can be anchored onto carbon black. The resulting **1@CB** assembly, suspended in ink form, catalytically oxidizes water under basic conditions with an affordable onset overpotential of 0.32 V. The assembly reaches the required current density of 10 mA/cm^2 needed for solar cell development at an overpotential of just 0.37 V, while retaining its molecular nature. The affordable potentials are associated with ligand oxidation, thus acting as an electron reservoir that lowers the activation barrier needed for catalysis. This involvement, however, leads to catalyst deactivation by demetallation because of an unfavorable equilibrium involving $[M^{n-1}L^{\bullet}]^{+} \leftrightharpoons [M^{n}L]^{+}$. As such, while observed turnover numbers reached notable values above 5000 for molecular catalysts, improvements in design will be necessary to allow for the formation of high-valence cobalt species expected to enhance the stability of the catalyst.

CHAPTER 6. CONCLUSIONS AND PERSPECTIVES

The development of robust and efficient water splitting catalysts remains an important hurdle that needs to be overcome before the widespread adoption of hydrogen-based technologies can be achieved. Much of the literature has focused on the development of catalysts that are capable of driving these reactions as well as studying their underlying reaction mechanisms. While the importance of such studies cannot be understated, understanding the deactivation mechanism of said catalysts is equally important. However, such studies are largely lacking in the literature. In this dissertation, all of these broad topics, including catalytic deactivation, are covered and discussed in detail using the complexes shown in **Figure 6.1.**

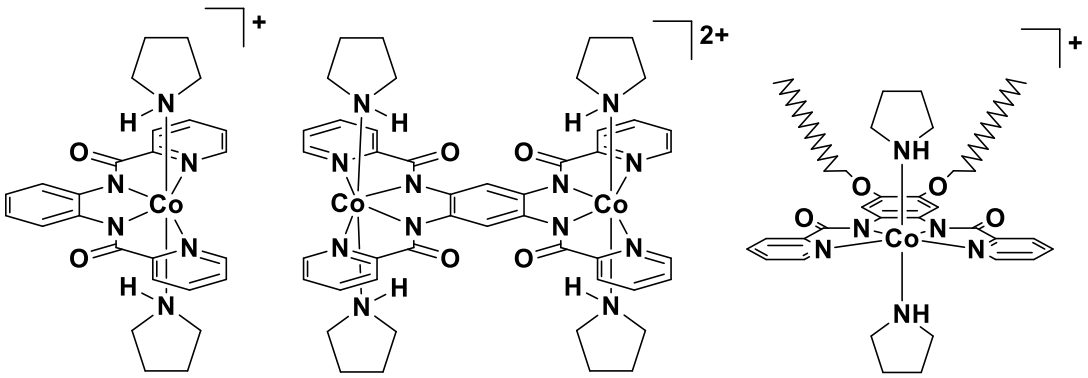

Figure 6.1. The catalysts that are studied in this thesis.

Based on our previous observation regarding the enhanced catalytic behavior obtained using a pentadentate amidopyridine ligand, in **Chapter 3** we designed a modified tetradentate ligand that incorporates two amidopyridine moieties. We then showed that the cobalt complex based on this ligand (**1**) can catalyze the reduction of water to hydrogen at an onset overpotential of 0.54 V. Moreover, we were able to obtain an impressive TOF of 23 min^{-1}. However, we observed a marked drop in charge consumption following a relatively short amount of time. This peculiar behavior prompted us to study the deactivation mechanism. Following a structural,

electrochemical, and spectroscopic study, we concluded that the active form of the catalyst is the nucleophilic [Co^{I}] oxidation state. [Co^{I}] reacts with protons to form [Co^{III}-H^{-}], a key intermediate in the proton reduction mechanism. However, we found evidence which showed that the metal-reduced [Co^{I}] is in tautomeric equilibrium with the ligand-reduced [Co^{II}-$L^{\bullet}$]. DFT calculations showed that, unlike [Co^{I}] which formed a [Co^{III}-H^{-}] upon protonation, [Co^{II}-$L^{\bullet}$] underwent ligand protonation to form a [Co^{II}-LH]. The protonated [Co^{II}-LH] is highly distorted from the original square planar geometry. We therefore concluded that catalyst deactivation takes place due to side reactions that lead to demetallation following ligand protonation.

In **Chapter 4**, we showed that using a bimetallic catalyst **2** in which a tetraamidobenzene was used to bridge the two cobalt centers can enhance the catalytic activity observed for the monometallic catalyst **1** described in **Chapter 3**. This is one of the first instances in which a bimetallic catalyst is demonstrably more active than its monometallic counterpart. While **1** had an observed TOF of 23 min^{-1}, **2**, under identical catalytic conditions, had an observed TOF of 60 min^{-1}. Moreover, **2** operated at an overpotential that is 0.1 V more positive than **1**. Given that **2** operates in a potential range where **1** is not catalytically active, we tested the catalytic performance of **2** in this region. Surprisingly, we observed that there was a marked improvement in stability in this catalytic region since we were able to observe catalysis even after 20 hours of electrolysis. This observation coupled with electrochemical, spectroscopic, and structural studies lead us to conclude that although **1** and **2** have very similar ligand designs, **2** operates using a voltage-dependent mechanism in which at low applied potentials a possible PCET mechanism avoiding [Co^{I}] is favored. On the other hand, at more negative applied potentials, the mechanism proceeds through [Co^{I}] as the active species. This in turn allows for the tautomeric equilibrium

we observed for **1** to take place, after which a similar deactivation mechanism is presumed to be at play.

We envision that further improvements to the amidopyridine platform can be achieved using two different pathways: (i) changing the metal center, and (ii) using the substituent effect to modulate catalytic behavior (**Figure 6.2.**). Changing the metal from cobalt (a 3d transition metal) to 4d or 5d transition metals such ruthenium or iridium respectively would impart greater ligand field stabilization on the metal complex. This increase in the ligand field stabilization energy would in turn make the metal ion less labile, thus disfavoring the demetallation of the catalyst and increasing the catalytic stability. However, such changes would likely make the metal-hydride more stable and less likely to react further to produce hydrogen. As such, another approach that relies on changing the substituents around the cobalt center could be utilized to tune the electronic properties of the ligand itself. Proposed substituents consist of electron donating groups, such as dimethylamine of methoxy moieties. We expect that such a substitution would shift the tautomeric equilibrium between $[Co^{I}\text{-}L] \leftrightarrow [Co^{II}\text{-}L^{\bullet}]$ towards the metal-centered reduced species and away from the ligand-centered reduced species. This shift in the equilibrium is expected to disfavor ligand protonation and to favor metal protonation which would lead to the formation of the desired $[Co^{III}\text{-}H^{-}]$ intermediate.

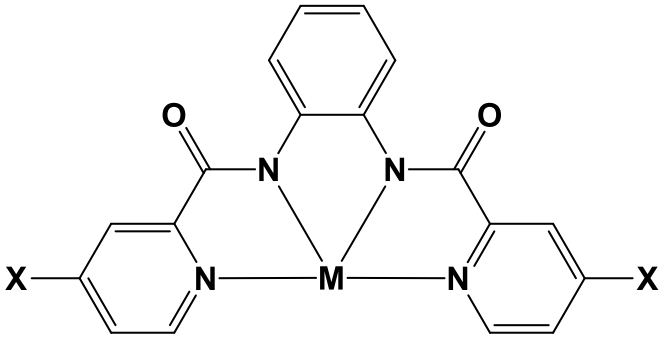

M = Co, Ru, or Ir
X = NMe_3, or OCH_3

Figure 6.2. The proposed modifications to **1**.

Given the ability of **1** to stabilize nominally high oxidation states, in **Chapter 5** we explored the other side of the water splitting reaction, namely water oxidation. In order to achieve this we prepared the amphiphilic molecular catalyst, $[Co^{III}(L^{OC18})(pyrr)_2]ClO_4$ (**3**) where L^{OC18} is the deprotonated form of N,N'-(4,5-bis(octadecyloxy)-1,2-phenylene)dipicolinamide. We showed that **3** can be anchored onto carbon black (CB) to yield the assembly **3@CB**. **3@CB** can catalyze water oxidation at an affordable onset overpotential of 0.32 V and reach a current density of 10 mA/cm^2 at an overpotential of 0.37 V, placing it on par with many nanostructured materials. Moreover, during bulk electrolysis **3@CB** displays TOF = 2700 h^{-1}. While XPS analysis confirmed the molecular nature of the catalyst, during electrolysis we observed a slight decrease in current consumption. This decrease in current was associated with demetallation of the **3@CB** assembly. Using DFT calculations, we proposed a mechanism for water oxidation. Our mechanism revealed that for most of the catalytic cycle, the ligand is acting as an electron reservoir for the oxidizing equivalents needed to oxidize water. This observation suggests that the high-valent oxo species that have been proposed in other studies can be made more energetically accessible by incorporating redox active ligands.

Future efforts will focus on enhancing the catalytic performance of **3** by focusing on two aspects of the catalyst design (**Figure 6.3**). The first aspect is attempting to use different metals such as ruthenium and iridium in an effort to impart greater stability on assembly (*vide supra*). Another important avenue for improving performance lies in the modification of the anchoring group. The anchoring group used in **3** is an octadecyloxy alkyl chain. Although this group is sufficient to attach **3** to the surface of CB, we hypothesize that using a shorter alkyl chain such octyloxy substituents would decrease the steric bulk of **3** which would allow us to anchor a greater number of molecules on the surface. Moreover, given the intrinsic lack of conductivity that can be achieved using alkyl-based anchoring groups, it is conceivable that using a shorter alkyl chain would also increase the conductivity of the assembly on carbon black. We also envision replacing the alkoxy substituents with highly conjugated anchoring groups such as pyrenes. This substitution would allow us to replace carbon black with even more conductive carbon-based substrates such as carbon nanotubes. A noncovalent bond would be achieved between the molecule and the substrate using π-π interactions. In fact, this anchoring mode is also expected to provide an avenue for electron transfer between the substrate (carbon nanotubes) and the anchored molecules.

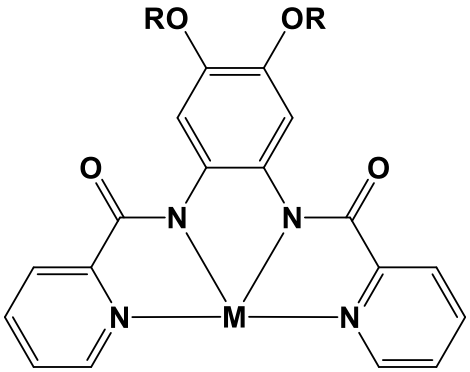

M = Co, Ru, or Ir
R = Pyrene, or C_8H_{17}

Figure 6.3. The proposed modifications to **3**

APPENDIX A. PERMISSION/LICENSE AGREEMENTS FOR COPYRIGHTED MATERIALS

Permission for: *Chem. Sci.* **2016**, *7, 3264* Copyright 2016, The Royal Society of Chemistry

The Royal Society of Chemistry does not require authors to obtain official permission to reproduce published papers in their own dissertation as long as proper acknowledgment is given.

Permission for: *Chem. Comun.* **2016**, *52, 8440* Copyright 2016, The Royal Society of Chemistry

The Royal Society of Chemistry does not require authors to obtain official permission to reproduce published papers in their own dissertation as long as proper acknowledgment is given.

Permission for: *Angew. Chem. Intl. Ed.* **2015**, *54, 2105* Copyright 2015, Wiley Publications

This Agreement between Mr. Habib Baydoun ("You") and John Wiley and Sons ("John Wiley and Sons") consists of your license details and the terms and conditions provided by John Wiley and Sons and Copyright Clearance Center.

License Number	4120421233436
License date	Jun 01, 2017
Licensed Content Publisher	John Wiley and Sons
Licensed Content Publication	Angewandte Chemie International Edition
Licensed Content Title	Ligand Transformations and Efficient Proton/Water Reduction with Cobalt Catalysts Based on Pentadentate Pyridine-Rich Environments
Licensed Content Author	Debashis Basu,Shivnath Mazumder,Xuetao Shi,Habib Baydoun,Jens Niklas,Oleg Poluektov,H. Bernhard Schlegel,Cláudio N. Verani
Licensed Content Date	Dec 22, 2014
Licensed Content Pages	6
Type of use	Dissertation/Thesis
Requestor type	Author of this Wiley article
Format	Print and electronic
Portion	Full article
Will you be translating?	No
Title of your thesis / dissertation	Water splitting using cobalt-based amidopyridine ligands
Expected completion date	Aug 2017
Expected size (number of pages)	200
Requestor Location	Mr. Habib Baydoun 5101 Cass Ave DETROIT, MI 48202 United States Attn: Mr. Habib Baydoun
Publisher Tax ID	EU826007151
Billing Type	Invoice
Billing Address	Mr. Habib Baydoun

5101 Cass Ave

DETROIT, MI 48202
United States
Attn: Mr. Habib Baydoun

Total 0.00 USD

Terms and Conditions

TERMS AND CONDITIONS

This copyrighted material is owned by or exclusively licensed to John Wiley & Sons, Inc. or one of its group companies (each a"Wiley Company") or handled on behalf of a society with which a Wiley Company has exclusive publishing rights in relation to a particular work (collectively "WILEY"). By clicking "accept" in connection with completing this licensing transaction, you agree that the following terms and conditions apply to this transaction (along with the billing and payment terms and conditions established by the Copyright Clearance Center Inc., ("CCC's Billing and Payment terms and conditions"), at the time that you opened your RightsLink account (these are available at any time at http://myaccount.copyright.com).

Terms and Conditions

- The materials you have requested permission to reproduce or reuse (the "Wiley Materials") are protected by copyright.

- You are hereby granted a personal, non-exclusive, non-sub licensable (on a stand-alone basis), non-transferable, worldwide, limited license to reproduce the Wiley Materials for the purpose specified in the licensing process. This license, **and any CONTENT (PDF or image file) purchased as part of your order,** is for a one-time use only and limited to any maximum distribution number specified in the license. The first instance of republication or reuse granted by this license must be completed within two years of the date of the grant of this license (although copies prepared before the end date may be distributed thereafter). The Wiley Materials shall not be used in any other manner or for any other purpose, beyond what is granted in the license. Permission is granted subject to an appropriate acknowledgement given to the author, title of the material/book/journal and the publisher. You shall also duplicate the copyright notice that appears in the Wiley publication in your use of the Wiley Material. Permission is also granted on the understanding that nowhere in the text is a previously published source acknowledged for all or part of this Wiley Material. Any third party content is expressly excluded from this permission.

- With respect to the Wiley Materials, all rights are reserved. Except as expressly granted by the terms of the license, no part of the Wiley Materials may be copied, modified, adapted (except for minor reformatting required by the new Publication), translated, reproduced, transferred or distributed, in any form or by any means, and

no derivative works may be made based on the Wiley Materials without the prior permission of the respective copyright owner.**For STM Signatory Publishers clearing permission under the terms of the STM Permissions Guidelines only, the terms of the license are extended to include subsequent editions and for editions in other languages, provided such editions are for the work as a whole in situ and does not involve the separate exploitation of the permitted figures or extracts,**You may not alter, remove or suppress in any manner any copyright, trademark or other notices displayed by the Wiley Materials. You may not license, rent, sell, loan, lease, pledge, offer as security, transfer or assign the Wiley Materials on a stand-alone basis, or any of the rights granted to you hereunder to any other person.

- The Wiley Materials and all of the intellectual property rights therein shall at all times remain the exclusive property of John Wiley & Sons Inc, the Wiley Companies, or their respective licensors, and your interest therein is only that of having possession of and the right to reproduce the Wiley Materials pursuant to Section 2 herein during the continuance of this Agreement. You agree that you own no right, title or interest in or to the Wiley Materials or any of the intellectual property rights therein. You shall have no rights hereunder other than the license as provided for above in Section 2. No right, license or interest to any trademark, trade name, service mark or other branding ("Marks") of WILEY or its licensors is granted hereunder, and you agree that you shall not assert any such right, license or interest with respect thereto

- NEITHER WILEY NOR ITS LICENSORS MAKES ANY WARRANTY OR REPRESENTATION OF ANY KIND TO YOU OR ANY THIRD PARTY, EXPRESS, IMPLIED OR STATUTORY, WITH RESPECT TO THE MATERIALS OR THE ACCURACY OF ANY INFORMATION CONTAINED IN THE MATERIALS, INCLUDING, WITHOUT LIMITATION, ANY IMPLIED WARRANTY OF MERCHANTABILITY, ACCURACY, SATISFACTORY QUALITY, FITNESS FOR A PARTICULAR PURPOSE, USABILITY, INTEGRATION OR NON-INFRINGEMENT AND ALL SUCH WARRANTIES ARE HEREBY EXCLUDED BY WILEY AND ITS LICENSORS AND WAIVED BY YOU.

- WILEY shall have the right to terminate this Agreement immediately upon breach of this Agreement by you.

- You shall indemnify, defend and hold harmless WILEY, its Licensors and their respective directors, officers, agents and employees, from and against any actual or threatened claims, demands, causes of action or proceedings arising from any breach of this Agreement by you.

- IN NO EVENT SHALL WILEY OR ITS LICENSORS BE LIABLE TO YOU OR ANY OTHER PARTY OR ANY OTHER PERSON OR ENTITY FOR ANY SPECIAL, CONSEQUENTIAL, INCIDENTAL, INDIRECT, EXEMPLARY OR PUNITIVE DAMAGES, HOWEVER CAUSED, ARISING OUT OF OR IN

CONNECTION WITH THE DOWNLOADING, PROVISIONING, VIEWING OR USE OF THE MATERIALS REGARDLESS OF THE FORM OF ACTION, WHETHER FOR BREACH OF CONTRACT, BREACH OF WARRANTY, TORT, NEGLIGENCE, INFRINGEMENT OR OTHERWISE (INCLUDING, WITHOUT LIMITATION, DAMAGES BASED ON LOSS OF PROFITS, DATA, FILES, USE, BUSINESS OPPORTUNITY OR CLAIMS OF THIRD PARTIES), AND WHETHER OR NOT THE PARTY HAS BEEN ADVISED OF THE POSSIBILITY OF SUCH DAMAGES. THIS LIMITATION SHALL APPLY NOTWITHSTANDING ANY FAILURE OF ESSENTIAL PURPOSE OF ANY LIMITED REMEDY PROVIDED HEREIN.

- Should any provision of this Agreement be held by a court of competent jurisdiction to be illegal, invalid, or unenforceable, that provision shall be deemed amended to achieve as nearly as possible the same economic effect as the original provision, and the legality, validity and enforceability of the remaining provisions of this Agreement shall not be affected or impaired thereby.

- The failure of either party to enforce any term or condition of this Agreement shall not constitute a waiver of either party's right to enforce each and every term and condition of this Agreement. No breach under this agreement shall be deemed waived or excused by either party unless such waiver or consent is in writing signed by the party granting such waiver or consent. The waiver by or consent of a party to a breach of any provision of this Agreement shall not operate or be construed as a waiver of or consent to any other or subsequent breach by such other party.

- This Agreement may not be assigned (including by operation of law or otherwise) by you without WILEY's prior written consent.

- Any fee required for this permission shall be non-refundable after thirty (30) days from receipt by the CCC.

- These terms and conditions together with CCC's Billing and Payment terms and conditions (which are incorporated herein) form the entire agreement between you and WILEY concerning this licensing transaction and (in the absence of fraud) supersedes all prior agreements and representations of the parties, oral or written. This Agreement may not be amended except in writing signed by both parties. This Agreement shall be binding upon and inure to the benefit of the parties' successors, legal representatives, and authorized assigns.

- In the event of any conflict between your obligations established by these terms and conditions and those established by CCC's Billing and Payment terms and conditions, these terms and conditions shall prevail.

- WILEY expressly reserves all rights not specifically granted in the combination of (i) the license details provided by you and accepted in the course of this licensing transaction, (ii) these terms and conditions and (iii) CCC's Billing and Payment

terms and conditions.

- This Agreement will be void if the Type of Use, Format, Circulation, or Requestor Type was misrepresented during the licensing process.

- This Agreement shall be governed by and construed in accordance with the laws of the State of New York, USA, without regards to such state's conflict of law rules. Any legal action, suit or proceeding arising out of or relating to these Terms and Conditions or the breach thereof shall be instituted in a court of competent jurisdiction in New York County in the State of New York in the United States of America and each party hereby consents and submits to the personal jurisdiction of such court, waives any objection to venue in such court and consents to service of process by registered or certified mail, return receipt requested, at the last known address of such party.

WILEY OPEN ACCESS TERMS AND CONDITIONS

Wiley Publishes Open Access Articles in fully Open Access Journals and in Subscription journals offering Online Open. Although most of the fully Open Access journals publish open access articles under the terms of the Creative Commons Attribution (CC BY) License only, the subscription journals and a few of the Open Access Journals offer a choice of Creative Commons Licenses. The license type is clearly identified on the article.

The Creative Commons Attribution License

The Creative Commons Attribution License (CC-BY) allows users to copy, distribute and transmit an article, adapt the article and make commercial use of the article. The CC-BY license permits commercial and non-

Creative Commons Attribution Non-Commercial License

The Creative Commons Attribution Non-Commercial (CC-BY-NC)License permits use, distribution and reproduction in any medium, provided the original work is properly cited and is not used for commercial purposes.(see below)

Creative Commons Attribution-Non-Commercial-NoDerivs License

The Creative Commons Attribution Non-Commercial-NoDerivs License (CC-BY-NC-ND) permits use, distribution and reproduction in any medium, provided the original work is properly cited, is not used for commercial purposes and no modifications or adaptations are made. (see below)

Use by commercial "for-profit" organizations

Use of Wiley Open Access articles for commercial, promotional, or marketing purposes requires further explicit permission from Wiley and will be subject to a fee.

Further details can be found on Wiley Online Library http://olabout.wiley.com/WileyCDA/Section/id-410895.html

Permission for: *Chem. Eur. J.* **2017**, *23*, 9266 Copyright 2017, Wiley Publication

This Agreement between Mr. Habib Baydoun ("You") and John Wiley and Sons ("John Wiley and Sons") consists of your license details and the terms and conditions provided by John Wiley and Sons and Copyright Clearance Center.

License Number	4114391078362
License date	May 22, 2017
Licensed Content Publisher	John Wiley and Sons
Licensed Content Publication	Chemistry - A European Journal
Licensed Content Title	Deactivation of a Cobalt Catalyst for Water Reduction through Valence Tautomerism
Licensed Content Author	Habib Baydoun,Shivnath Mazumder,H. Bernhard Schlegel,Cláudio N. Verani
Licensed Content Date	May 22, 2017
Licensed Content Pages	1
Type of use	Dissertation/Thesis
Requestor type	Author of this Wiley article
Format	Print and electronic
Portion	Full article
Will you be translating?	No
Title of your thesis / dissertation	Water splitting using cobalt-based amidopyridine ligands
Expected completion date	Aug 2017
Expected size (number of pages)	200
Requestor Location	Mr. Habib Baydoun 5101 Cass Ave DETROIT, MI 48202 United States Attn: Mr. Habib Baydoun
Publisher Tax ID	EU826007151
Billing Type	Invoice
Billing Address	Mr. Habib Baydoun 5101 Cass Ave

DETROIT, MI 48202
United States
Attn: Mr. Habib Baydoun

Total 0.00 USD

Terms and Conditions

TERMS AND CONDITIONS

This copyrighted material is owned by or exclusively licensed to John Wiley & Sons, Inc. or one of its group companies (each a"Wiley Company") or handled on behalf of a society with which a Wiley Company has exclusive publishing rights in relation to a particular work (collectively "WILEY"). By clicking "accept" in connection with completing this licensing transaction, you agree that the following terms and conditions apply to this transaction (along with the billing and payment terms and conditions established by the Copyright Clearance Center Inc., ("CCC's Billing and Payment terms and conditions"), at the time that you opened your RightsLink account (these are available at any time at http://myaccount.copyright.com).

Terms and Conditions

- The materials you have requested permission to reproduce or reuse (the "Wiley Materials") are protected by copyright.

- You are hereby granted a personal, non-exclusive, non-sub licensable (on a stand-alone basis), non-transferable, worldwide, limited license to reproduce the Wiley Materials for the purpose specified in the licensing process. This license, **and any CONTENT (PDF or image file) purchased as part of your order,** is for a one-time use only and limited to any maximum distribution number specified in the license. The first instance of republication or reuse granted by this license must be completed within two years of the date of the grant of this license (although copies prepared before the end date may be distributed thereafter). The Wiley Materials shall not be used in any other manner or for any other purpose, beyond what is granted in the license. Permission is granted subject to an appropriate acknowledgement given to the author, title of the material/book/journal and the publisher. You shall also duplicate the copyright notice that appears in the Wiley publication in your use of the Wiley Material. Permission is also granted on the understanding that nowhere in the text is a previously published source acknowledged for all or part of this Wiley Material. Any third party content is expressly excluded from this permission.

- With respect to the Wiley Materials, all rights are reserved. Except as expressly granted by the terms of the license, no part of the Wiley Materials may be copied, modified, adapted (except for minor reformatting required by the new Publication), translated, reproduced, transferred or distributed, in any form or by any means, and no derivative works may be made based on the Wiley Materials without the prior

permission of the respective copyright owner.**For STM Signatory Publishers clearing permission under the terms of the STM Permissions Guidelines only, the terms of the license are extended to include subsequent editions and for editions in other languages, provided such editions are for the work as a whole in situ and does not involve the separate exploitation of the permitted figures or extracts,**You may not alter, remove or suppress in any manner any copyright, trademark or other notices displayed by the Wiley Materials. You may not license, rent, sell, loan, lease, pledge, offer as security, transfer or assign the Wiley Materials on a stand-alone basis, or any of the rights granted to you hereunder to any other person.

- The Wiley Materials and all of the intellectual property rights therein shall at all times remain the exclusive property of John Wiley & Sons Inc, the Wiley Companies, or their respective licensors, and your interest therein is only that of having possession of and the right to reproduce the Wiley Materials pursuant to Section 2 herein during the continuance of this Agreement. You agree that you own no right, title or interest in or to the Wiley Materials or any of the intellectual property rights therein. You shall have no rights hereunder other than the license as provided for above in Section 2. No right, license or interest to any trademark, trade name, service mark or other branding ("Marks") of WILEY or its licensors is granted hereunder, and you agree that you shall not assert any such right, license or interest with respect thereto

- NEITHER WILEY NOR ITS LICENSORS MAKES ANY WARRANTY OR REPRESENTATION OF ANY KIND TO YOU OR ANY THIRD PARTY, EXPRESS, IMPLIED OR STATUTORY, WITH RESPECT TO THE MATERIALS OR THE ACCURACY OF ANY INFORMATION CONTAINED IN THE MATERIALS, INCLUDING, WITHOUT LIMITATION, ANY IMPLIED WARRANTY OF MERCHANTABILITY, ACCURACY, SATISFACTORY QUALITY, FITNESS FOR A PARTICULAR PURPOSE, USABILITY, INTEGRATION OR NON-INFRINGEMENT AND ALL SUCH WARRANTIES ARE HEREBY EXCLUDED BY WILEY AND ITS LICENSORS AND WAIVED BY YOU.

- WILEY shall have the right to terminate this Agreement immediately upon breach of this Agreement by you.

- You shall indemnify, defend and hold harmless WILEY, its Licensors and their respective directors, officers, agents and employees, from and against any actual or threatened claims, demands, causes of action or proceedings arising from any breach of this Agreement by you.

- IN NO EVENT SHALL WILEY OR ITS LICENSORS BE LIABLE TO YOU OR ANY OTHER PARTY OR ANY OTHER PERSON OR ENTITY FOR ANY SPECIAL, CONSEQUENTIAL, INCIDENTAL, INDIRECT, EXEMPLARY OR PUNITIVE DAMAGES, HOWEVER CAUSED, ARISING OUT OF OR IN CONNECTION WITH THE DOWNLOADING, PROVISIONING, VIEWING

OR USE OF THE MATERIALS REGARDLESS OF THE FORM OF ACTION, WHETHER FOR BREACH OF CONTRACT, BREACH OF WARRANTY, TORT, NEGLIGENCE, INFRINGEMENT OR OTHERWISE (INCLUDING, WITHOUT LIMITATION, DAMAGES BASED ON LOSS OF PROFITS, DATA, FILES, USE, BUSINESS OPPORTUNITY OR CLAIMS OF THIRD PARTIES), AND WHETHER OR NOT THE PARTY HAS BEEN ADVISED OF THE POSSIBILITY OF SUCH DAMAGES. THIS LIMITATION SHALL APPLY NOTWITHSTANDING ANY FAILURE OF ESSENTIAL PURPOSE OF ANY LIMITED REMEDY PROVIDED HEREIN.

- Should any provision of this Agreement be held by a court of competent jurisdiction to be illegal, invalid, or unenforceable, that provision shall be deemed amended to achieve as nearly as possible the same economic effect as the original provision, and the legality, validity and enforceability of the remaining provisions of this Agreement shall not be affected or impaired thereby.

- The failure of either party to enforce any term or condition of this Agreement shall not constitute a waiver of either party's right to enforce each and every term and condition of this Agreement. No breach under this agreement shall be deemed waived or excused by either party unless such waiver or consent is in writing signed by the party granting such waiver or consent. The waiver by or consent of a party to a breach of any provision of this Agreement shall not operate or be construed as a waiver of or consent to any other or subsequent breach by such other party.

- This Agreement may not be assigned (including by operation of law or otherwise) by you without WILEY's prior written consent.

- Any fee required for this permission shall be non-refundable after thirty (30) days from receipt by the CCC.

- These terms and conditions together with CCC's Billing and Payment terms and conditions (which are incorporated herein) form the entire agreement between you and WILEY concerning this licensing transaction and (in the absence of fraud) supersedes all prior agreements and representations of the parties, oral or written. This Agreement may not be amended except in writing signed by both parties. This Agreement shall be binding upon and inure to the benefit of the parties' successors, legal representatives, and authorized assigns.

- In the event of any conflict between your obligations established by these terms and conditions and those established by CCC's Billing and Payment terms and conditions, these terms and conditions shall prevail.

- WILEY expressly reserves all rights not specifically granted in the combination of (i) the license details provided by you and accepted in the course of this licensing transaction, (ii) these terms and conditions and (iii) CCC's Billing and Payment

terms and conditions.

- This Agreement will be void if the Type of Use, Format, Circulation, or Requestor Type was misrepresented during the licensing process.

- This Agreement shall be governed by and construed in accordance with the laws of the State of New York, USA, without regards to such state's conflict of law rules. Any legal action, suit or proceeding arising out of or relating to these Terms and Conditions or the breach thereof shall be instituted in a court of competent jurisdiction in New York County in the State of New York in the United States of America and each party hereby consents and submits to the personal jurisdiction of such court, waives any objection to venue in such court and consents to service of process by registered or certified mail, return receipt requested, at the last known address of such party.

WILEY OPEN ACCESS TERMS AND CONDITIONS

Wiley Publishes Open Access Articles in fully Open Access Journals and in Subscription journals offering Online Open. Although most of the fully Open Access journals publish open access articles under the terms of the Creative Commons Attribution (CC BY) License only, the subscription journals and a few of the Open Access Journals offer a choice of Creative Commons Licenses. The license type is clearly identified on the article.

The Creative Commons Attribution License

The Creative Commons Attribution License (CC-BY) allows users to copy, distribute and transmit an article, adapt the article and make commercial use of the article. The CC-BY license permits commercial and non-

Creative Commons Attribution Non-Commercial License

The Creative Commons Attribution Non-Commercial (CC-BY-NC)License permits use, distribution and reproduction in any medium, provided the original work is properly cited and is not used for commercial purposes.(see below)

Creative Commons Attribution-Non-Commercial-NoDerivs License

The Creative Commons Attribution Non-Commercial-NoDerivs License (CC-BY-NC-ND) permits use, distribution and reproduction in any medium, provided the original work is properly cited, is not used for commercial purposes and no modifications or adaptations are made. (see below)

Use by commercial "for-profit" organizations

Use of Wiley Open Access articles for commercial, promotional, or marketing purposes requires further explicit permission from Wiley and will be subject to a fee.

Further details can be found on Wiley Online Library http://olabout.wiley.com/WileyCDA/Section/id-410895.html

APPENDIX B. CRYSTALLOGRAPHIC STRUCTURAL DETAILS FOR UNPUBLISHED STRUCTURES

Crystal structure for $[(Co^{III})_2L^2(pyrr)_4](ClO_4)_2$ presented in chapter 4.

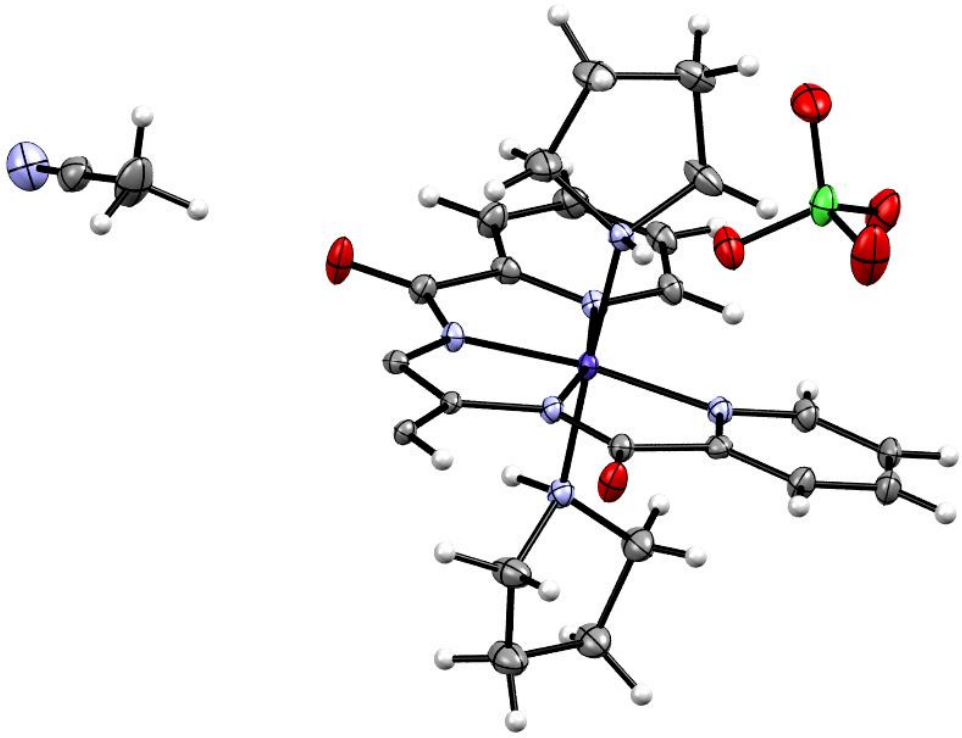

Table A1 Fractional Atomic Coordinates (×10^4) and Equivalent Isotropic Displacement Parameters (Å^2×10^3) for [(Co^{III})$_2$L^2(pyrr)$_4$](ClO$_4$)$_2$ U_{eq} is defined as 1/3 of of the trace of the orthogonalised U_{IJ} tensor.

Atom	*x*	*y*	*z*	U(eq)
Co1	3080.1(4)	10201.9(4)	2213.6(2)	11.40(11)
Cl1	7863.7(8)	12320.8(7)	4194.2(4)	22.83(17)
O2	5629(2)	13728.9(19)	1651.7(11)	22.1(4)
N5	1238(2)	10881(2)	1689.6(13)	15.1(5)
N6	4874(2)	9516(2)	2794.3(13)	14.3(5)
O1	2546(2)	6412(2)	723.6(12)	27.6(5)
O4	7311(2)	11955(2)	3329.8(12)	28.2(5)
O5	9002(2)	11324(2)	4378.6(13)	35.2(5)
O6	8484(3)	13812(2)	4294.3(14)	44.6(6)
O3	6655(2)	12145(2)	4773.8(13)	31.7(5)
N3	4386(2)	11407(2)	1599.5(13)	12.1(4)
N4	3204(2)	11957(2)	3064.4(13)	14.0(5)
C7	4758(3)	10776(3)	783.6(15)	11.4(5)
C8	5673(3)	11448(3)	198.9(15)	11.2(5)
C9	4092(3)	9339(3)	585.5(15)	11.7(5)
N2	3200(2)	8832(2)	1243.7(13)	12.5(5)
N1	1825(2)	8549(2)	2653.5(13)	13.3(5)
N7	1015(3)	1722(3)	-1202.5(17)	36.6(7)
C6	4814(3)	12772(3)	1950.5(16)	14.5(6)
C5	4127(3)	13058(3)	2804.1(16)	14.2(5)
C1	2503(3)	12229(3)	3805.5(16)	18.1(6)
C2	2686(3)	13552(3)	4298.1(17)	18.7(6)
C3	3656(3)	14660(3)	4039.8(17)	21.1(6)
C4	4386(3)	14399(3)	3284.5(17)	19.2(6)
C16	83(3)	11550(3)	2227.2(18)	24.7(7)
C17	-1103(3)	12003(3)	1613.6(18)	26.1(7)
C18	-296(3)	12133(4)	775.4(19)	30.1(7)
C19	1323(3)	11803(3)	968.2(18)	26.6(7)
C20	5686(3)	8319(3)	2374.2(19)	29.4(7)
C21	6915(3)	8046(3)	3005.7(19)	28.6(7)
C22	6218(3)	8379(3)	3879.8(18)	24.0(6)
C23	4806(3)	9171(4)	3697.3(18)	28.6(7)
C11	1774(3)	7327(3)	2096.7(16)	15.5(6)
C12	1059(3)	6008(3)	2270.8(18)	21.2(6)
C13	364(3)	5902(3)	3042.4(17)	21.1(6)
C14	406(3)	7148(3)	3612.9(17)	18.8(6)
C15	1133(3)	8444(3)	3398.5(16)	16.1(6)
C10	2549(3)	7472(3)	1270.3(16)	16.4(6)
C24	2895(4)	3870(3)	-635(2)	38.6(8)
C25	1834(3)	2684(3)	-953.5(19)	26.2(7)

Table A2 Anisotropic Displacement Parameters (Å^2×10^3) for Hb77-run1. The Anisotropic displacement factor exponent takes the form: -2π^2[h^{2}a*^{2}U$_{11}$+2hka*b*U$_{12}$+…].

Atom	U_{11}	U_{22}	U_{33}	U_{23}	U_{13}	U_{12}
Co1	11.83(18)	13.39(19)	8.97(18)	0.71(13)	3.40(13)	0.29(13)
Cl1	25.3(4)	24.5(4)	17.8(4)	-1.8(3)	8.1(3)	-2.0(3)
O2	29.9(11)	15(1)	20.5(11)	-0.4(8)	11.9(9)	-4.4(8)
N5	14.8(11)	16.6(11)	14.0(11)	1.3(9)	4.1(9)	1.8(9)
N6	15.7(11)	15.7(11)	11.6(11)	2.4(9)	1.3(9)	0.3(9)
O1	44.5(13)	16.8(10)	19.5(11)	-4.5(8)	14.3(9)	-8.2(9)
O4	27.0(11)	40.2(13)	16.4(11)	-2.5(9)	0.6(9)	0.7(9)
O5	26.5(12)	50.7(14)	29.3(12)	1.5(10)	-0.9(10)	14.2(10)
O6	66.4(17)	28.4(12)	35.6(13)	-3.6(10)	18.3(12)	-19.5(11)
O3	37.8(12)	29.5(11)	28.2(12)	1.2(9)	21.4(10)	1.9(10)
N3	12.4(11)	13.6(11)	10.5(11)	1.0(9)	3.7(9)	1.5(9)
N4	13.6(11)	16.4(11)	12.1(11)	0.9(9)	2.0(9)	1.5(9)
C7	12.1(12)	13.5(13)	9.2(12)	0.9(10)	1.3(10)	4.3(10)
C8	11.8(12)	9.4(12)	12.1(13)	0.1(10)	0.8(10)	-0.4(10)
C9	10.2(12)	13.9(13)	11.8(13)	4(1)	3.2(10)	2.8(10)
N2	11.9(11)	14.7(11)	10.7(11)	0.9(9)	3.9(9)	-0.6(9)

N1	10.2(11)	17.2(11)	12.2(11)	0.5(9)	1.0(9)	-0.6(9)
N7	33.9(16)	41.9(17)	32.8(16)	2.1(13)	1.8(13)	-4.3(14)
C6	14.5(13)	15.3(13)	13.7(13)	1.5(11)	1.6(11)	1.6(11)
C5	12.7(13)	16.5(13)	14.4(14)	2.7(11)	1.1(11)	4.9(10)
C1	19.2(14)	21.1(14)	14.2(14)	1.6(11)	6.2(11)	2.1(11)
C2	21.6(14)	22.9(14)	12.2(13)	0.1(11)	4.9(11)	6.7(12)
C3	27.1(16)	19.3(14)	16.4(14)	-2.9(11)	2.6(12)	2.9(12)
C4	22.4(15)	15.1(14)	19.5(15)	-1.1(11)	4.5(12)	0.3(11)
C16	20.4(15)	33.2(17)	21.3(16)	2.7(13)	4.1(12)	7.6(13)
C17	19.6(15)	36.7(18)	23.3(16)	4.3(13)	3.6(13)	7.9(13)
C18	24.4(16)	44.1(19)	24.3(17)	8.8(14)	2.6(13)	12.5(14)
C19	22.6(15)	37.6(18)	22.5(16)	12.6(14)	4.7(13)	10.1(13)
C20	26.4(17)	37.5(18)	25.5(17)	2.8(14)	-0.7(13)	13.2(14)
C21	20.8(15)	34.2(18)	32.1(18)	7.8(14)	-5.3(13)	7.0(13)
C22	23.1(15)	24.6(16)	24.7(16)	9.8(13)	-6.9(13)	-3.6(12)
C23	21.7(16)	48(2)	17.6(15)	13.0(14)	-1.3(13)	3.8(14)
C11	14.6(13)	17.7(14)	14.9(14)	5.3(11)	2.4(11)	0.2(11)
C12	25.3(15)	16.1(14)	21.9(15)	0.3(12)	5.7(12)	-0.3(12)
C13	21.4(15)	20.3(15)	22.7(15)	7.7(12)	6.2(12)	0.1(12)
C14	13.6(13)	29.9(16)	13.9(14)	7.8(12)	4.9(11)	1.4(12)
C15	14.9(13)	20.5(14)	12.8(14)	2.0(11)	2.2(11)	-0.3(11)
C10	19.3(14)	13.7(13)	16.1(14)	0.7(11)	4.0(11)	0.6(11)
C24	59(2)	18.4(16)	37(2)	-1.5(14)	13.5(17)	-6.5(16)
C25	30.3(17)	24.6(16)	24.6(17)	2.4(13)	7.4(14)	6.4(14)

Table A3 Bond Lengths for $[(Co^{III})_2L^2(pyrr)_4](ClO_4)_2$

Atom	Atom	Length/Å		Atom	Atom	Length/Å
Co1	N5	1.988(2)		C9	C8[1]	1.397(3)
Co1	N6	1.995(2)		C9	N2	1.412(3)
Co1	N3	1.890(2)		N2	C10	1.338(3)
Co1	N4	1.985(2)		N1	C11	1.350(3)
Co1	N2	1.891(2)		N1	C15	1.345(3)
Co1	N1	2.000(2)		N7	C25	1.143(4)
Cl1	O4	1.444(2)		C6	C5	1.496(3)
Cl1	O5	1.446(2)		C5	C4	1.380(3)
Cl1	O6	1.427(2)		C1	C2	1.370(4)
Cl1	O3	1.4384(19)		C2	C3	1.382(4)
O2	C6	1.232(3)		C3	C4	1.376(4)
N5	C16	1.473(3)		C16	C17	1.524(4)
N5	C19	1.470(3)		C17	C18	1.526(4)
N6	C20	1.461(3)		C18	C19	1.530(4)
N6	C23	1.485(3)		C20	C21	1.517(4)
O1	C10	1.233(3)		C21	C22	1.535(4)
N3	C7	1.413(3)		C22	C23	1.528(4)
N3	C6	1.342(3)		C11	C12	1.375(3)
N4	C5	1.354(3)		C11	C10	1.498(3)
N4	C1	1.345(3)		C12	C13	1.383(4)
C7	C8	1.399(3)		C13	C14	1.379(4)
C7	C9	1.408(3)		C14	C15	1.381(3)
C8	C9[1]	1.397(3)		C24	C25	1.442(4)

[1]1-X,2-Y,-Z

Table A4 Bond Angles for $[(Co^{III})_2L^2(pyrr)_4](ClO_4)_2$

Atom	Atom	Atom	Angle/°		Atom	Atom	Atom	Angle/°
N5	Co1	N6	177.12(8)		C8[1]	C9	C7	120.9(2)
N5	Co1	N1	88.53(8)		C8[1]	C9	N2	125.8(2)
N6	Co1	N1	89.62(8)		C9	N2	Co1	114.90(16)
N3	Co1	N5	94.06(9)		C10	N2	Co1	118.21(16)
N3	Co1	N6	88.25(9)		C10	N2	C9	126.7(2)
N3	Co1	N4	83.27(8)		C11	N1	Co1	110.95(16)
N3	Co1	N2	83.64(8)		C15	N1	Co1	131.49(17)
N3	Co1	N1	166.36(8)		C15	N1	C11	117.4(2)
N4	Co1	N5	90.97(9)		O2	C6	N3	128.4(2)
N4	Co1	N6	87.59(8)		O2	C6	C5	121.0(2)

N4	Co1	N1	110.10(8)		N3	C6	C5	110.6(2)
N2	Co1	N5	87.87(9)		N4	C5	C6	116.6(2)
N2	Co1	N6	94.09(9)		N4	C5	C4	122.0(2)
N2	Co1	N4	166.74(8)		C4	C5	C6	121.3(2)
N2	Co1	N1	83.08(8)		N4	C1	C2	123.1(2)
O4	Cl1	O5	109.04(12)		C1	C2	C3	119.2(2)
O6	Cl1	O4	110.00(13)		C4	C3	C2	118.5(2)
O6	Cl1	O5	109.68(14)		C3	C4	C5	119.7(2)
O6	Cl1	O3	109.72(12)		N5	C16	C17	105.9(2)
O3	Cl1	O4	109.40(13)		C16	C17	C18	104.8(2)
O3	Cl1	O5	108.99(13)		C17	C18	C19	105.0(2)
C16	N5	Co1	120.57(17)		N5	C19	C18	105.1(2)
C19	N5	Co1	120.96(17)		N6	C20	C21	105.1(2)
C19	N5	C16	103.5(2)		C20	C21	C22	104.1(2)
C20	N6	Co1	119.47(17)		C23	C22	C21	105.0(2)
C20	N6	C23	104.2(2)		N6	C23	C22	106.6(2)
C23	N6	Co1	120.29(16)		N1	C11	C12	122.5(2)
C7	N3	Co1	115.04(16)		N1	C11	C10	116.5(2)
C6	N3	Co1	118.34(16)		C12	C11	C10	121.0(2)
C6	N3	C7	126.6(2)		C11	C12	C13	119.8(3)
C5	N4	Co1	111.15(16)		C14	C13	C12	118.0(2)
C1	N4	Co1	131.36(17)		C13	C14	C15	119.4(2)
C1	N4	C5	117.4(2)		N1	C15	C14	122.8(2)
C8	C7	N3	126.2(2)		O1	C10	N2	128.2(2)
C8	C7	C9	120.7(2)		O1	C10	C11	120.7(2)
C9	C7	N3	113.1(2)		N2	C10	C11	111.1(2)
$C9^1$	C8	C7	118.4(2)		N7	C25	C24	178.5(3)
C7	C9	N2	113.3(2)					

Table A5 Torsion Angles for $[(Co^{III})_2L^2(pyrr)_4](ClO_4)_2$

A	B	C	D	Angle/°		A	B	C	D	Angle/°
Co1	N5	C16	C17	177.08(17)		C7	C9	N2	Co1	1.2(3)
Co1	N5	C19	C18	-177.98(18)		C7	C9	N2	C10	-173.2(2)
Co1	N6	C20	C21	-177.45(17)		C8	C7	C9	$C8^1$	0.0(4)
Co1	N6	C23	C22	168.18(17)		C8	C7	C9	N2	-179.7(2)
Co1	N3	C7	C8	178.61(19)		$C8^1$	C9	N2	Co1	-178.43(19)
Co1	N3	C7	C9	-0.8(3)		$C8^1$	C9	N2	C10	7.2(4)
Co1	N3	C6	O2	-178.6(2)		C9	C7	C8	$C9^1$	0.0(4)
Co1	N3	C6	C5	0.2(3)		C9	N2	C10	O1	-2.9(4)
Co1	N4	C5	C6	1.6(3)		C9	N2	C10	C11	176.4(2)
Co1	N4	C5	C4	179.5(2)		N2	Co1	N3	C7	1.19(17)
Co1	N4	C1	C2	-177.08(19)		N2	Co1	N3	C6	178.45(19)
Co1	N2	C10	O1	-177.1(2)		N1	Co1	N3	C7	14.4(5)
Co1	N2	C10	C11	2.1(3)		N1	Co1	N3	C6	-168.4(3)
Co1	N1	C11	C12	176.0(2)		N1	Co1	N2	C9	-178.23(18)
Co1	N1	C11	C10	-3.7(3)		N1	Co1	N2	C10	-3.32(19)
Co1	N1	C15	C14	-174.61(19)		N1	C11	C12	C13	-0.2(4)
O2	C6	C5	N4	177.7(2)		N1	C11	C10	O1	-179.4(2)
O2	C6	C5	C4	-0.2(4)		N1	C11	C10	N2	1.2(3)
N5	Co1	N3	C7	-86.21(17)		C6	N3	C7	C8	1.6(4)
N5	Co1	N3	C6	91.05(19)		C6	N3	C7	C9	-177.8(2)
N5	Co1	N2	C9	92.99(17)		C6	C5	C4	C3	175.6(2)
N5	Co1	N2	C10	-92.09(19)		C5	N4	C1	C2	-0.1(4)
N5	C16	C17	C18	-21.8(3)		C1	N4	C5	C6	-176.0(2)
N6	Co1	N3	C7	95.51(17)		C1	N4	C5	C4	1.9(4)
N6	Co1	N3	C6	-87.24(19)		C1	C2	C3	C4	1.2(4)
N6	Co1	N2	C9	-89.11(17)		C2	C3	C4	C5	0.5(4)
N6	Co1	N2	C10	85.80(19)		C16	N5	C19	C18	-39.1(3)
N6	C20	C21	C22	32.9(3)		C16	C17	C18	C19	-2.1(3)
N3	Co1	N2	C9	-1.33(17)		C17	C18	C19	N5	25.2(3)
N3	Co1	N2	C10	173.6(2)		C19	N5	C16	C17	38.0(3)
N3	C7	C8	$C9^1$	-179.3(2)		C20	N6	C23	C22	30.8(3)
N3	C7	C9	$C8^1$	179.4(2)		C20	C21	C22	C23	-13.4(3)
N3	C7	C9	N2	-0.3(3)		C21	C22	C23	N6	-10.1(3)
N3	C6	C5	N4	-1.2(3)		C23	N6	C20	C21	-39.6(3)
N3	C6	C5	C4	-179.1(2)		C11	N1	C15	C14	1.0(4)

N4	Co1	N3	C7	-176.71(18)		C11	C12	C13	C14	0.5(4)
N4	Co1	N3	C6	0.55(18)		C12	C11	C10	O1	0.9(4)
N4	Co1	N2	C9	7.8(5)		C12	C11	C10	N2	-178.4(2)
N4	Co1	N2	C10	-177.3(3)		C12	C13	C14	C15	0.0(4)
N4	C5	C4	C3	-2.1(4)		C13	C14	C15	N1	-0.7(4)
N4	C1	C2	C3	-1.4(4)		C15	N1	C11	C12	-0.5(4)
C7	N3	C6	O2	-1.7(4)		C15	N1	C11	C10	179.8(2)
C7	N3	C6	C5	177.1(2)		C10	C11	C12	C13	179.4(2)

Table A6 Hydrogen Atom Coordinates (Å×10^4) and Isotropic Displacement Parameters (Å^2×10^3) for [(Co^{III})$_2$L^2(pyrr)$_4$](ClO$_4$)$_2$

Atom	*x*	*y*	*z*	U(eq)
H5	717	9937	1433	18
H6	5610	10393	2814	17
H8	6124	12417	332	13
H1	1851	11469	3996	22
H2	2152	13707	4811	22
H3	3815	15579	4376	25
H4	5065	15138	3095	23
H16A	517	12425	2588	30
H16B	-355	10825	2601	30
H17A	-1492	12963	1824	31
H17B	-1948	11244	1541	31
H18A	-347	13142	589	36
H18B	-747	11408	322	36
H19A	1761	11263	468	32
H19B	1942	12731	1123	32
H20A	6117	8614	1835	35
H20B	5015	7416	2246	35
H21A	7813	8715	2941	34
H21B	7200	7007	2927	34
H22A	5964	7451	4146	29
H22B	6915	9021	4266	29
H23A	3902	8526	3786	34
H23B	4773	10093	4081	34
H12	1043	5172	1862	25
H13	-129	4997	3175	25
H14	-60	7115	4149	23
H15	1144	9297	3794	19
H24A	3188	4466	-1101	58
H24B	3781	3454	-402	58
H24C	2436	4498	-186	58

Crystal structure for $[(Co^{II})_2L^2(pyrr)_2]^0$ presented in chapter 4.

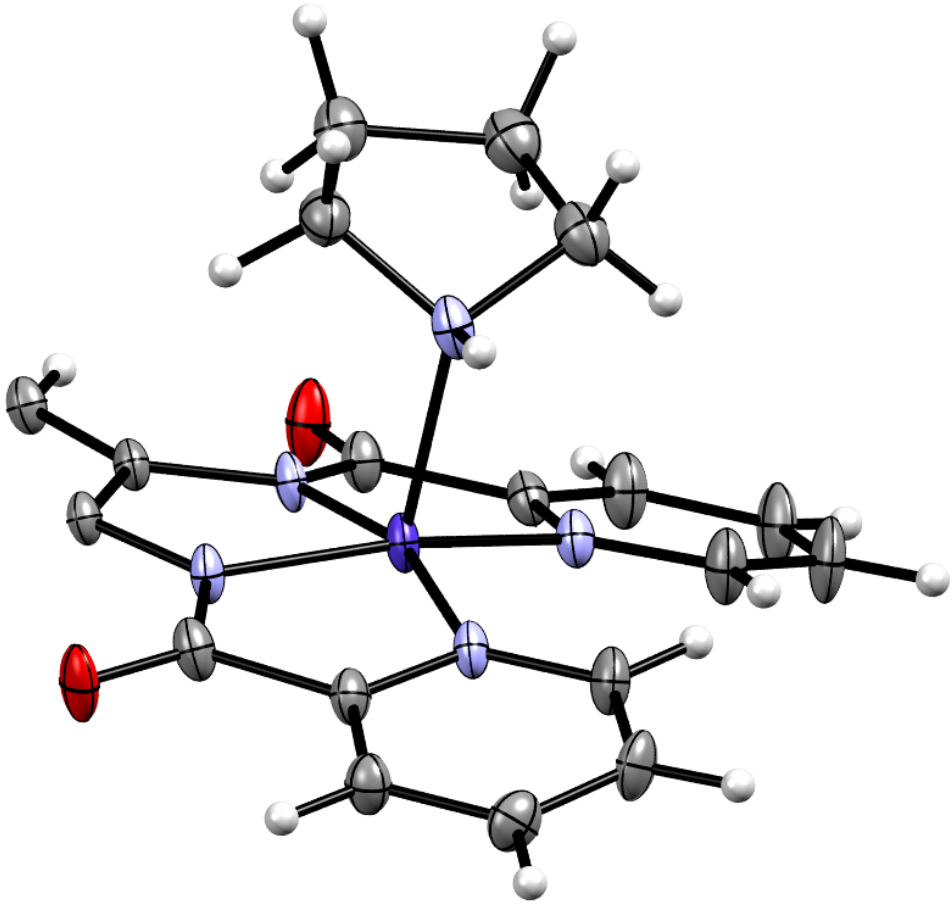

Table A7 Fractional Atomic Coordinates ($\times 10^4$) and Equivalent Isotropic Displacement Parameters ($Å^2 \times 10^3$) for final1. U_{eq} is defined as 1/3 of of the trace of the orthogonalised U_{IJ} tensor.

Atom	*x*	*y*	*z*	U(eq)
Co1	725.8(6)	6042.4(3)	2484.8(3)	16.92(16)
O1	1928(4)	3506.9(17)	2185.9(17)	31.2(7)
O2	-2274(3)	7367.8(17)	540.8(17)	27.6(7)
N2	1044(4)	4951.5(19)	1912.8(19)	17.3(7)
N1	1560(4)	5387(2)	3634(2)	19.4(7)
N3	-448(4)	6330.6(19)	1315.2(19)	17.2(7)
N4	-276(4)	7170.0(19)	2867.3(19)	18.4(7)
N5	3170(4)	6690(2)	2295(2)	21.6(7)
C7	576(4)	4922(2)	937(2)	16.0(8)
C8	-287(4)	5697(2)	603(2)	15.5(8)
C9	862(5)	4227(2)	338(2)	17.0(8)
C1	1856(5)	5638(3)	4536(2)	27.7(10)
C2	2414(6)	5059(3)	5240(3)	33.9(11)
C3	2685(6)	4201(3)	5038(3)	30(1)
C4	2452(5)	3932(3)	4121(2)	26.9(9)
C5	1897(5)	4530(2)	3442(2)	19.6(8)
C6	1639(5)	4269(3)	2435(2)	20.3(9)
C10	-1399(5)	7063(2)	1230(2)	20.8(9)
C11	-1321(5)	7539(2)	2155(2)	18.7(8)
C15	-87(5)	7620(3)	3668(2)	24.0(9)
C14	-978(5)	8381(2)	3827(3)	24.9(9)
C13	-2117(5)	8720(2)	3129(3)	25.0(9)
C12	-2273(5)	8292(2)	2271(2)	22.1(9)
C19	3842(5)	6571(3)	1360(3)	25.5(9)
C18	4953(5)	5730(3)	1461(3)	28.5(10)
C17	5536(5)	5684(3)	2518(3)	30.3(10)
C16	4731(5)	6488(3)	2944(3)	27.7(10)

Table A8 Anisotropic Displacement Parameters ($Å^2 \times 10^3$) for final1. The Anisotropic displacement factor exponent takes the form: $-2\pi^2[h^2a^{*2}U_{11}+2hka^*b^*U_{12}+\ldots]$.

Atom	U_{11}	U_{22}	U_{33}	U_{23}	U_{13}	U_{12}
Co1	24.0(3)	14.5(3)	11.1(3)	-0.6(2)	-6.08(19)	-0.1(2)
O1	56.2(19)	17.8(16)	17.7(14)	0.0(12)	-9.4(13)	7.0(14)
O2	38.7(17)	23.9(16)	17.8(14)	-1.3(12)	-13.8(12)	11.0(13)
N2	23.7(17)	15.7(17)	11.2(16)	2.1(13)	-7.1(13)	0.3(13)
N1	24.0(17)	19.3(18)	14.0(16)	-1.8(13)	-3.7(13)	-2.6(14)
N3	24.0(17)	14.6(17)	11.9(16)	-2.3(13)	-6.0(13)	1.0(13)
N4	23.2(17)	19.2(18)	12.0(16)	-1.8(14)	-4.5(13)	-2.8(13)
N5	26.2(18)	18.7(19)	18.5(17)	-1.9(14)	-7.4(14)	-0.3(14)
C7	18(2)	17(2)	12.1(18)	-0.2(15)	-3.9(15)	-1.4(15)
C8	19.1(19)	13.4(19)	13.3(19)	-2.0(15)	-3.8(15)	-2.1(15)
C9	22(2)	12.1(19)	16.0(19)	1.4(15)	-4.5(15)	-0.6(15)
C1	42(3)	23(2)	16(2)	-2.2(18)	-7.8(18)	4.2(19)
C2	55(3)	32(3)	12(2)	-1.4(18)	-10.1(19)	4(2)
C3	50(3)	23(2)	14(2)	5.4(17)	-10.3(18)	3.7(19)
C4	42(2)	18(2)	19(2)	-0.1(18)	-6.6(18)	1.2(19)
C5	22(2)	20(2)	16(2)	1.3(16)	-4.3(16)	-4.3(17)
C6	27(2)	16(2)	17(2)	-1.9(17)	-3.5(16)	-1.1(17)
C10	26(2)	17(2)	18(2)	-0.8(17)	-7.2(17)	-1.4(17)
C11	23(2)	17(2)	15.8(19)	-3.7(16)	-2.2(16)	-3.0(16)
C15	34(2)	24(2)	13(2)	-0.7(17)	-4.3(17)	0.1(18)
C14	40(2)	19(2)	15(2)	-6.0(17)	0.0(18)	0.5(18)
C13	32(2)	19(2)	24(2)	-4.4(17)	4.1(18)	1.2(17)
C12	27(2)	20(2)	18(2)	0.7(16)	-3.1(16)	3.7(17)
C19	27(2)	29(2)	20(2)	1.6(18)	-0.6(17)	-3.8(18)
C18	30(2)	28(2)	26(2)	-2.8(19)	-2.2(18)	-2.7(18)

C17	30(2)	30(2)	30(2)	3(2)	-2.2(19)	-4.0(19)
C16	29(2)	28(2)	26(2)	3.9(19)	-5.2(18)	-3.4(19)

Table A9 Bond Lengths for $[(Co^{II})_2L^2(pyrr)_2]^0$.

Atom	Atom	Length/Å		Atom	Atom	Length/Å
Co1	N2	1.875(3)		C7	C8	1.416(5)
Co1	N1	1.985(3)		C7	C9	1.390(5)
Co1	N3	1.887(3)		C8	C9[1]	1.388(5)
Co1	N4	1.974(3)		C9	C8[1]	1.388(5)
Co1	N5	2.148(3)		C1	C2	1.379(5)
O1	C6	1.238(4)		C2	C3	1.357(6)
O2	C10	1.237(4)		C3	C4	1.373(5)
N2	C7	1.415(4)		C4	C5	1.375(5)
N2	C6	1.338(4)		C5	C6	1.493(5)
N1	C1	1.348(4)		C10	C11	1.507(5)
N1	C5	1.361(5)		C11	C12	1.374(5)
N3	C8	1.416(4)		C15	C14	1.372(5)
N3	C10	1.330(5)		C14	C13	1.372(5)
N4	C11	1.365(4)		C13	C12	1.387(5)
N4	C15	1.333(4)		C19	C18	1.537(5)
N5	C19	1.482(5)		C18	C17	1.545(5)
N5	C16	1.485(5)		C17	C16	1.518(6)

[1]-X,1-Y,-Z

Table A10 Bond Angles for $[(Co^{II})_2L^2(pyrr)_2]^0$.

Atom	Atom	Atom	Angle/°		Atom	Atom	Atom	Angle/°
N2	Co1	N1	82.69(12)		N3	C8	C7	112.9(3)
N2	Co1	N3	83.52(12)		C9[1]	C8	N3	127.1(3)
N2	Co1	N4	163.16(12)		C9[1]	C8	C7	120.1(3)
N2	Co1	N5	101.96(13)		C8[1]	C9	C7	118.8(3)
N1	Co1	N5	96.30(12)		N1	C1	C2	122.5(4)
N3	Co1	N1	161.93(12)		C3	C2	C1	120.2(4)
N3	Co1	N4	82.92(12)		C2	C3	C4	118.6(4)
N3	Co1	N5	97.95(12)		C3	C4	C5	119.3(4)
N4	Co1	N1	108.24(12)		N1	C5	C4	123.0(3)
N4	Co1	N5	89.77(12)		N1	C5	C6	115.9(3)
C7	N2	Co1	115.3(2)		C4	C5	C6	121.1(3)
C6	N2	Co1	119.5(2)		O1	C6	N2	128.8(3)
C6	N2	C7	125.1(3)		O1	C6	C5	120.9(3)
C1	N1	Co1	132.1(3)		N2	C6	C5	110.2(3)
C1	N1	C5	116.4(3)		O2	C10	N3	130.1(3)
C5	N1	Co1	111.5(2)		O2	C10	C11	120.1(3)
C8	N3	Co1	114.7(2)		N3	C10	C11	109.8(3)
C10	N3	Co1	119.6(2)		N4	C11	C10	116.0(3)
C10	N3	C8	125.6(3)		N4	C11	C12	122.5(3)
C11	N4	Co1	111.5(2)		C12	C11	C10	121.5(3)
C15	N4	Co1	131.8(3)		N4	C15	C14	123.7(3)
C15	N4	C11	116.6(3)		C15	C14	C13	119.5(3)
C19	N5	Co1	115.1(2)		C14	C13	C12	118.2(4)
C19	N5	C16	102.7(3)		C11	C12	C13	119.3(3)
C16	N5	Co1	119.3(2)		N5	C19	C18	104.2(3)
N2	C7	C8	112.4(3)		C19	C18	C17	104.1(3)
C9	C7	N2	126.4(3)		C16	C17	C18	105.2(3)
C9	C7	C8	121.2(3)		N5	C16	C17	104.3(3)

[1]-X,1-Y,-Z

Table A11 Torsion Angles for $[(Co^{II})_2L^2(pyrr)_2]^0$.

A	B	C	D	Angle/°		A	B	C	D	Angle/°
Co1	N2	C7	C8	-8.6(4)		N4	C11	C12	C13	2.8(6)
Co1	N2	C7	C9	172.5(3)		N4	C15	C14	C13	-1.0(6)

Co1	N2	C6	O1	180.0(3)		N5	Co1	N2	C7	-87.1(2)
Co1	N2	C6	C5	1.7(4)		N5	Co1	N2	C6	94.3(3)
Co1	N1	C1	C2	178.7(3)		N5	Co1	N3	C8	92.4(3)
Co1	N1	C5	C4	-178.5(3)		N5	Co1	N3	C10	-90.7(3)
Co1	N1	C5	C6	1.9(4)		N5	C19	C18	C17	-26.0(4)
Co1	N3	C8	C7	6.3(4)		C7	N2	C6	O1	1.6(6)
Co1	N3	C8	C9[1]	-173.3(3)		C7	N2	C6	C5	-176.7(3)
Co1	N3	C10	O2	-179.3(3)		C8	N3	C10	O2	-2.7(6)
Co1	N3	C10	C11	0.2(4)		C8	N3	C10	C11	176.7(3)
Co1	N4	C11	C10	-4.1(4)		C8	C7	C9	C8[1]	0.0(6)
Co1	N4	C11	C12	175.0(3)		C9	C7	C8	N3	-179.7(3)
Co1	N4	C15	C14	-176.1(3)		C9	C7	C8	C9[1]	0.0(6)
Co1	N5	C19	C18	-88.8(3)		C1	N1	C5	C4	2.2(5)
Co1	N5	C16	C17	86.2(3)		C1	N1	C5	C6	-177.5(3)
O2	C10	C11	N4	-177.8(3)		C1	C2	C3	C4	2.3(7)
O2	C10	C11	C12	3.1(6)		C2	C3	C4	C5	-2.2(6)
N2	Co1	N3	C8	-8.8(2)		C3	C4	C5	N1	-0.1(6)
N2	Co1	N3	C10	168.1(3)		C3	C4	C5	C6	179.6(4)
N2	C7	C8	N3	1.4(4)		C4	C5	C6	O1	-0.4(6)
N2	C7	C8	C9[1]	-179.0(3)		C4	C5	C6	N2	178.0(3)
N2	C7	C9	C8[1]	178.8(3)		C5	N1	C1	C2	-2.1(6)
N1	Co1	N2	C7	178.0(3)		C6	N2	C7	C8	169.9(3)
N1	Co1	N2	C6	-0.6(3)		C6	N2	C7	C9	-9.0(6)
N1	Co1	N3	C8	-49.3(5)		C10	N3	C8	C7	-170.4(3)
N1	Co1	N3	C10	127.6(4)		C10	N3	C8	C9[1]	10.0(6)
N1	C1	C2	C3	-0.1(7)		C10	C11	C12	C13	-178.1(3)
N1	C5	C6	O1	179.2(3)		C11	N4	C15	C14	5.1(5)
N1	C5	C6	N2	-2.3(4)		C15	N4	C11	C10	174.9(3)
N3	Co1	N2	C7	9.7(2)		C15	N4	C11	C12	-6.0(5)
N3	Co1	N2	C6	-168.9(3)		C15	C14	C13	C12	-2.4(6)
N3	C10	C11	N4	2.7(5)		C14	C13	C12	C11	1.5(6)
N3	C10	C11	C12	-176.4(3)		C19	N5	C16	C17	-42.6(4)
N4	Co1	N2	C7	46.2(5)		C19	C18	C17	C16	0.1(4)
N4	Co1	N2	C6	-132.4(4)		C18	C17	C16	N5	25.8(4)
N4	Co1	N3	C8	-178.8(3)		C16	N5	C19	C18	42.6(4)
N4	Co1	N3	C10	-1.9(3)						

[1]-X,1-Y,-Z

Table A12 Hydrogen Atom Coordinates (Å×10^4) and Isotropic Displacement Parameters (Å^2×10^3) for [(Co^{II})$_2$L^2(pyrr)$_2$]^0.

Atom	*x*	*y*	*z*	U(eq)
H5	2940(50)	7300(30)	2380(20)	26
H9	1442	3709	568	20
H1	1674	6235	4693	33
H2	2610	5262	5867	41
H3	3029	3794	5522	36
H4	2672	3339	3958	32
H15	709	7401	4156	29
H14	-808	8671	4415	30
H13	-2781	9235	3231	30
H12	-3029	8517	1769	27
H19A	4568	7079	1198	31
H19B	2863	6500	870	31
H18A	5981	5767	1084	34
H18B	4247	5208	1260	34
H17A	5102	5139	2798	36
H17B	6832	5699	2622	36
H16A	4383	6359	3581	33
H16B	5567	6986	2979	33

REFERENCES

1. Lewis, N. S.; Nocera, D. G., *Proc. Natl. Acad. Sci. USA* **2006,** *103* (43), 15729-15735.

2. Ogden, J. M., *Annual Review of Energy and the Environment* **1999,** *24* (1), 227-279.

3. Kärkäs, M. D.; Verho, O.; Johnston, E. V.; Åkermark, B., *Chem. Rev.* **2014,** *114* (24), 11863-12001.

4. Suen, N.-T.; Hung, S.-F.; Quan, Q.; Zhang, N.; Xu, Y.-J.; Chen, H. M., *Chem. Soc. Rev.* **2017,** *46* (2), 337-365.

5. Thoi, V. S.; Sun, Y.; Long, J. R.; Chang, C. J., *Chem. Soc. Rev.* **2013,** *42* (6), 2388-2400.

6. Du, P.; Eisenberg, R., *Energy & Environmental Science* **2012,** *5* (3), 6012-6021.

7. Wang, M.; Chen, L.; Sun, L., *Energy & Environmental Science* **2012,** *5* (5), 6763-6778.

8. Elgrishi, N.; McCarthy, B. D.; Rountree, E. S.; Dempsey, J. L., *ACS Catalysis* **2016,** *6* (6), 3644-3659.

9. Basu, D.; Allard, M. M.; Xavier, F. R.; Heeg, M. J.; Schlegel, H. B.; Verani, C. N., *Dalton Trans.* **2015,** *44* (7), 3454-3466.

10. Basu, D.; Mazumder, S.; Shi, X.; Baydoun, H.; Niklas, J.; Poluektov, O.; Schlegel, H. B.; Verani, C. N., *Angew. Chem., Int. Ed.* **2015,** *54* (7), 2105-2110.

11. Basu, D.; Mazumder, S.; Shi, X. T.; Staples, R. J.; Schlegel, H. B.; Verani, C. N., *Angew. Chem. Int. Edit.* **2015,** *54* (24), 7139-7143.

12. Basu, D.; Mazumder, S.; Niklas, J.; Baydoun, H.; Wanniarachchi, D.; Shi, X.; Staples, R. J.; Poluektov, O.; Schlegel, H. B.; Verani, C. N., *Chem. Sci.* **2016,** *7*, 3264-3278.

13. Dempsey, J. L.; Brunschwig, B. S.; Winkler, J. R.; Gray, H. B., *Acc. Chem. Res.* **2009,** *42* (12), 1995-2004.

14. Kawano, K.; Yamauchi, K.; Sakai, K., *Chem. Commun.* **2014,** *50* (69), 9872-9875.

15. Connelly, N. G.; Geiger, W. E., *Chem. Rev.* **1996,** *96* (2), 877-910.

16. Mandal, S.; Shikano, S.; Yamada, Y.; Lee, Y.-M.; Nam, W.; Llobet, A.; Fukuzumi, S., *J. Am. Chem. Soc.* **2013,** *135* (41), 15294-15297.

17. Connolly, P.; Espenson, J. H., *Inorg. Chem.* **1986,** *25* (16), 2684-2688.

18. Sundstrom, E. J.; Yang, X.; Thoi, V. S.; Karunadasa, H. I.; Chang, C. J.; Long, J. R.; Head-Gordon, M., *J. Am. Chem. Soc.* **2012,** *134* (11), 5233-5242.

19. Eckenhoff, W. T.; Brennessel, W. W.; Eisenberg, R., *Inorg. Chem.* **2014,** *53* (18), 9860-9869.

20. Natali, M.; Luisa, A.; Iengo, E.; Scandola, F., *Chem. Commun.* **2014,** *50* (15), 1842-1844.

21. Chen, L.; Wang, M.; Han, K.; Zhang, P.; Gloaguen, F.; Sun, L., *Energy & Environmental Science* **2014,** *7* (1), 329-334.

22. Connor, G. P.; Mayer, K. J.; Tribble, C. S.; McNamara, W. R., *Inorg. Chem.* **2014,** *53* (11), 5408-5410.

23. Artero, V.; Chavarot-Kerlidou, M.; Fontecave, M., *Angew. Chem., Int. Ed.* **2011,** *50* (32), 7238-7266.

24. Rao, H.; Wang, Z.-Y.; Zheng, H.-Q.; Wang, X.-B.; Pan, C.-M.; Fan, Y.-T.; Hou, H.-W., *Catalysis Science & Technology* **2015,** *5* (4), 2332-2339.

25. Han, Z.; McNamara, W. R.; Eum, M.-S.; Holland, P. L.; Eisenberg, R., *Angew. Chem., Int. Ed.* **2012,** *51* (7), 1667-1670.

26. Zhang, M.; Zhang, M.-T.; Hou, C.; Ke, Z.-F.; Lu, T.-B., *Angew. Chem., Int. Ed.* **2014,** *53* (48), 13042-13048.

27. Yuan, Y.-J.; Tu, J.-R.; Lu, H.-W.; Yu, Z.-T.; Fan, X.-X.; Zou, Z.-G., *Dalton Trans.* **2016,** *45* (4), 1359-1363.

28. Kankanamalage, P. H. A.; Mazumder, S.; Tiwari, V.; Kpogo, K. K.; Bernhard Schlegel, H.; Verani, C. N., *Chem. Commun.* **2016,** *52* (91), 13357-13360.

29. Coggins, M. K.; Zhang, M.-T.; Chen, Z.; Song, N.; Meyer, T. J., *Angew. Chem., Int. Ed.* **2014,** *53* (45), 12226-12230.

30. Zhang, P.; Wang, M.; Yang, Y.; Yao, T.; Sun, L., *Angew. Chem., Int. Ed.* **2014,** *53* (50), 13803-13807.

31. Fu, L.-Z.; Fang, T.; Zhou, L.-L.; Zhan, S.-Z., *RSC Advances* **2014,** *4* (96), 53674-53680.

32. Tinker, L. L.; McDaniel, N. D.; Curtin, P. N.; Smith, C. K.; Ireland, M. J.; Bernhard, S., *Chem. Eur. J.* **2007,** *13* (31), 8726-8732.

33. Karunadasa, H. I.; Montalvo, E.; Sun, Y.; Majda, M.; Long, J. R.; Chang, C. J., *Science* **2012,** *335* (6069), 698-702.

34. Hu, X.; Brunschwig, B. S.; Peters, J. C., *J. Am. Chem. Soc.* **2007,** *129* (29), 8988-8998.

35. Fihri, A.; Artero, V.; Pereira, A.; Fontecave, M., *Dalton Trans.* **2008,** (41), 5567-5569.

36. Fihri, A.; Artero, V.; Razavet, M.; Baffert, C.; Leibl, W.; Fontecave, M., *Angew. Chem., Int. Ed.* **2008,** *47* (3), 564-567.

37. Dempsey, J. L.; Winkler, J. R.; Gray, H. B., *J. Am. Chem. Soc.* **2010,** *132* (47), 16774-16776.

38. Dempsey, J. L.; Winkler, J. R.; Gray, H. B., *J. Am. Chem. Soc.* **2010,** *132* (3), 1060-1065.

39. Mulfort, K. L.; Tiede, D. M., *J. Phys. Chem. B* **2010,** *114* (45), 14572-14581.

40. McCormick, T. M.; Han, Z.; Weinberg, D. J.; Brennessel, W. W.; Holland, P. L.; Eisenberg, R., *Inorg. Chem.* **2011,** *50* (21), 10660-10666.

41. Muckerman, J. T.; Fujita, E., *Chem. Commun.* **2011,** *47* (46), 12456-12458.

42. Solis, B. H.; Hammes-Schiffer, S., *J. Am. Chem. Soc.* **2011,** *133* (47), 19036-19039.

43. Solis, B. H.; Hammes-Schiffer, S., *Inorg. Chem.* **2011,** *50* (21), 11252-11262.

44. Solis, B. H.; Yu, Y.; Hammes-Schiffer, S., *Inorg. Chem.* **2013,** *52* (12), 6994-6999.

45. Kaeffer, N.; Morozan, A.; Fize, J.; Martinez, E.; Guetaz, L.; Artero, V., *ACS Catalysis* **2016,** *6* (6), 3727-3737.

46. Reuillard, B.; Warnan, J.; Leung, J. J.; Wakerley, D. W.; Reisner, E., *Angew. Chem.* **2016,** *128* (12), 4020-4025.

47. Bhattacharjee, A.; Andreiadis, E. S.; Chavarot-Kerlidou, M.; Fontecave, M.; Field, M. J.; Artero, V., *Chem. Eur. J.* **2013,** *19* (45), 15166-15174.

48. Sun, Y.; Bigi, J. P.; Piro, N. A.; Tang, M. L.; Long, J. R.; Chang, C. J., *J. Am. Chem. Soc.* **2011,** *133* (24), 9212-9215.

49. Khnayzer, R. S.; Thoi, V. S.; Nippe, M.; King, A. E.; Jurss, J. W.; El Roz, K. A.; Long, J. R.; Chang, C. J.; Castellano, F. N., *Energy & Environmental Science* **2014,** *7* (4), 1477-1488.

50. Zee, D. Z.; Chantarojsiri, T.; Long, J. R.; Chang, C. J., *Acc. Chem. Res.* **2015,** *48* (7), 2027-2036.

51. Nippe, M.; Khnayzer, R. S.; Panetier, J. A.; Zee, D. Z.; Olaiya, B. S.; Head-Gordon, M.; Chang, C. J.; Castellano, F. N.; Long, J. R., *Chem. Sci.* **2013,** *4* (10), 3934-3945.

52. Lesh, F. D.; Shanmugam, R.; Allard, M. M.; Lanznaster, M.; Heeg, M. J.; Rodgers, M. T.; Shearer, J. M.; Verani, C. N., *Inorg. Chem.* **2010,** *49* (16), 7226-7228.

53. Allard, M. M.; Sonk, J. A.; Heeg, M. J.; McGarvey, B. R.; Schlegel, H. B.; Verani, C. N., *Angew. Chem. Int. Edit.* **2012,** *51* (13), 3178-3182.

54. Allard, M. M.; Xavier, F. R.; Heeg, M. J.; Schlegel, H. B.; Verani, C. N., *Eur. J. Inorg. Chem.* **2012,** (29), 4622-4631.

55. Wickramasinghe, L. D.; Perera, M. M.; Li, L.; Mao, G. Z.; Zhou, Z. X.; Verani, C. N., *Angew. Chem. Int. Edit.* **2013,** *52* (50), 13346-13350.

56. Wickramasinghe, L. D.; Mazumder, S.; Gonawala, S.; Perera, M. M.; Baydoun, H.; Thapa, B.; Li, L.; Xie, L.; Mao, G.; Zhou, Z.; Schlegel, H. B.; Verani, C. N., *Angew. Chem., Int. Ed.* **2014,** *53* (52), 14462-14467.

57. Gonawala, S.; Leopoldino, V. R.; Kpogo, K.; Verani, C. N., *Chem. Commun.* **2016,** *52* (74), 11155-11158.

58. Johnson, M. S.; Wickramasinghe, L.; Verani, C.; Metzger, R. M., *The Journal of Physical Chemistry C* **2016,** *120* (19), 10578-10583.

59. Wickramasinghe, L. D.; Mazumder, S.; Kpogo, K. K.; Staples, R. J.; Schlegel, H. B.; Verani, C. N., *Chem-Eur J* **2016,** *22* (31), 10786-10790.

60. Baydoun, H.; Mazumder, S.; Schlegel, H. B.; Verani, C. N., *Chem. Eur. J.* **2017,** *23* (39), 9266-9271.

61. Szymczak, N. K.; Berben, L. A.; Peters, J. C., *Chem. Commun.* **2009,** (44), 6729-6731.

62. Kal, S.; Filatov, A. S.; Dinolfo, P. H., *Inorg. Chem.* **2014,** *53* (14), 7137-7145.

63. Valdez, C. N.; Dempsey, J. L.; Brunschwig, B. S.; Winkler, J. R.; Gray, H. B., *Proc. Natl. Acad. Sci. USA* **2012,** *109* (39), 15589-15593.

64. Laga, S. M.; Blakemore, J. D.; Henling, L. M.; Brunschwig, B. S.; Gray, H. B., *Inorg. Chem.* **2014,** *53* (24), 12668-12670.

65. Di Giovanni, C.; Gimbert-Suriñach, C.; Nippe, M.; Benet-Buchholz, J.; Long, J. R.; Sala, X.; Llobet, A., *Chem. Eur. J.* **2016,** *22* (1), 361-369.

66. Kpogo, K. K.; Mazumder, S.; Wang, D.; Schlegel, H. B.; Fiedler, A. T.; Verani, C. N., *Chem. Eur. J.* **2017,** *23* (39), 9272-9279.

67. Gersten, S. W.; Samuels, G. J.; Meyer, T. J., *J. Am. Chem. Soc.* **1982,** *104* (14), 4029-4030.

68. Zong, R.; Thummel, R. P., *J. Am. Chem. Soc.* **2005,** *127* (37), 12802-12803.

69. Leung, C.-F.; Ng, S.-M.; Ko, C.-C.; Man, W.-L.; Wu, J.; Chen, L.; Lau, T.-C., *Energy & Environmental Science* **2012,** *5* (7), 7903-7907.

70. Puntoriero, F.; Sartorel, A.; Orlandi, M.; La Ganga, G.; Serroni, S.; Bonchio, M.; Scandola, F.; Campagna, S., *Coord. Chem. Rev.* **2011,** *255* (21–22), 2594-2601.

71. Young, K. J.; Takase, M. K.; Brudvig, G. W., *Inorg. Chem.* **2013,** *52* (13), 7615-7622.

72. Fillol, J. L.; Codolà, Z.; Garcia-Bosch, I.; Gómez, L.; Pla, J. J.; Costas, M., *Nat. Chem.* **2011,** *3* (10), 807-813.

73. Ellis, W. C.; McDaniel, N. D.; Bernhard, S.; Collins, T. J., *J. Am. Chem. Soc.* **2010,** *132* (32), 10990-10991.

74. Coggins, M. K.; Zhang, M.-T.; Vannucci, A. K.; Dares, C. J.; Meyer, T. J., *J. Am. Chem. Soc.* **2014,** *136* (15), 5531-5534.

75. Gonawala, S.; Baydoun, H.; Wickramasinghe, L.; Verani, C. N., *Chem. Commun.* **2016,** *52* (54), 8440-8443.

76. Li, F.; Zhang, B.; Li, X.; Jiang, Y.; Chen, L.; Li, Y.; Sun, L., *Angew. Chem., Int. Ed.* **2011,** *50* (51), 12276-12279.

77. Li, F.; Li, L.; Tong, L.; Daniel, Q.; Gothelid, M.; Sun, L., *Chem. Commun.* **2014,** *50* (90), 13948-13951.

78. Sheehan, S. W.; Thomsen, J. M.; Hintermair, U.; Crabtree, R. H.; Brudvig, G. W.; Schmuttenmaer, C. A., *Nat. Commun.* **2015,** *6*, 6469.

79. Liang, Y.; Li, Y.; Wang, H.; Zhou, J.; Wang, J.; Regier, T.; Dai, H., *Nat. Mater.* **2011,** *10* (10), 780-786.

80. Kanan, M. W.; Nocera, D. G., *Science* **2008,** *321* (5892), 1072-1075.

81. Janiak, C., *J. Chem. Soc., Dalton Trans.* **2000,** (21), 3885-3896.

82. Eady, S. C.; MacInnes, M. M.; Lehnert, N., *ACS Appl. Mater. Interfaces* **2016,** *8* (36), 23624-23634.

83. Kramer, W. W.; McCrory, C. C. L., *Chem. Sci.* **2016,** *7* (4), 2506-2515.

84. Eady, S. C.; Peczonczyk, S. L.; Maldonado, S.; Lehnert, N., *Chem. Commun.* **2014,** *50* (59), 8065-8068.

85. Das, A.; Stahl, S. S., *Angew. Chem.*, n/a-n/a.

86. Rezaeifard, A.; Jafarpour, M., *Catalysis Science & Technology* **2014,** *4* (7), 1960-1969.

87. Bullock, R. M.; Das, A. K.; Appel, A. M., *Chem. Eur. J.* **2017,** *23* (32), 7626-7641.

88. Duan, L.; Wang, L.; Li, F.; Li, F.; Sun, L., *Acc. Chem. Res.* **2015,** *48* (7), 2084-2096.

89. Scherrer, D.; Schilling, M.; Luber, S.; Fox, T.; Spingler, B.; Alberto, R.; Richmond, C. J., *Dalton Trans.* **2016,** *45* (48), 19361-19367.

90. Yamamoto, M.; Wang, L.; Li, F.; Fukushima, T.; Tanaka, K.; Sun, L.; Imahori, H., *Chem. Sci.* **2016,** *7* (2), 1430-1439.

91. Yamamoto, M.; Nishizawa, Y.; Chabera, P.; Li, F.; Pascher, T.; Sundstrom, V.; Sun, L.; Imahori, H., *Chem. Commun.* **2016,** *52* (94), 13702-13705.

92. Lu, Z.; Gao, Y.; Chen, H.; Liu, Z.; Sun, L., *Dalton Trans.* **2017,** *46* (4), 1304-1310.

93. Wang, Y.; Duan, L.; Wang, L.; Chen, H.; Sun, J.; Sun, L.; Ahlquist, M. S. G., *ACS Catalysis* **2015,** *5* (7), 3966-3972.

94. Duan, L.; Xu, Y.; Gorlov, M.; Tong, L.; Andersson, S.; Sun, L., *Chem. Eur. J.* **2010,** *16* (15), 4659-4668.

95. Chen, H.; Sun, Z.; Liu, X.; Han, A.; Du, P., *The Journal of Physical Chemistry C* **2015,** *119* (17), 8998-9004.

96. Robert M. Silverstein, F. X. W., David J. Kiemle, David L. Bryce, *Spectrometric Identification of Organic Compounds*. 8th Edition ed.; John Wiley & Sons: 2014.

97. Pozniak, B. P.; Cole, R. B., *J. Am. Soc. Mass Spectrom.* **2007,** *18* (4), 737-748.

98. Sheldrick, G., *Acta Crystallographica Section A* **2008,** *64* (1), 112-122.

99. Dolomanov, O. V.; Bourhis, L. J.; Gildea, R. J.; Howard, J. A. K.; Puschmann, H., *J. Appl. Crystallogr.* **2009,** *42* (2), 339-341.

100. Kissinger, P. T.; Heineman, W. R., *J. Chem. Educ.* **1983,** *60* (9), 702.

101. Gagne, R. R.; Koval, C. A.; Lisensky, G. C., *Inorg. Chem.* **1980,** *19* (9), 2854-2855.

102. Bunce, N. J., *J. Chem. Educ.* **1987,** *64* (11), 907.

103. Huang, W., Reduction Chemistry of Rare-Earth Metal Complexes: Toward New Reactivity and Properties. 2013.

104. McCrory, C. C. L.; Jung, S.; Peters, J. C.; Jaramillo, T. F., *J. Am. Chem. Soc.* **2013,** *135* (45), 16977-16987.

105. Zhang, P.; Wang, M.; Yang, Y.; Zheng, D.; Han, K.; Sun, L., *Chem. Commun.* **2014,** *50* (91), 14153-14156.

106. Han, Z.; Eisenberg, R., *Acc. Chem. Res.* **2014,** *47* (8), 2537-2544.

107. Call, A.; Codolà, Z.; Acuña-Parés, F.; Lloret-Fillol, J., *Chem. Eur. J.* **2014,** *20* (20), 6171-6183.

108. Zhang, P.; Wang, M.; Gloaguen, F.; Chen, L.; Quentel, F.; Sun, L., *Chem. Commun.* **2013,** *49* (82), 9455-9457.

109. Zarkadoulas, A.; Field, M. J.; Papatriantafyllopoulou, C.; Fize, J.; Artero, V.; Mitsopoulou, C. A., *Inorg. Chem.* **2016,** *55* (2), 432-444.

110. Letko, C. S.; Panetier, J. A.; Head-Gordon, M.; Tilley, T. D., *J. Am. Chem. Soc.* **2014,** *136* (26), 9364-9376.

111. Quintana, L. M. A.; Johnson, S. I.; Corona, S. L.; Villatoro, W.; Goddard, W. A.; Takase, M. K.; VanderVelde, D. G.; Winkler, J. R.; Gray, H. B.; Blakemore, J. D., *Proc. Natl. Acad. Sci. USA* **2016,** *113* (23), 6409-6414.

112. McCarthy, B. D.; Donley, C. L.; Dempsey, J. L., *Chem. Sci.* **2015,** *6* (5), 2827-2834.

113. Anxolabéhère-Mallart, E.; Costentin, C.; Fournier, M.; Nowak, S.; Robert, M.; Savéant, J.-M., *J. Am. Chem. Soc.* **2012,** *134* (14), 6104-6107.

114. Barnes, D. J.; Chapman, R. L.; Vagg, R. S.; Watton, E. C., *J. Chem. Eng. Data* **1978,** *23* (4), 349-350.

115. Reiher, M.; Salomon, O.; Artur Hess, B., *Theor. Chem. Acc.* **2001,** *107* (1), 48-55.

116. Frisch, M. J.; Trucks, G. W.; Schlegel, H. B.; G. E. Scuseria; Robb, M. A.; Cheeseman, J. R.; Scalmani, G.; Barone, V.; B. Mennucci; Petersson, G. A.; et_al *Gaussian Development Version: Revision H.35*, Revision H.35; Gaussian, Inc.: Wallingford, CT, 2014.

117. Dolg, M.; Wedig, U.; Stoll, H.; Preuss, H., *J. Chem. Phys.* **1987,** *86* (2), 866-872.

118. Hariharan, P. C.; Pople, J. A., *Theor. Chim. Acta* **1973,** *28* (3), 213-222.

119. Francl, M. M.; Pietro, W. J.; Hehre, W. J.; Binkley, J. S.; Gordon, M. S.; DeFrees, D. J.; Pople, J. A., *J. Chem. Phys.* **1982,** *77* (7), 3654-3665.

120. Marenich, A. V.; Cramer, C. J.; Truhlar, D. G., *J. Phys. Chem. B* **2009,** *113* (18), 6378-6396.

121. Kelly, C. P.; Cramer, C. J.; Truhlar, D. G., *J. Phys. Chem. B* **2006,** *110* (32), 16066-16081.

122. Pennington, R. K., T.; Millam, J. M. *GaussView*, Semichem, Inc.: Shawnee Mission, KS 2009.

123. Petit, L.; Maldivi, P.; Adamo, C., *J. Chem. Theory Comput.* **2005,** *1* (5), 953-962.

124. Runge, E.; Gross, E. K. U., *Phys. Rev. Lett.* **1984,** *52* (12), 997-1000.

125. Stratmann, R. E.; Scuseria, G. E.; Frisch, M. J., *J. Chem. Phys.* **1998,** *109* (19), 8218-8224.

126. Martin, R. L., *J. Chem. Phys.* **2003,** *118* (11), 4775-4777.

127. apex. APEX2 V2010.11-3. Software for the CCD Detector System; Bruker Analytical X-ray Systems, Madison, WI (2010). .

128. Amirnasr, M.; Schenk, K. J.; Meghdadi, S., *Inorg. Chim. Acta* **2002,** *338*, 19-26.

129. Meghdadi, S.; Amirnasr, M.; Habibi, M. H.; Amiri, A.; Ghodsi, V.; Rohani, A.; Harrington, R. W.; Clegg, W., *Polyhedron* **2008,** *27* (13), 2771-2778.

130. Dutta, S. K.; Beckmann, U.; Bill, E.; Weyhermüller, T.; Wieghardt, K., *Inorg. Chem.* **2000,** *39* (15), 3355-3364.

131. Beckmann, U.; Bill, E.; Weyhermüller, T.; Wieghardt, K., *Inorg. Chem.* **2003,** *42* (4), 1045-1056.

132. Shakya, R.; Hindo, S. S.; Wu, L.; Allard, M. M.; Heeg, M. J.; Hratchian, H. P.; McGarvey, B. R.; Da Rocha, S. R. P.; Verani, C. N., *Inorg. Chem.* **2007,** *46* (23), 9808-9818.

133. Singh, W. M.; Baine, T.; Kudo, S.; Tian, S.; Ma, X. A. N.; Zhou, H.; DeYonker, N. J.; Pham, T. C.; Bollinger, J. C.; Baker, D. L.; Yan, B.; Webster, C. E.; Zhao, X., *Angew. Chem., Int. Ed.* **2012,** *51* (24), 5941-5944.

134. Vennampalli, M.; Liang, G.; Katta, L.; Webster, C. E.; Zhao, X., *Inorg. Chem.* **2014,** *53* (19), 10094-10100.

135. Addison, A. W.; Rao, T. N.; Reedijk, J.; van Rijn, J.; Verschoor, G. C., *J. Chem. Soc., Dalton Trans.* **1984,** (7), 1349-1356.

136. Blanchard, S.; Neese, F.; Bothe, E.; Bill, E.; Weyhermüller, T.; Wieghardt, K., *Inorg. Chem.* **2005,** *44* (10), 3636-3656.

137. Kochem, A.; Kanso, H.; Baptiste, B.; Arora, H.; Philouze, C.; Jarjayes, O.; Vezin, H.; Luneau, D.; Orio, M.; Thomas, F., *Inorg. Chem.* **2012,** *51* (20), 10557-10571.

138. Scarborough, C. C.; Sproules, S.; Weyhermüller, T.; DeBeer, S.; Wieghardt, K., *Inorg. Chem.* **2011,** *50* (24), 12446-12462.

139. Storr, T.; Verma, P.; Shimazaki, Y.; Wasinger, E. C.; Stack, T. D. P., *Chem. Eur. J.* **2010,** *16* (30), 8980-8983.

140. Kaim, W., *Coord. Chem. Rev.* **2011,** *255* (21–22), 2503-2513.

141. Shultz, D. A., Valence Tautomerism in Dioxolene Complexes of Cobalt. In *Magnetism: Molecules to Materials*, Wiley-VCH Verlag GmbH & Co. KGaA: 2003; pp 281-306.

142. Buchanan, R. M.; Pierpont, C. G., *J. Am. Chem. Soc.* **1980,** *102* (15), 4951-4957.

143. Schmidt, R. D.; Shultz, D. A.; Martin, J. D.; Boyle, P. D., *J. Am. Chem. Soc.* **2010,** *132* (17), 6261-6273.

144. Ishizuka, T.; Watanabe, A.; Kotani, H.; Hong, D.; Satonaka, K.; Wada, T.; Shiota, Y.; Yoshizawa, K.; Ohara, K.; Yamaguchi, K.; Kato, S.; Fukuzumi, S.; Kojima, T., *Inorg. Chem.* **2016,** *55* (3), 1154-1164.

145. *APEX II collection and processing program*, Bruker AXS Inc: 2009.

146. Garrido-Barros, P.; Funes-Ardoiz, I.; Drouet, S.; Benet-Buchholz, J.; Maseras, F.; Llobet, A., *J. Am. Chem. Soc.* **2015,** *137* (21), 6758-6761.

147. Nakazono, T.; Parent, A. R.; Sakai, K., *Chem. Eur. J.* **2015,** *21* (18), 6723-6726.

148. Lyaskovskyy, V.; de Bruin, B., *ACS Catalysis* **2012,** *2* (2), 270-279.

149. Lei, H.; Liu, C.; Wang, Z.; Zhang, Z.; Zhang, M.; Chang, X.; Zhang, W.; Cao, R., *ACS Catalysis* **2016,** *6* (10), 6429-6437.

150. Li, D.; Baydoun, H.; Verani, C. N.; Brock, S. L., *J. Am. Chem. Soc.* **2016,** *138* (12), 4006-4009.

151. Wickramasinghe, L. Redox-Active Trivalent Metallosurfactants With Low Global Symmetry For Molecule-Based Electronics: Spectroscopic, Electrochemical, And Amphiphilic Properties Of New Molecular Materials For Current-Voltage Measurements In M|lb-Monolayer|m Devices. Wayne State university, 2014.

152. Frisch, M. J.; Trucks, G. W.; Schlegel, H. B.; Scuseria, G. E.; Robb, M. A.; Cheeseman, J. R.; Scalmani, G.; Barone, V.; Petersson, G. A.; Nakatsuji, H.; Li, X.; Caricato, M.; Marenich, A.; Bloino, J.; Janesko, B. G.; Gomperts, R.; Mennucci, B.; Hratchian, H. P.; Ortiz, J. V.; Izmaylov, A. F.; Sonnenberg, J. L.; Williams-Young, D.; Ding, F.; Lipparini, F.; Egidi, F.; Goings, J.; Peng, B.; Petrone, A.; Henderson, T.; Ranasinghe, D.; Zakrzewski, V. G.; Gao, J.; Rega, N.; Zheng, G.; Liang, W.; Hada, M.; Ehara, M.; Toyota, K.; Fukuda, R.; Hasegawa, J.; Ishida, M.; Nakajima, T.; Honda, Y.; Kitao, O.; Nakai, H.; Vreven, T.; Throssell, K.;

Montgomery, J. A.; Jr.; Peralta, J. E.; Ogliaro, F.; Bearpark, M.; Heyd, J. J.; Brothers, E.; Kudin, K. N.; Staroverov, V. N.; Keith, T.; Kobayashi, R.; Normand, J.; Raghavachari, K.; Rendell, A.; Burant, J. C.; Iyengar, S. S.; Tomasi, J.; Cossi, M.; Millam, J. M.; Klene, M.; Adamo, C.; Cammi, R.; Ochterski, J. W.; Martin, R. L.; Morokuma, K.; Farkas, O.; Foresman, J. B.; Fox, D. J., **2016**.

153. Thapa, B.; Schlegel, H. B., *The Journal of Physical Chemistry A* **2017,** *121* (24), 4698-4706.

154. Thapa, B.; Schlegel, H. B., *The Journal of Physical Chemistry A* **2015,** *119* (21), 5134-5144.

155. Thapa, B.; Schlegel, H. B., *The Journal of Physical Chemistry A* **2016,** *120* (44), 8916-8922.

156. Thapa, B.; Schlegel, H. B., *The Journal of Physical Chemistry A* **2016,** *120* (28), 5726-5735.

157. Bartmess, J. E., *The Journal of Physical Chemistry* **1994,** *98* (25), 6420-6424.

158. Camaioni, D. M.; Schwerdtfeger, C. A., *The Journal of Physical Chemistry A* **2005,** *109* (47), 10795-10797.

159. Isse, A. A.; Gennaro, A., *The Journal of Physical Chemistry B* **2010,** *114* (23), 7894-7899.

160. Kelly, C. P.; Cramer, C. J.; Truhlar, D. G., *The Journal of Physical Chemistry B* **2006,** *110* (32), 16066-16081.

161. Ben-Naim, A.; Marcus, Y., *The Journal of chemical physics* **1984,** *81* (4), 2016-2027.

162. Wickramasinghe, L. D.; Mazumder, S.; Gonawala, S.; Perera, M. M.; Baydoun, H.; Thapa, B.; Li, L.; Xie, L. X.; Mao, G. Z.; Zhou, Z. X.; Schlegel, H. B.; Verani, C. N., *Angew. Chem. Int. Edit.* **2014,** *53* (52), 14462-14467.

163. Kärkäs, M. D.; Åkermark, T.; Chen, H.; Sun, J.; Åkermark, B., *Angew. Chem., Int. Ed.* **2013,** *52* (15), 4189-4193.

164. Lee, S. H.; Han, J. H.; Kwak, H.; Lee, S. J.; Lee, E. Y.; Kim, H. J.; Lee, J. H.; Bae, C.; Lee, S. N.; Kim, Y.; Kim, C., *Chem. Eur. J.* **2007,** *13* (33), 9393-9398.

165. Song, Y. J.; Hyun, M. Y.; Lee, J. H.; Lee, H. G.; Kim, J. H.; Jang, S. P.; Noh, J. Y.; Kim, Y.; Kim, S.-J.; Lee, S. J.; Kim, C., *Chem. Eur. J.* **2012,** *18* (19), 6094-6101.

166. Song, Y. J.; Lee, S. H.; Park, H. M.; Kim, S. H.; Goo, H. G.; Eom, G. H.; Lee, J. H.; Lah, M. S.; Kim, Y.; Kim, S.-J.; Lee, J. E.; Lee, H.-I.; Kim, C., *Chem. Eur. J.* **2011,** *17* (26), 7336-7344.

167. Li, D.; Baydoun, H.; Kulikowski, B.; Brock, S. L., *Chem. Mater.* **2017,** *29* (7), 3048-3054.

168. Galán-Mascarós, J. R., *ChemElectroChem* **2015,** *2* (1), 37-50.

169. Tahir, M.; Pan, L.; Idrees, F.; Zhang, X.; Wang, L.; Zou, J.-J.; Wang, Z. L., *Nano Energy* **2017,** *37*, 136-157.

170. Lee, W.-T.; Muñoz, S. B.; Dickie, D. A.; Smith, J. M., *Angew. Chem., Int. Ed.* **2014,** *53* (37), 9856-9859.

171. Nakazono, T.; Parent, A. R.; Sakai, K., *Chem. Commun.* **2013,** *49* (56), 6325-6327.

172. Parent, A. R.; Sakai, K., *ChemSusChem* **2014,** *7* (8), 2070-2080.

173. Downes, C. A.; Marinescu, S. C., *J. Am. Chem. Soc.* **2015,** *137* (43), 13740-13743.

174. Panda, C.; Debgupta, J.; Díaz Díaz, D.; Singh, K. K.; Sen Gupta, S.; Dhar, B. B., *J. Am. Chem. Soc.* **2014,** *136* (35), 12273-12282.

175. Das, D.; Pattanayak, S.; Singh, K. K.; Garai, B.; Sen Gupta, S., *Chem. Commun.* **2016,** *52* (79), 11787-11790.

176. Wang, C.-C.; Chang, H.-C.; Lai, Y.-C.; Fang, H.; Li, C.-C.; Hsu, H.-K.; Li, Z.-Y.; Lin, T.-S.; Kuo, T.-S.; Neese, F.; Ye, S.; Chiang, Y.-W.; Tsai, M.-L.; Liaw, W.-F.; Lee, W.-Z., *J. Am. Chem. Soc.* **2016,** *138* (43), 14186-14189.

177. Wang, B.; Lee, Y.-M.; Tcho, W.-Y.; Tussupbayev, S.; Kim, S.-T.; Kim, Y.; Seo, M. S.; Cho, K.-B.; Dede, Y.; Keegan, B. C.; Ogura, T.; Kim, S. H.; Ohta, T.; Baik, M.-H.; Ray, K.; Shearer, J.; Nam, W., **2017,** *8*, 14839.

178. Pfaff, F. F.; Kundu, S.; Risch, M.; Pandian, S.; Heims, F.; Pryjomska-Ray, I.; Haack, P.; Metzinger, R.; Bill, E.; Dau, H.; Comba, P.; Ray, K., *Angew. Chem., Int. Ed.* **2011,** *50* (7), 1711-1715.

179. Liao, R.-Z.; Li, X.-C.; Siegbahn, P. E. M., *Eur. J. Inorg. Chem.* **2014,** *2014* (4), 728-741.

ABSTRACT

WATER SPLITTING USING COBALT-BASED AMIDOPYRIDINE COMPLEXES

by

HABIB BAYDOUN

December 2017

Advisor: Dr. Claudio N. Verani

Major: Chemistry (Inorganic)

Degree: Doctor of Philosophy

As part of the ongoing search for clean energy sources, splitting water into oxygen and hydrogen has emerged as a promising source of alternative energy. We are interested in developing electrocatalysts capable of performing water reduction and water oxidation. In this dissertation, a variety of catalytic platforms based on an amidopyridine framework are studied. A novel monomeric cobalt complex in an amidopyridine ligand environment, ($[Co^{III}(L^1)(pyrr)_2]PF_6$), was investigated for electrocatalytic water reduction and found to have an onset overpotential of 0.54 V and an observed TOF of 23 min^{-1}. The catalytic decomposition pathway was explored with the aim of designing more stable catalysts.

Following the initial design, we prepared a modified catalyst in which the amidopyridine framework is extended over a phenylene tetraamine bridge to yield $[(Co^{III})_2L^2(pyrr)_4](PF_6)_2$. The bimetallic cobalt complex showed significant improvement in catalytic activity: onset overpotential decreased to 0.45 V and the TOF was found to be 60 min^{-1} per cobalt center under identical catalytic conditions. To the best of our knowledge this is one of the first examples where a dimeric catalyst is more active than its monomeric counterpart. Moreover, we showed that the dimer operates using a voltage-dependent mechanism, in which side reactions associated with deactivation are avoided at low applied potentials.

Finally, we demonstrate that we can drive water oxidation by modification of conductive carbon black-based supports with the hydrophobic octadecyloxy substituted catalyst in an N2N2' environment, $[Co^{III}(L^{OC18H37})(pyrr)_2]ClO_4$. The prepared assemblies can catalyze water oxidation at an onset overpotential of 0.32 V, and reach a current density of 10 mA/cm^2 at an overpotential of 0.37 V. The molecular nature of the catalyst was ascertained using XPS analysis. A DFT-supported mechanism suggests the ligand is heavily involved in catalysis as an electron reservoir.

The work presented in this dissertation emphasizes the importance of taking into account ligand involvement while designing novel catalysts. In the case of water reduction, we showed that ligand involvement had deleterious effects on catalysis, however for water oxidation we showed that ligand involvement can lower the activation barrier needed for catalysis. Future work will focus on using these lessons to design more active catalysts.

AUTOBIOGRAPHICAL STATEMENT

Habib Baydoun

EDUCATION

2012–2017 Wayne State University, Detroit, MI **Ph.D., Chemistry**
2008–2011 American university of Beirut **B.S., Chemistry**

HONORS AND AWARDS

- Recipient of the Mary G. Wood Endowed Scholarship for **2017-2018**
- Recipient of the Summer Dissertation Fellowship; Spring/Summer **2017**
- Second place poster winner at the Graduate and Postdoc Research Symposium in the Graduate Student category, *Wayne State University, Detroit, MI;* ***2016***
- Recipient of the Thomas C. Rumble Graduate fellowship; academic year **2015/2016**
- Honorable mention, National Science Foundation Graduate Research Fellowship Program; ***2014***

PUBLICATIONS

1. Liyanage, D. R.; Li, D.; Cheek, Q.; **Baydoun, H.;** Brock, S.; Synthesis and Oxygen Evolution Reaction (OER) Catalytic Performance of $Ni_{2-x}Ru_xP$ Nanocrystals: Enhancing Activity by Dilution of the Noble Metal. *J. Mater. Chem. A* ***2017***, *5*, 17609.
2. **Baydoun, H.**; Mazumder, S.; Schlegel, H. B.; Verani, C.; Deactivation of a cobalt catalyst for water reduction *via* valence tautomerism, *Chem. Eur. J.* **2017,** *23*, 9266.
3. Li, D.; **Baydoun, H.;** Kulikowski, B.; Brock, S.; Boosting the Catalytic Performance of Iron Phosphide Nanorods for the Oxygen Evolution Reaction by Incorporation of Manganese, *Chem. Mater.* **2017**, *29*, 3048. *(One of the most read papers for April 2017)*
4. Gonawala, S.; **Baydoun, H.**; Wickramasinghe, L.; Verani, C.; Efficient water oxidation with Langmuir-Blodgett films of procatalytic $[Co^{III}(N_2O_3)]$ surfactants on electrodes, *Chem. Commun.* **2016**, *52*, 8440.
5. Li, D.; **Baydoun, H.;** Verani, C.; Brock, S.; Efficient water oxidation using CoMnP nanoparticles, *J. Am. Chem. Soc.* **2016**, *138*, 4006.
6. Basu, D.; Mazumder, S.; Niklas, J.; **Baydoun, H.;** Wanniarachchi, D.; Shi, X.; Staples, R.; Poluektov, O.; Schlegel, H. B.; Verani, C.; Evaluation of the coordination preferences and catalytic pathways of heteroaxial cobalt oximes towards hydrogen generation, *Chem. Sci.* **2016,** *7*, 3264.
7. Basu, D.; Mazumder, S.; Shi, X.; **Baydoun, H.;** Niklas, J.; Poluektov, O.; Schlegel, H. B.; Verani, C.*; Ligand transformations and efficient proton/water reduction with cobalt catalysts based on pentadentate pyridine-rich environments, *Angew. Chem. Int. Ed.* **2015,** *54*, 2105.
8. Wickramasinghe, L.; Mazumder, S.; Gonowala, S.; Perera, M. M.; **Baydoun, H.;** Thapa, B.; Li, L.; Xie, L.; Mao, G.; Zhou, Z.; Schlegel, H. B.; Verani, C.; Mechanisms of rectification in Au │molecule │Au devices based on Langmuir-Blodgett films of iron(III) and copper(II) surfactants, *Angew. Chem. Int. Ed.* **2014,** *53*, 14462.
9. Ghauch, A.; Abou Assi, H.; **Baydoun, H.;** Tuqan, A.; Bejjani, A; Fe^0-based trimetallic systems for the removal of aqueous diclofenac: mechanism and kinetics, *Chem. Eng. J.* **2011,** *172*, 1033.
10. Ghauch, A.; **Baydoun, H.;** Dermesropian, P.; Degradation of aqueous carbamazepine in ultrasonic/Fe^0/H_2O_2 systems, *Chem. Eng. J.* **2011,** *172*, 18.
11. Ghauch, A.; **Baydoun, H.;** Tuquan, A.; Ayoub, G.; Naim, S.; Submicrometric iron particles for the removal of pharmaceuticals in water: Application to β-lactam antibiotics, *Advanced Materials Research*, **2011,** *324*, 485.